Title
In-situ microscopy of the first-order magnetic phase transition in FeRh thin films

Author
Baldasseroni, Chloe

Publication Date
2013

Peer reviewed|Thesis/dissertation

In-situ microscopy of the first-order magnetic phase transition in FeRh thin films

by

Chloe Baldasseroni

A dissertation submitted in partial satisfaction of the
requirements for the degree of
Doctor of Philosophy

in

Engineering - Materials Science and Engineering

in the

Graduate Division

of the

University of California, Berkeley

Committee in charge:

Professor Frances Hellman, Chair
Professor Ronald Gronsky
Professor David Attwood

Fall 2013

In-situ microscopy of the first-order magnetic phase transition in FeRh thin films

Abstract

In-situ microscopy of the first-order magnetic phase transition
in FeRh thin films

by

Chloe Baldasseroni

Doctor of Philosophy in Engineering - Materials Science and Engineering

University of California, Berkeley

Professor Frances Hellman, Chair

Simple ferromagnetic (FM) and antiferromagnetic (AF) materials such as Fe and Cr become paramagnetic when heated above some critical temperature, in what is known as a second-order phase transition. Less usual magnetic transitions are found in the magnetic world, for example a first-order magnetic phase transition from AF to FM with increasing temperature. Equiatomic FeRh has been known to exhibit such a transition for over 50 years, with a transition temperature slightly above room temperature. Interest in this material has been renewed in the recent years due to its potential application for heat-assisted magnetic recording, as well as a test system for fundamental studies of the physics of magnetic phase transitions. Similarly to crystallization, this AF-FM transition is expected to proceed by nucleation of magnetic domains but the features of the first-order hysteretic transition have been difficult to study with macroscopic measurements and very few microscopic studies have been performed.

In this work, FeRh thin films were synthesized by magnetron sputtering and structurally and magnetically characterized. A membrane-based heating device was designed to enable temperature-dependent microscopy measurements, providing a thermally uniform and well-controlled sample area. Synchrotron x-ray magnetic microscopy was used to study the temperature-driven AF-FM phase transition in epitaxial FeRh thin films in zero field. Using magnetic microscopy with x-ray magnetic circular dichroism, the different stages of nucleation, growth and coalescence of FM domains were observed across the transition and details of the nucleation were identified. The FM phase nucleates into single domain islands and the width of the transition of the individual nuclei upon heating is sharper than that of the macroscopic transition. Using magnetic microscopy with x-ray magnetic linear dichroism, the evolution of the AF phase was studied. Differences in the morphology of AF and FM phases were found, with the AF phase having a smaller feature size limited

by defects. Finally, interfacial FM at the interface with capping layers is due to an alloying effect with a third metallic element that stabilizes the FM phase at room temperature by lowering the transition temperature.

Contents

List of Figures

List of Tables

Acknowledgments

I want to thank my advisor Frances Hellman for giving me the opportunity of this memorable experience at Berkeley and for teaching me thoroughness and integrity in science. I thank the members of my committee David Attwood and Ronald Gronsky for taking the time to read this work and for their encouragements back when I was taking my qualifying examination. I have had the chance to share a lab and an office with many members of the Hellman group over these 5 years, many who helped contribute to this work. The "old timer physicists" Daniel Queen, Dave Cooke and Zoe Boekelheide gave me memorable summers in the Microlab. Hyeon-Jun Lee had a lot of lab wisdom to offer. Cathy Bordel provided priceless resources, energy, and enthusiasm and was an awesome colleague and friend. It was wonderful to develop a material sciency friendship with Julie Karel as she helped me navigate the MSE program at the beginning and it was a pleasure to get to work with her at the end. Undergraduate students Neal Reynolds, Neil Anderson and Hye Jin Lee gave me the opportunity to mentor them. I also thank all the more recent members of the Hellman lab: Cory Antonakos, Laura Sposato, Hilary Jacks and Alex Ceballos for making me not want to leave such a fun lab (informal lab outings!) with special extra thanks to Cory for her patience in receiving my Nanolab training.

Synchrotron measurements are time intensive and quite daunting if not done with a large team of people. In addition to Cathy, Cory and Alex from my lab and Mi-Young Im and Peter Fisher at the ALS, I am also indebted to many people for providing manpower, knowledge and expertise to the PEEM microscopy measurements (and their analysis!) presented in this work. Julia Herrero-Albillos, Alexander Kaiser, Claus Schneider, Sergio Valencia, Ahmet Unal and Florian Kronast made the measurements at BESSY possible. Special thanks to Chuck Fadley and the helpful members of his group that I was lucky to collaborate with, at LBNL and at BESSY: Alex Gray, Gunnar Palsson and Slavo Nemsak. Jeffrey Kortright and Kevin Stone helped make the XMLD study of FeRh possible. Finally, Andreas Scholl provided tireless and patient support and expertise in attempting an almost impossible measurement at his beamline at the ALS.

I thank Julie Borchers and Brian Maranville of NIST for their neutron expertise and friendly collaboration. Kin Man Yu at LBNL was much help with the RBS characterization. Kerry Maize and Ali Shakouri allowed beautiful thermoreflectance measurements of my devices at UCSC. I also thank the students and staff at the NanoLab for their assistance with microfabrication, and Sufal Swaraj and David Kilcoyne for giving me the opportunity to test heater stages at beamlines at the ALS. Eric Harley and Emmanuelle Sarrouy provided much needed MATLAB simulation tips when I was stuck.

This work was also made possible by many non-scientific contributions from my family and friends. My family provided loving support over the years, sometimes in the form of cross-Atlantic shipments of French delicacy. I thank Blythe for her

dedicated emotional support. This work would have not been possible without her. Finally, my best friend Aurelie K was always there to listen and share about the sometimes inevitable despair of graduate studies.

This work was supported by the Director, Office of Science, Office of Basic Energy Sciences, Materials Sciences and Engineering Division, of the U.S. Department of Energy (DOE) under Contract No. DE-AC02-05CH11231.

Chapter 1

Introduction

Equiatomic FeRh was discovered in 1939 by Fallot *et al.* to undergo an unusual temperature-driven magnetic phase transition [1]. The two different magnetic phases were later identified as antiferromagnetic (AF) and ferromagnetic (FM) with the AF phase transitioning into FM with increasing temperature [2, 3]. This phase transition can also be driven by magnetic field, defining it as a metamagnetic transition, and is coupled to a lattice expansion. The first-order character of this phase transition was established by the abrupt and hysteretic change with temperature of different properties such as magnetization, resistivity, and lattice parameter, and the presence of latent heat at the transition.

Other magnetic alloys such as Ru doped $CeFe_2$ and Gd_4Ge_5 or Si doped RGe_5 with R heavy rare earth element (Gd or higher Z) exhibit a similar first-order AF-FM magnetic phase transition with increasing temperature [4, 5]. FeRh is a unique system compared to the rare earth alloys which have a cryogenic temperature transition: the transition is situated just above room temperature (near 350 K). Therefore it has been and is still of significant interest in the physics and materials science community, as well as for technological applications. FeRh has been studied in the bulk for over 50 years [6] and more recently in thin film form [7, 8, 9]. Current investigations of this unique transition range from the fundamental understanding of the origin and nature of the transition [10] to applications associated with the transition such as a giant magnetocaloric effect and a giant volume magnetostriction [11, 12]. A large reason for the interest in FeRh in thin film form is that thin films have been proposed as a candidate material for heat-assisted magnetic recording (HAMR) in an exchange-spring system coupled to a hard magnetic layer (for example FePt or CoPt) [13, 14, 15]. In those thin films, the transition temperature has been shown to be sensitive to changes in composition and substrate-induced strain as well as structural and chemical order and these effects remain to be fully understood. The thin film form is ideal in providing easy control of film composition and stress to allow the study of these factors on the phase transition mechanism.

At compositions below 10 at.% Rh, FeRh alloys have a bcc structure α at room

temperature which is FM. In the 10 to 45 at.% Rh composition range, the FeRh system orders chemically into a CsCl crystal structure α', still FM. Near equiatomic composition CsCl-ordered FeRh exhibits unusual magnetic properties with temperature [6]. This structure has AF order at low temperature in a type G structure with Fe moments aligned parallel along (111) planes and no moment on the Rh atom. When increasing the temperature above a transition temperature T_0 (between room temperature up to above $100°C$ depending on sample form and processing) the structure becomes FM with Fe moment of $3.2\mu_B$ and a small Rh induced moment of $1\mu_B$ [16]. The crystal structure is conserved but a lattice expansion of up to 1% is observed upon transition. The equivalence between temperature and magnetic field in driving the transition has been shown in both bulk samples and thin film samples, with the magnetic field effectively lowering T_0.

Similarly to a classic first-order phase transition such as crystallization which proceeds by nucleation, metasbility between the two magnetic phases is believed to lead to a phase coexistence of the AF and FM phases across the transition and this transition is expected to proceed by nucleation and growth of a new distinct phase out of the original phase. Instead of nucleating crystals, magnetic domains are nucleated. Several recent studies have aimed at characterizing the nucleation and growth process by magnetization measurements [7, 17]. By measuring the magnetization as a function of temperature, under constant magnetic field, one can observe the hysteretic character of the transition which requires overheating to nucleate the FM phase and undercooling to nucleate the AF phase. The characteristics of the M-T transition such as the width of the hysteresis and the broadening as well as the temperature T_0 itself are influenced by different parameters such as substrate (through its effect on thin-film stress), composition and doping by different elements (Ir, Pt increase T_0 while Co, Ni, Pd decrease T_0 for example).

How the changes in M-T characteristics translate into changes in the nucleation regime is not well understood yet. In fact the bulk magnetization measurements have two limitations: they require to measure the effect of temperature under a constant external magnetic field, therefore do not allow to study the transition driven by temperature only, and they rely on measuring a macroscopic parameter to characterize a mechanism that proceeds at a microscopic level. Limited microscopy measurements of FM domains in FeRh have been performed, none of them being able to study the temperature driven or field driven transition, in-situ [18, 19]. They nevertheless showed a lenghtscale of FM domains on the order of 100 nm.

This work presents the study of the in-situ nucleation of magnetic domains in FeRh thin films by microscopy to gain understanding of the unusual magnetic phase transition in FeRh. A clear understanding of the nucleation and growth of magnetic domains in both phases opens the possibility of determining how the transition can be tuned. Synchrotron radiation offers the tunability and the brightness that enables magnetic microscopy with elemental sensitivity and sub-100 nm spatial resolution, needed for our system. In particular, photoemission electron microscopy (PEEM)

will be used, combined with polarized x-rays. Using an x-ray incident microcopy technique allows to take advantage of polarized x-rays. Indeed, circular polarization provides sensitivity to FM and linear polarization to AF.

It is common to cap thin films susceptible to oxidation with a protective thin film layer. Typical materials used for capping are noble metals such as Au and Pt, light self-passivating metals such as Al, or oxides such as MgO or Al_2O_3. A series of recent studies have showed that substrate and capping materials can induce interfacial effects where the magnetic properties of the FeRh film are substantially modified near the interface with the capping layer as well as the substrate [20, 21, 22]. These interfacial effects are directly relevant to the successful integration of FeRh in HAMR technology and their study will be part of the work reported here, by relating them to the sensitivity of the transition temperature T_0 to strain, composition and doping by other elements.

Chapter 2 presents the FeRh growth thin film method and the different experimental characterization techniques used. Epitaxial films were grown by magnetron sputtering and their structural, chemical and magnetic properties were characterized. In particular the effect of the different parameters on the transition temperature and characteristics were studied and a corrected phase diagram is proposed.

Chapter 3 details the development of a membrane-based device with the goal to enable temperature-dependent synchrotron microscopy studies: a microfabricated amorphous silicon nitride membrane-based nanocalorimeter is proposed to be suitable for an x-ray transparent sample platform with low power heating and built-in temperature sensing. Thermal characterization in both air and vacuum are analyzed experimentally, including thermal imaging, and via simulation. A simulation model that includes conduction, as well as radiation and convection heat loss, is presented. A new simple design that has improved temperature homogeneity and a large isothermal area while maintaining a thin thermal conduction layer is proposed and fabricated. This new design enables applications in transmission X-ray microscopes and spectroscopy set-ups at atmospheric pressure and is tested on a magnetic thin film.

Results from the microscopic study of the nucleation of the FM phase are presented and discussed in Chapter 4. The evolution of FM domains across the temperature-driven AF to FM phase transition in uncapped and capped epitaxial FeRh thin films is studied by x-ray magnetic circular dichroism (XMCD) and photoemission electron microscopy. The coexistence of the AF and FM phases is evidenced across the broad transition and the different stages of nucleation, growth and coalescence are directly imaged. Details of the nucleation of single domains are discussed.

Chapter 5 summarizes the attempt at the reciprocal study of the AF phase. The evolution of the AF phase across the temperature-driven FM to AF transition upon cooling in uncapped epitaxial FeRh thin films is studied by x-ray magnetic linear dichroism (XMLD) and photoemission electron microscopy. By comparing XMLD and XMCD images recorded at the same temperature, the AF phase is identified,

its structure is directly imaged, and its evolution is studied across the transition. A quantitative analysis of the correlation length of the images shows differences between the characteristic lengthscale of the two phases with the AF phase having a finer feature size. The asymmetry of the transition between the evolution of the AF upon cooling and the FM phase upon heating is studied at the microscopic level.

Chapter 6 focuses on an important issue related to the technological application of FeRh. FeRh is a system that has been shown to be extremely sensitive to external factors such as strain and composition or dopant. The role of capping material in stabilizing a thin FM layer at the interface between a FeRh film and cap in the nominally AF phase at room temperature is studied by XMCD in photoemission electron microscopy and polarized neutron reflectivity. These techniques are used to determine the presence or absence of interfacial ferromagnetism (FM) in films capped with oxides and metals. Chemically stable oxide caps are shown to not generate any interfacial FM while the effect of metallic caps depends on the element, showing that interfacial FM is due to metallic interdiffusion and the formation of a ternary alloy with modified AF to FM transition temperature.

Chapter 3 is largely a reprint of "Heat transfer simulation and thermal measurements of microfabricated X-ray transparent heater stages" published in the Review of Scientific Instruments, reprinted with permission from [23], Copyright 2011, AIP Publishing LLC. Chapter 4 is largely a reprint of "Temperature-driven nucleation of ferromagnetic domains in FeRh thin films" published in Applied Physics Letters, reprinted with permission from [24], Copyright 2012, AIP Publishing LLC.

Chapter 2

FeRh thin films growth and characterization

2.1 Introduction

FeRh has seen a renewed interest in recent years due to its potential use in magnetic recording technology. In this technology, magnetic layers used in hard disk drives are in thin-film form, therefore a thin-film processing technique is required. The two families of techniques are physical vapor deposition (PVD) and chemical vapor deposition (CVD). Metal thin-films are typically synthesized by PVD. In particular one technique that is common both in academia and industry is sputter deposition. In this work, we focus on the study of FeRh in thin-film form. First, this has the advantage of giving easy control of the film composition. Second, since the film is deposited on a substrate, the relationship between the film and the substrate potentially gives control of the stress of the film, in particular by distortion of the crystal structure. Finally, for microscopy studies, flat and thin samples are desired, and both of these characteristics are intrinsic to thin-film processing, compared to bulk processing. In this chapter, the growth technique of sputter deposition is presented, followed then by the different characterization techniques used to determine the structural, magnetic and chemical properties of the thin films. While the x-ray diffraction method used in the structural characterization is specific to thin-films, the magnetic measurement technique and the composition analysis techniques used are not. Finally an experimental phase diagram of the magnetic phase transition region is proposed.

2.2 Growth technique

FeRh thin films are prepared by magnetron sputtering (Hellman Lab) from an FeRh alloy target. In magnetron sputtering, Ar ions impinge on a material target to sputter atoms. Those energetic atoms are then deposited onto a substrate. The

Parameter	Range of values
Ar sputter pressure	1 to 4 mTorr
DC power	25 to 50 W
Growth temperature	150 to 600°C

Table 2.1: Range of sputter deposition parameters used.

films are prepared in a high vacuum sputtering chamber with a typical base pressure of 8×10^{-8} Torr. The temperature of the substrate is controlled by a halogen heating lamp situated right behind the sample holder. The maximum temperature set-point that our AJA sputter deposition system enables is 650°C. At this heating lamp set-point value, the actual temperature of a sample mounted on the sample holder was experimentally determined with a thermocouple mounted between the sample and the sample holder and found to be 600°C. We therefore estimate an offset of 50°C for all deposition temperatures and report the estimated temperatures throughout the rest of this document. The deposition rate is controlled by the DC power applied to the material target and is calibrated by a quartz crystal microbalance. Finally, another growth parameter that can be controlled is the Ar sputtering pressure. The pressure affects the relative sputtering yield of the different species in the FeRh alloy target by controlling their kinetic energy, thereby giving control of the composition of the film.

Therefore three independent growth parameters were varied so as to establish a systematic growth pattern and optimize the films quality: deposition temperature, sputtering pressure and growth rate (controlled by the DC power). In the next sections we present the effect of the three growth parameters on the structural, chemical and magnetic properties of FeRh thin films. These three parameters were varied over the range summarized in Table 2.1. The effect of post-deposition anneal was also studied and will be briefly discussed. An alternative growth technique reported in the literature is electron beam evaporation from separate elemental sources [17, 20, 21] or sputtering from two separate Fe and Rh targets [14, 22, 25, 26] but the majority of studies are on FeRh deposited by sputtering from an alloy target [7, 8, 9, 13, 27, 28, 29, 30].

All films are around 100 nm thick and deposited on MgO substrate unless specified otherwise. All films studied in this chapter were not capped, resulting in a native oxide of thickness 2 nm and likely composition Fe_2O_3, as determined by hard x-ray photoemission(see Section 6.3). The effect of capping layer will be studied in Chapter 6.

2.3 Structural characterization

The reported crystal stucture of the desired FeRh phase is CsCl (B2) with a lattice parameter of 0.299 nm in the bulk. θ-2θ geometry scans were performed in a powder diffractometer. They enable to determine the phase and check for texturing of the crystal structure with a preferential orientation. ϕ scans were performed in a triple axis diffractometer. They allow us to check for the single crystalline quality of the films and their epitaxial relationship to the substrate. In addition, in the case of epitaxial films, the lattice parameters can be determined using the triple axis diffractometer.

Phase and texture determination

An FeRh thin film was deposited simultaneously on MgO (001) and amorphous Si-N (a-Si-N) on Si with an Ar pressure of 2 mTorr, a DC power of 40 W and deposition temperature of 600°C. θ-2θ scans are shown in Figure 2.1. Except for the higher intensity peaks identified as respective substrate peaks and labeled with star symbols on the plot, all other peaks are identified as FeRh CsCl phase. While the film on a-Si-N exhibits 110, 111 and 211 peaks, indicating a polycrystalline structure, for the film grown on MgO only Bragg reflections of (001), (002) and (003) planes are seen in the range of 2θ measured, suggesting epitaxy, which will be confirmed with triple axis diffractometry.

We find that for a deposition temperature of 600°C, epitaxy with (001) out-of-plane orientation is obtained over the entire range of Ar pressure and DC power studied. The average CsCl structural coherence length t in the thin film can be calculated from the width of the 001 peak using Scherrer's formula

$$t = \frac{0.9\lambda}{Bcos\theta} \tag{2.1}$$

with $\lambda = 0.154178$ nm (CuK_α) and B = FWHM of 2θ peak (in radians) [31]. In a polycrystalline film, this would correspond to the average grain size. In our epitaxial films, this coherence length is likely limited by low angle grain boundaries or antiphase boundaries. The average coherence length in the {001} planes for the entire range of deposition parameters is 33 nm. Note that since 001 is a superlattice peak due to the CsCl structure, the coherence length is related to the chemical order. No clear correlation is seen between t and the Ar sputter pressure or the growth rate while the temperature is seen to increase the coherence length by a few nm.

Epitaxy

Having found that under the right conditions our films show (001) out-of-plane orientation, we then used a thin-film triple axis diffractometer to confirm the epitaxy. The cubic structure and lattice parameter of FeRh make it a particularly good

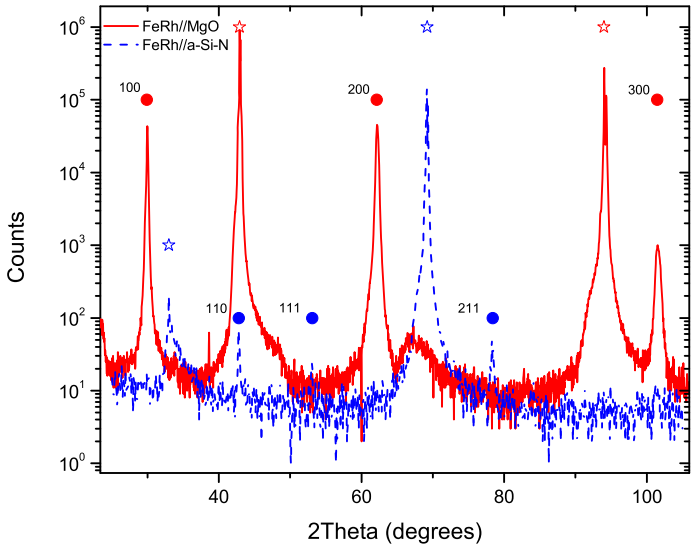

Figure 2.1: Comparison of the x-ray diffraction spectra for a polycrystalline FeRh film deposited on a-Si-N on Si substrate (blue dashed line) and an epitaxial FeRh film deposited on (001) MgO substrate (red solid line). The lines are the diffracted intensities from the FeRh films. The star symbols indicate the 2θ position of the Si and MgO substrate peaks. The circle symbols indicate the FeRh film peaks with the corresponding hkl labels.

candidate for epitaxy on single crystalline (001) MgO substrates by a 45° rotation to the 0.4212 nm lattice parameter (Fig. 2.2). We already established that there is a parallelism between the (001) planes of FeRh and MgO. To qualify for epitaxy a parallelism between specific crystallographic directions within those planes must also exist [32]. By looking at an off-axis peak such as 101 and recording the intensity of this peak during a full in-plane rotation of the film, known as a 360° ϕ scan, one can determine the in-plane symmetry of the crystal structure. A film with a cubic single-crystal orientation in the plane shows 4 Bragg peaks in the ϕ scan, consistent with the 4-fold symmetry of the cubic crystal. Then, a 360° ϕ scan of the 202 MgO substrate peak shows the expected 45° rotation to the film (Fig. 2.2) and we therefore confirm the following epitaxy relationships:

FeRh (001)//MgO (001)

FeRh [100]//MgO [220]

We then turn to the effect of the deposition temperature. 101 ϕ scans recorded for films grown at different deposition temperatures of 600°C, 350°C and 150°C are shown in Figure 2.3. All films deposited at a temperature of 150°C or higher show four-

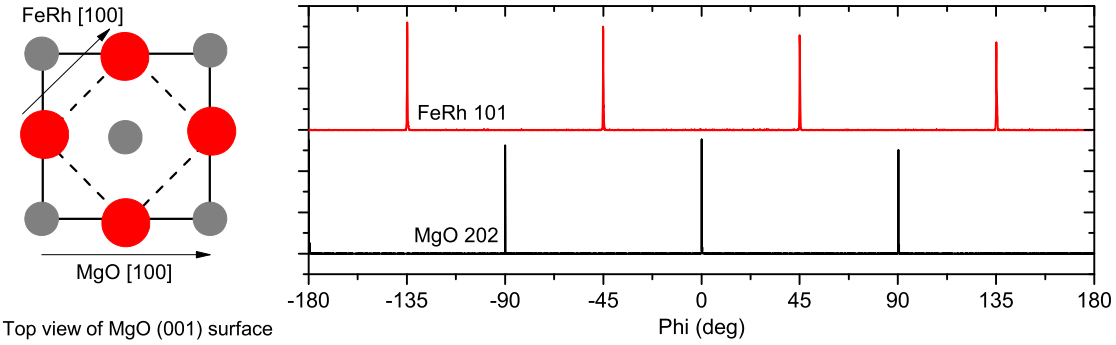

Figure 2.2: Diagram of the (001) surface of the MgO substrate showing the in-plane epitaxial relation with FeRh as displayed in the 360 degrees ϕ scans of FeRh 101 and MgO 202.

fold symmetry, indicating their single-crystalline character with the same epitaxial relationship to the MgO substrate. The FWHM of the ϕ peaks is related to the mosaicity of the crystal. The right panel in Figure 2.3 shows one representative peak for each growth temperature. The small difference in ϕ position comes from sample alignment offsets in the instrument and is not physically significant. The FWHM is calculated for each film with a Gaussian fit. We find that the FWHM decreases greatly from 1.69° at 150°C to 0.47° at 350°C, and decreases further to 0.28° at 600°C, indicating an improvement in the mosaicity of the film with increasing growth temperature.

Analysis of the ratio of 001 to 002 Bragg peaks integrated intensity in θ-2θ scans, related to the chemical order parameter, also indicates that the chemical ordering improves with increasing growth temperature. Note that the values commonly reported in the literature are $\sqrt{I_{001}/I_{002}}$ instead of the actual chemical order parameter S which is corrected for the geometry of the x-ray diffractometer and the film, and the structure factors of Fe and Rh. Reported values of $\sqrt{I_{001}/I_{002}}$ range from 0.8 to 1.18 [25, 26, 30] (since this is not corrected for the theoretical intensities, values above 1 are possible). De Vries *et al.* recently reported a chemical order parameter $S = \sqrt{I_{001}/I_{002}}_{exp}/\sqrt{I_{001}/I_{002}}_{calc}$ for sputtered and post-annealed FeRh thin films [33]. S increases with post-annealing temperature from 0.67 at 600°C to 0.89 at 800°C.

The chemical order parameters was calculated for three of our films, all grown under the same conditions of 2 mTorr Ar pressure, 40 W power and 600°C growth temperature, the highest growth temperature (no post-growth anneal). The three samples only differ in composition from 49 to 51.4 at.% Rh. The theoretical intensities

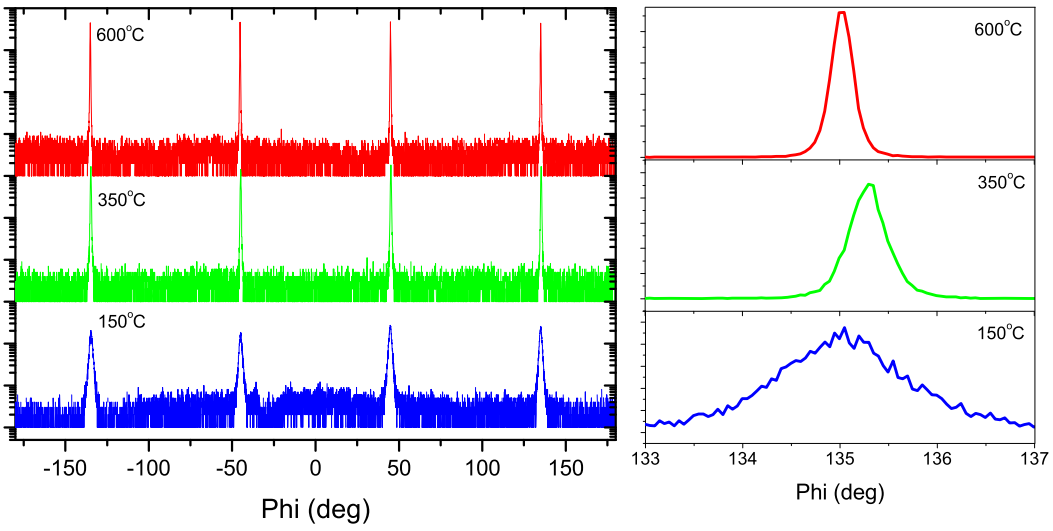

Figure 2.3: 360 degrees ϕ scans of FeRh thin films processed at different deposition temperature (left) and zoom-in on the 135 deg peak, showing the reduction in FWHM with increasing growth temperature (right). The 600°C and 350°C films were deposited with 1 mTorr Ar, and the 150°C film with 2 mTorr Ar.

were calculated in the following way:

$$I^{calc} \propto |(1-x)f_{Fe} + (x)f_{Rh}(-1)^{h+k+l}|^2 \times (1+\cos^2 2\theta) \times \frac{1}{\sin 2\theta} \times (1-\exp(-\frac{2ut}{\sin\theta})) \times \exp(-2B(\frac{\sin\theta}{\lambda})^2) \quad (2.2)$$

The different terms in this equation are the structure factor, the polarization factor, the Lorentz factor, the absorption factor and the temperature factor. The structure factor takes into account the composition of the film. Expressions for the polarization factor, the Lorentz factor for a single crystal and the temperature factor are taken from Ref. [31] with the B coefficient calculated from values tabulated therein. While the absorption factor is constant in the case of thick samples and can therefore be ignored, it is not the case for thin films. The expression for this factor is taken from Ref. [34] where the linear absorption coefficient u is the product of mass absorption coefficient $\mu_{FeRh} = 249.25$ cm^2/g and density $\rho_{FeRh} = 9.76$ g/cm^3 and t is the thickness, here 100 nm. For the three films investigated (S11-004, S11-166, S12-031) we find an average $S = 0.88\pm0.03$. This is comparable to the best S reported by de Vries *et al.*

Finally the effect of a post-growth anneal was investigated. We found that a film grown at 600°C shows no further improvement of its mosaicity and chemical ordering after a post-growth anneal of 8 hours at 600°C in vacuum. Therefore, for

optimal crystal quality of FeRh thin films, a deposition at 600°C is selected with no post-growth anneal.

Lattice parameters and strain

Epitaxial films can be further characterized to determine their in-plane and out-of-plane lattice parameters and therefore determine their strain state. First we turn to the 100 nm films grown on MgO substrate.

Using the reported FeRh bulk lattice parameter of a =0.299 nm and the spacing between {220} MgO planes of a' =0.2978 nm, a lattice misfit or mismatch $f = \frac{a-a'}{a}$ of 0.4 % is calculated. In the extreme case of commensurate epitaxy, the film is coherently strained meaning that the FeRh lattice would contract biaxially in-plane to match the susbstrate, with a compression factor equal to the mismatch, and would expand out-of-plane:

$$\epsilon_{x,y} = -f; \epsilon_z = \frac{-2\nu\epsilon_{x,y}}{1-\nu} \tag{2.3}$$

with ν Poisson's ratio (0.32 calculated for FeRh [35]) resulting in a tetragonal distortion. In reality, the strain depends on the thickness of the film. For a given mismatch, there is a critical thickness t_c above which the coherently strained state is not energetically favorable. Above this thickness, the internal energy of the film can be lowered by the creation of crystallographic defects, called misfit dislocations, resulting in discommensurate epitaxy.[32, 36] The total internal energy of a film of thickness t can be written as the sum of two components $U = U_\epsilon + U_d$ with U_ϵ the strain energy stored per unit area

$$U_\epsilon = (\frac{E}{1-\nu})\epsilon_x^2 t \tag{2.4}$$

with E Young's modulus of elasticity, and U_d the dislocation energy per unit area of array of dislocations

$$U_d = 2\rho_l \frac{G_s b^2}{4\pi(1-\nu)ln(\frac{4t}{b})} \tag{2.5}$$

with ρ_l the linear density of the array of dislocations, $G_s = \frac{E}{2(1-\nu)}$ the shear modulus of elasticity and b the dislocation Burgers vector. t_c is defined as the thickness which minimizes the energy at $\epsilon_{x,y} = -f$ or $\frac{dU}{d\epsilon_{x,y}}(\epsilon_{x,y} = -f) = 0$. For the smallest edge dislocation in (001) plane in FeRh (Burgers vector $b = a$, in-plane lattice constant) and a mismatch of 0.4 %, t_c = 12 nm. The strain is progressively decreased by increasing the thickness above 12 nm and its value can be estimated by evaluating the strain $\epsilon_{x,y}$ for which the internal energy is minimized. For example for a film of 170 nm, 90 % of the initial mismatch strain of 0.4 % has been relieved. For our films of 100 nm, this simple model estimates a residual strain of -0.06%, possibly inducing a small degree of tetragonal distortion in the lattice.

The average strain can be determined experimentally by measuring the out-of-plane and in-plane lattice parameters c and a and calculating the tetragonal distortion c/a. c is directly determined by the d_{001} spacing. To determine a, we measure an off-axis peak which is related to a and c according to the definition of the d-spacing $\frac{1}{d_{hkl}^2} = \frac{h^2+k^2}{a^2} + \frac{l^2}{c^2}$ with hkl the Miller indices. For the {202} planes $\frac{1}{d_{202}^2} = \frac{4}{a^2} + \frac{4}{c^2}$ which gives

$$a = \frac{c \times 2d_{202}}{\sqrt{c^2 - (2d_{202})^2}} \tag{2.6}$$

Figure 2.4 shows the tetragonal distortion for FeRh films grown at $600°C$ with varied Ar pressure and deposition rate. The 2θ values compiled to calculate the tetragonal distortion of these different films were measured with two instruments: a Siemens D5000 powder x-ray diffractometer (Stacy lab in UCB-Chemistry) and a Panalytical XPert MRD Pro 4-circle diffractometer (Ramesh lab in UCB-Materials Science and Engineering). The accuracy of both instruments was estimated by calculating the statistical error obtained on measuring MgO single crystalline 002 and 004 peaks compared to the expected theoretical values. The relative 2θ average error is similar for both instruments at $\frac{\Delta 2\theta}{2\theta} = 8.2 \times 10^{-4}$. This results in an uncertainty in the values of lattice parameters of ± 0.0003 nm for the out of plane lattice constant c and ± 0.0006 nm for the in-plane lattice constant a (larger due to cumulative error) which in turn result in an uncertainty in tetragonal distortion $\frac{c}{a} \times 100$ of $\pm 0.3\%$. This is much larger than the strain of -0.06% estimated earlier. All films with a tetragonal distortion between 99.7 and 100.3 % are considered strain free within our measurement error and this strain-free range is indicated by the gray shaded region in Figure 2.4. Characterization of different films grown under identical conditions give excellent reproducibility within the error range. Note that the model used assumes that the strain is uniform through the thickness of the film and our measurement averages the strain over the entire thickness of the film.

No strong effect of Ar pressure or growth rate has been found. 100 nm films deposited with a power ranging from 25 W to 40 W and Ar pressure ranging from 2 mTorr to 4 mTorr are practically strain free. Films deposited at 40 W with 2 mTorr Ar pressure have the lowest reported tetragonal distortion of 99.9 % with lattice parameters $a = 0.2989$ nm and $c = 0.2986$ nm.

In an effort to increase the tetragonal strain in FeRh thin films with the possibility of giving rise to perpendicular anisotropy [37], additional films have been fabricated on different substrates (leading to different mismatch) and with reduced thickness (close to the critical thickness so as to keep the strain as close as possible to its maximum coherent strain value) [38].

Table 2.2 shows the crystal substrates that were tested. All these different substrates resulted in good epitaxy of FeRh. MgO and $KTaO_3$ substrates were found to induce large strain by reducing the thickness of the film to 5 nm, giving tetrag-

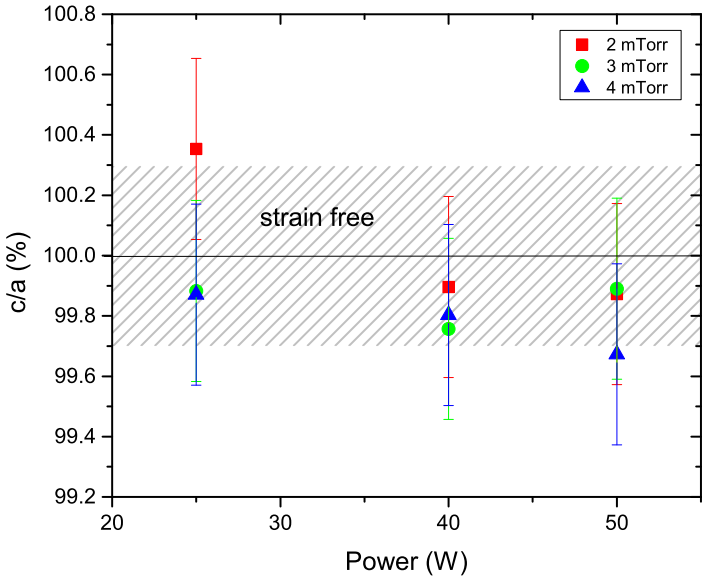

Figure 2.4: Tetragonal distortion c/a (times 100) in % as a function of FeRh target DC power (related to deposition rate) for different values Ar sputter pressure. The strain free region taking into account the measurement uncertainty is indicated with the shaded region.

onal distortions of 101.5 % and 102.1 % respectively. We notice that an increased distortion of only 0.76 % is gained by increasing the lattice mismatch by a factor of more than 10 (also note that this is within the range of our measurement error). One possible explanation is that while increasing the mismatch directly increases the coherent strain, it also decreases the critical thickness, making the relaxation of strain by defects more energetically favorable. Indeed the calculation of the critical thickness using Equations 2.4 and 2.5 shows that no minimum thickness can satisfy the minimum energy condition, indicating that misfit dislocations cannot be avoided. Because of this trade-off in energy, substrates with higher mismatch did not achieve the desired effect.

A brief review of cubic substrates that are commercially available indicates that there is a "gap" of lattice parameter available between MgO and $KTaO_3$. Based on the energy form of Equations 2.4 and 2.5 it is estimated that an FeRh film of thickness 4 nm deposited on a substrate with a mismatch $f = 0.02$ would experience a strain of 1 %. Therefore, substrates with a lattice parameter of 0.41 nm are sought. An

Substrate	Lattice parameter (nm)	Mismatch to FeRh	Critical thickness (nm)
MgO	0.4212	0.004	12
$KTaO_3$	0.3989	0.057	0
$SrTiO_3$	0.3905	0.081	0

Table 2.2: Summary of different substrates used with lattice parameter, mismatch and expected critical thickness. $h_c = 0$ indicates that the critical thickness minimum energy condition cannot be satisified.

alternative is to create such a substrate using epitaxy and strain. Epitaxial growth of strained MgO on $SrTiO_3$ has been reported to achieve an in-plane lattice constant of 0.414 to 0.418 nm [39, 40]. 10 nm of MgO was deposited by RF sputter from an MgO compound target onto $SrTiO_3$ at a temperature of 400°C. The out-of-plane lattice constant of a 20 nm FeRh thin film deposited on such a substrate is $c = 0.2978$ nm, within error bars of the relaxed lattice parameter, indicating that the film is mostly relaxed. Films thinner than 20 nm on this MgO/$SrTiO_3$ should be investigated in the future.

In summary, FeRh thin films grown by magnetron sputtering were synthesized with varying deposition parameters. The deposition rate has no significant effect on the crystalline properties measured. In contrast, the growth temperature has a strong effect. Increasing the growth temperature increases the coherence length and decreases the angle of mosaicity by increasing diffusion which favors larger grains with lower angle grain boundaries. Increased diffusion also favors the formation of the thermodynamically stable CsCl ordered phase, resulting in higher chemical order. 100 nm films on MgO are strain-free but tetragonal strain can be achieved in thinner films on other substrates.

2.4 Composition analysis

Rutherford backscattering spectrometry (RBS) was used for film composition analysis since it is one of the most quantitative elemental analysis technique [41]. The sample is exposed to a beam of high energy α particles (He^{++}) and the backscattered particles are detected as a function of energy. The kinetic energy of the backscattered particles is affected by interaction with the atoms constituting the sample in two ways: the mass of the collided atom (billiard-ball model of collision), with the heavier nuclei resulting in higher scattered He^{++} energy and the depth of the atom in the film (additional energy loss due to the stopping power of the electrons in the film). Therefore broadened backscattered peaks are detected for the different elements present in the film, resulting in a plateau-like profile. Elements with similar masses might result in overlap of the peaks. This is not an issue with Fe ($Z = 26$) and Rh ($Z = 45$) which have enough difference in atomic masses Z. The high energy onset

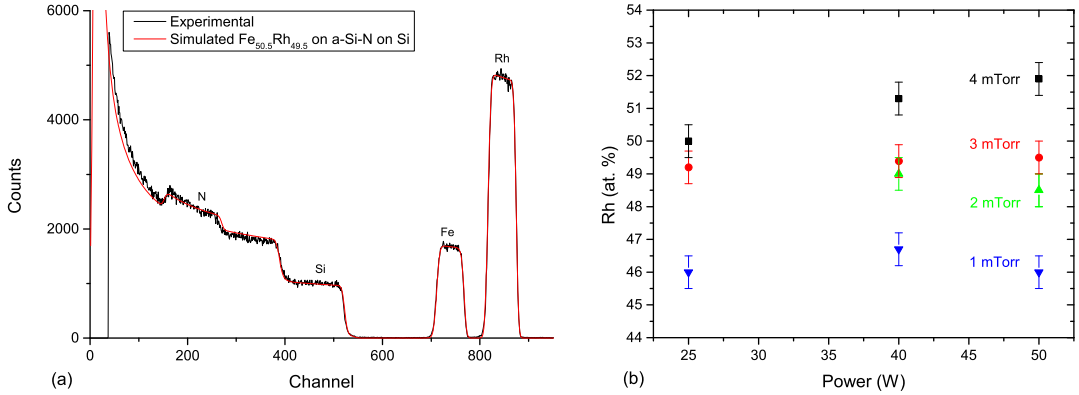

Figure 2.5: (a) Experimental RBS spectrum of 100 nm FeRh thin film with simulation performed with SIMNRA software. (b) Effect of Ar pressure and deposition rate on FeRh thin film composition as determined by experimental RBS measurement and simulated spectra analysis.

of the peak indicates the element present in the film and the breadth an estimate of the thickness of the film. The intensity of the backscattered peaks is proportional to Z^2. This means that for a 1 to 1 ratio of Fe and Rh, a ratio of intensities around 3 is expected. The data is fit using a software (SIMNRA) for precise composition determination. RBS was performed at Lawrence Berkeley National Lab, Materials Science Division.

A typical spectrum for FeRh thin film deposited on *a*-Si-N on Si is shown in Fig. 2.5 (a). A model is fit to the spectrum, varying the composition and thickness of the different layers constituting the sample. Figure 2.5 (b) shows the composition of FeRh films as a function of target power and Ar pressure. For a given pressure, small non-monotonic variations of composition are seen, within the measurement accuracy of ± 0.5 %. A strong effect of pressure is evidenced, which as mentioned earlier, is attributed to the control of relative sputtering yield of Fe and Rh by the pressure. Rh at.% increases with Ar pressure from 46 at.% at 1 mTorr to $\sim$51 at.% at 4 mTorr. In sputtering, thermalization of sputtered atoms occur when the atoms undergo enough scattering to have their kinetic energy reduced to the same level as the sputtering gas and results in a reduced deposition rate of the sputtered atoms [36]. The pressure at which thermalization occurs depends on the mass ratio of gas atom to the energetic particle. Rh (mass 102.9) is more different to Ar (39.95) than Fe (55.85), therefore for any given pressure, Fe atoms are closer to thermalization than Rh atoms and the change in gas scattering with gas pressure is more for Fe atoms than for Rh atoms. As a result, the reduction in deposition rate due to thermalization varies differently for Fe and Rh atoms with pressure. Both Fe and Rh sputter yields decrease with increasing

pressure, but the Fe sputter yield decreases at a faster rate, leading to lower Fe (higher Rh) concentration films at higher sputtering pressure. As will further be discussed in Sections 2.5 and 2.6, films deposited at 1 mTorr are found to be FM without any magnetic transition, because they are near 46 at.% Rh composition.

2.5 Magnetic characterization

The magnetic properties of FeRh thin films were measured by SQUID magnetometry in a Quantum Design MPMS. First, measurements of magnetization as a function of temperature and field were performed to characterize the films for comparison with existing literature. From this data, the dependence of transition temperature on applied field was determined, which in turn allows comparison of macroscopic measurements recorded in magnetic field to microscopic observations performed in no magnetic field. Finally, the magnetization of FeRh at room temperature was studied, revealing the presence of a residual FM phase, which is relevant to the microscopy study as well as the interfacial study and was analyzed.

The temperature dependence of the magnetization was recorded to characterize the AF-FM magnetic phase transition at the macroscopic level in a constant external magnetic field. The magnetic properties of the FM phase were studied by recording magnetization M as a function of field H at 400 K, the maximum temperature of the MPMS. Figure 2.6 shows the $M(H)$ at fixed T and $M(T)$ at fixed H characteristics of FeRh films deposited at 600°C, 2 mTorr Ar and 40 W DC power. The following data treatment was done: background subtraction of MgO substrate diamagnetic background by linear fit of high field portions of $M(H)$ hysteresis (not shown) where the substrate signal dominates. Note that some erroneous data points were removed in the middle of the $M-T$ transition. They result from the difficulty for the MPMS fitting routine to accurately determine the total magnetic signal which is near 0 emu in this region due to the compensation between the negative signal from the substrate and the positive signal from the film.

Samples 1 and 2 were synthesized under the same conditions and have similar compositions of 49 and 50 at.% Rh (small difference in composition due to composition drift over time, discussed in Sec. 2.6). After normalization to the volume of the film, similar magnetization values at 1000 Oe field are respectively determined in Fig. 2.6 (a): 1100 emu/cc (note that the saturation magnetization M_s = 1130 emu/cc is reached at 2 T) and 1230 emu/cc. These magnetization values correspond to atoms carrying on average an atomic moment of 1.58 and 1.77 μ_B, regardless of their Fe or Rh chemical species. The difference could be due to the small change in Rh composition, but both values are in good agreement with values reported in the literature for thin films (e.g. 1.52 μ_B [21] and 1120 emu/cc [7]). Moment per atom reported for bulk samples range from 1.85 to 2.07 μ_B/at. [3, 42, 43].

The $M-T$ hysteresis is shown for each sample on separate panels in Fig. 2.6

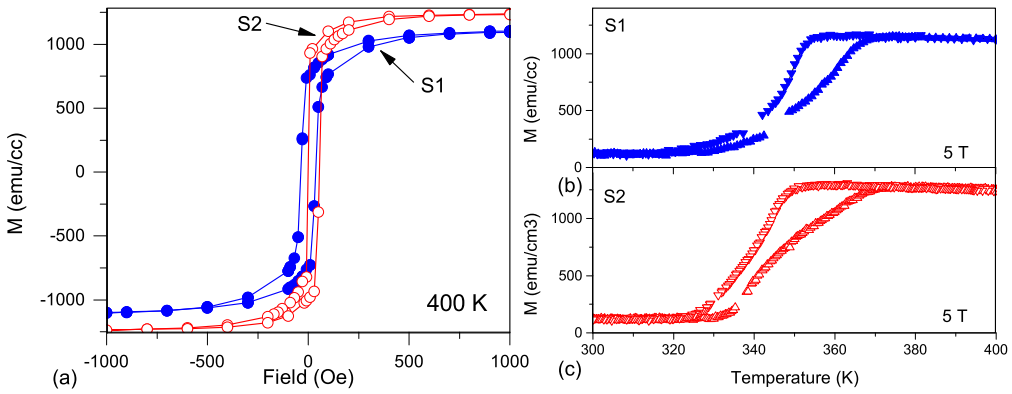

Figure 2.6: (a) Field hysteresis and (b, c) temperature hysteresis of the magnetization in representative FeRh films of composition 50 (S1 - blue) and 49 at.% Rh (S2 - red), grown with the standard parameters 600°C, 2 mTorr, 40 W.

(b) and (c). We find that for both samples, the transition proceeds between 325 and 370 K at 5 T, with a hysteresis of about 10 K in the middle of the transition and a broadening, defined as the temperature spread between the beginning and the end of the transition, of 30 to 40 K. Both samples exhibit a strong asymmetry in the shape of the macroscopic $M(T)$ curve at fixed field between heating and cooling. The small temperature shift between the two $M(T)$ curves is due to the 1 at.% difference in Rh composition.

$M-T$ hysteresis were recorded with externally applied magnetic field ranging from 1 T to 5 T. For a given sample, the transition temperature decreases with increasing magnetic field [6, 7]. The shift of the transition temperature with applied field was experimentally measured on a series of samples with varying deposition pressure and rate. Similarly to the study by Maat *et al.* [7], additional transition data in the $H-T$ phase diagram was obtained by doing magnetic field sweeps at a fixed temperature chosen in the transition region. Indeed, the AF-FM transition is metamagnetic and can be driven by both H and T. Figure 2.7 shows the H-T diagram constructed using T_{AF-FM} and T_{FM-AF} from the $M-T$ curves of three samples, with the transition temperature here defined for simplicity of analysis as the inflection point (or maximum of derivative dM/dT). The three selected FeRh thin films were deposited at 600°C but differ in the other deposition parameters: 4 mTorr Ar, 50 W (reference 52 at.% Rh), 4 mTorr Ar, 40 W (similar composition 51.5 at.% Rh but lower rate) and 2 mTorr Ar, 50 W (same rate as reference but different composition 48.5 at.% Rh).

Linear fits to the AF-FM and FM-AF boundaries for the different samples, give an average slope of -7.9±0.3 K/T, in good agreement with the existing literature [7]. The change in slope is minimal with change in either deposition rate or Ar pressure. On

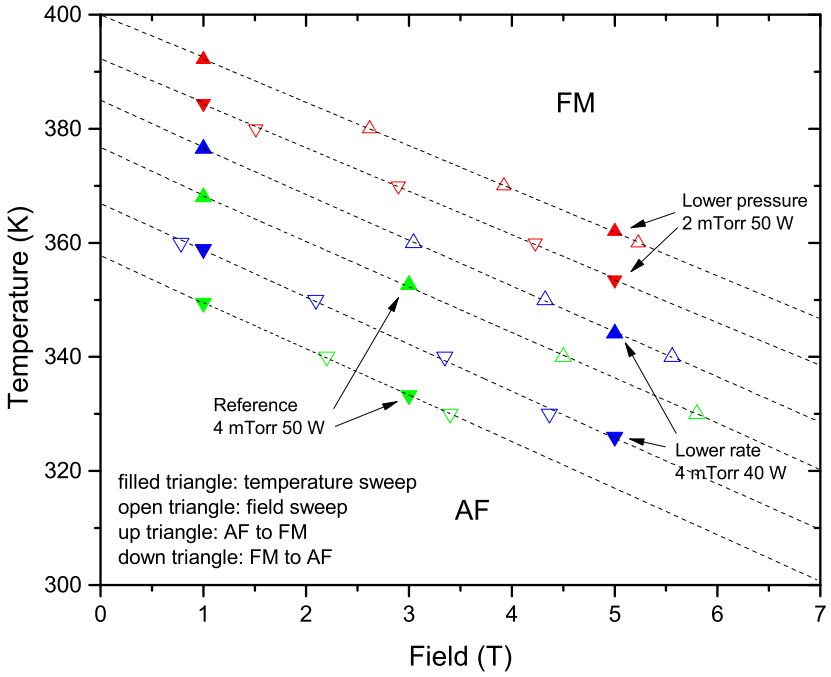

Figure 2.7: Field-temperature phase diagram of FeRh thin films with varying deposition parameters: 4 mTorr Ar, 50 W (reference 52 at.% Rh - green); 2 mTorr Ar, 50 W (different composition 48.5 at.% Rh - red); 4 mTorr Ar, 40 W (similar composition 51.5 at.% Rh but lower rate - blue). All films deposited at 600°C. Up (down) triangles correspond to the AF to FM (FM to AF) transition. Filled symbols are used for data obtained from temperature sweeps ($M(T)$ at constant H) and open symbols are used for data obtained from field sweeps ($M(H)$ at constant T).

the other hand, large shifts are observed in the intercepts at zero field of the different samples. The largest shift is seen between the films with different compositions (52 at.% Rh and 48.5 at.% Rh). The effect of composition on T_0 will be further discussed in Sec. 2.6 and will be used to propose an updated partial phase diagram. Note that a small shift in T_0 is also caused by a difference in deposition rate. Although we did not observe any change in coherence length, mosaicity, chemical ordering and tetragonal strain with deposition rate, there must be a difference between the two samples. We suggest that the degree of chemical homogeneity, which is susceptible to vary with deposition rate, can cause small shifts in T_0. This shows that the AF-FM transition in FeRh is extremely sensitive to the structural and chemical properties of the system.

While the magnetization is small in the AF phase as shown in $M - T$ curves in

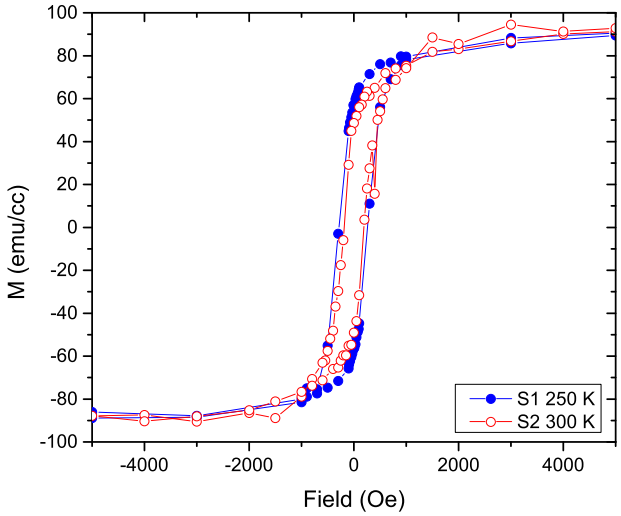

Figure 2.8: M(H) data of representative FeRh thin films recorded at 300 K (S1 50 at.% Rh - blue) or below (S2 49 at.% Rh - red), in the nominally AF phase. Both films were grown with the standard parameters 600°C, 2 mTorr, 40 W.

Fig. 2.6 (b) and (c), it is not zero. To better understand this, $M - H$ hysteresis curves were recorded in the AF phase at 300 K, both before and after an $M - T$ sweep. As shown in Fig. 2.8, for all our films of ∼100 nm thickness, a residual FM phase is found in the nominal AF phase, below the AF-FM transition temperature, with a saturation magnetization around 90 emu/cc.

This has been observed by other groups as well [21, 30, 44] but its origin is not fully understood. The possible sources are: (1) a residual chemically disordered bcc phase distributed through the entire thickness of the film and FM at all temperatures below the Curie temperature, (2) a FM layer situated at either top or bottom interface (or both), where the chemical ordering and/or the strain state of the film is different from the bulk of the film, possibly stabilizing a FM phase at room temperature. The magnitude of this magnetic contribution was verified on sample 2, deposited under the same conditions, and is found to be identical, showing that it is reproducible for a given set of deposition parameters and a given thickness.

FM layers at interfaces with capping layers and the substrate have been previously observed [21] and will be studied in details in Chapter 6. In an effort to determine if the entirety of the magnetic signal originates from these FM interface layers, we compare two films of different thicknesses. Fig. 2.9 shows the $M(H)$ hysteresis recorded in the nominally AF phase near room temperature, for 18 nm and 85 nm thick FeRh thin films deposited under the same conditions. The magnetic moment of the film has

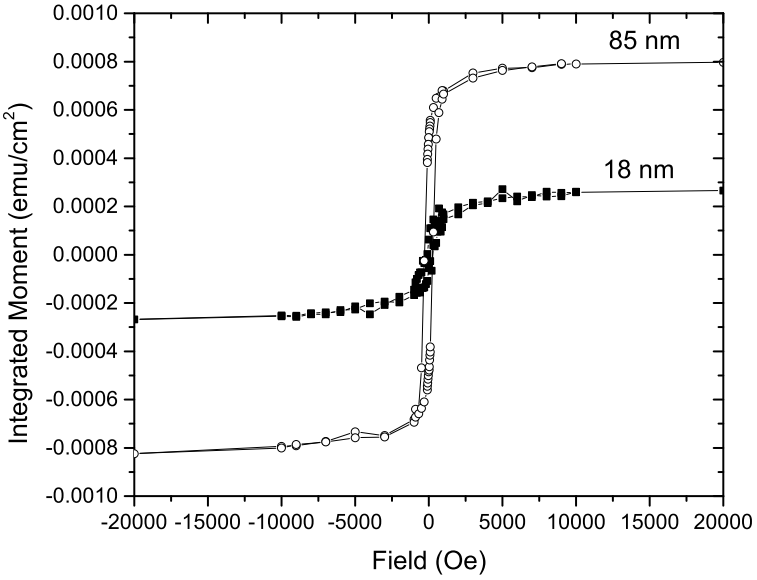

Figure 2.9: $M(H)$ hysteresis of 18 nm (filled squares) and 85 nm (open circles) FeRh thin films near room temperature, in the nominally AF phase. Both films were grown with the standard parameters 600°C, 2 mTorr, 40 W. The integrated moment is the total moment divided by the surface area of the film.

been normalized by the surface area only, instead of the volume, so as to represent an "integrated moment" in emu/cm^2.

The saturation magnetization M_S is reached at 2 T. The 18 nm film has $M_S = 2.6720\times10^{-4}$ emu/cm^2 and the 85 nm film has $M_S = 8.1068\times10^{-4}$ emu/cm^2. We assume that the two films have the same interfacial layers, therefore after subtraction of the thinner film to the thicker film, any residual FM signal is distributed through the entire 67 nm left. A residual magnetization of 81 emu/cc is determined. A magnetic signal originating from the top and/or bottom interfaces only would result in the same integrated moment for all films, regardless of their thickness. The residual magnetic signal corresponds to 7 % of M_S of the FM CsCl phase (1130 emu/cc) which is in good agreement with the fraction of disordered phase estimated from the chemical order parameter S according to

$$r_{Rh} = F_{Rh} + (1 - F_{Rh})S \tag{2.7}$$

with r_{Rh} the fraction of Rh site occupied by the right atoms and F_{Rh} the fraction of Rh atoms in the alloy [31]. The fraction of disordered phase is equal to $1 - r_{Rh}$ and ranges from 5 to 7 % for films deposited under the same standard conditions. We

then conclude that the residual FM signal in nominally AF FeRh thin films is due to a combination of interfacial effects and a small residual fraction of FM chemically disordered bcc phase.

2.6 Phase diagram

Background

Following the discovery of the unusual magnetic transition in equiatomic FeRh by Fallot *et al.* in 1938 [1], several groups focused on the change in T_0 and magnetic and structural properties as a function of Fe to Rh ratio. A series of papers from the 1960's studied bulk samples of different compositions near the equiatomic ratio towards the elaboration of a phase diagram. [2, 3, 42, 45, 46]. The sample preparation differs from group to group, with high temperature anneal ranging from 950°C to 1200°C for a few hours up to a day and subsequent heat treatment of either a slow furnace cooling or a water quench. As a result, samples with varying homogeneity in structure and composition are obtained. In particular, the presence of a residual fcc γ phase and the effect of quenching on the chemical order are debated. Note that the chemical ordering parameter was not reported, but simply qualitative statements on the chemical order were made such as "well ordered" and "highly ordered" [3, 46], therefore it is likely that the chemical order vary from sample to sample, thereby inducing uncertainty in the phase diagrams reported. Based on all this work and a few additional later reports, Swartzendruber proposed in the 1980's an updated phase diagram for the Fe-Rh system over the full range of composition [6]. This diagram as referenced in the ASM International Alloy Phase Diagram Database^{TM} is reproduced in Fig. 2.10 [47].

10 years later Takahashi *et al.* [16] showed that samples with the slow cool heat treatment had a broader transition than samples obtained by fast quench. From the study of their quenched samples they suggested a correction to the original phase diagram. A portion of the two phase diagrams proposed are shown in Fig. 2.11.

While both phase diagrams agree qualitatively for the location of the Curie transition and the γ fcc phase region at high temperature, the details of the location of the FM to AF transition are quite different. According to Swartzendruber the transition temperature increases with increasing Rh composition from 48 at.% to 55 at.% and then decreases sharply. According to Takahashi *et al.* the transition temperature increases with a higher slope from 47 at.% to 49 at.% and then decreases with a similar slope from 49 at.% to 51 at.%. Both show that the maximum transition temperature is around 395 K and that away from the maximum towards lower Rh composition, the AF phase α" transforms into the FM phase α' upon heating, while on the higher Rh composition side, the α" phase transitions into a two phase region of α" and γ. Note that Takahashi *et al.* do not specifically indicate the boundary between α' and α" in the two phase region with γ.

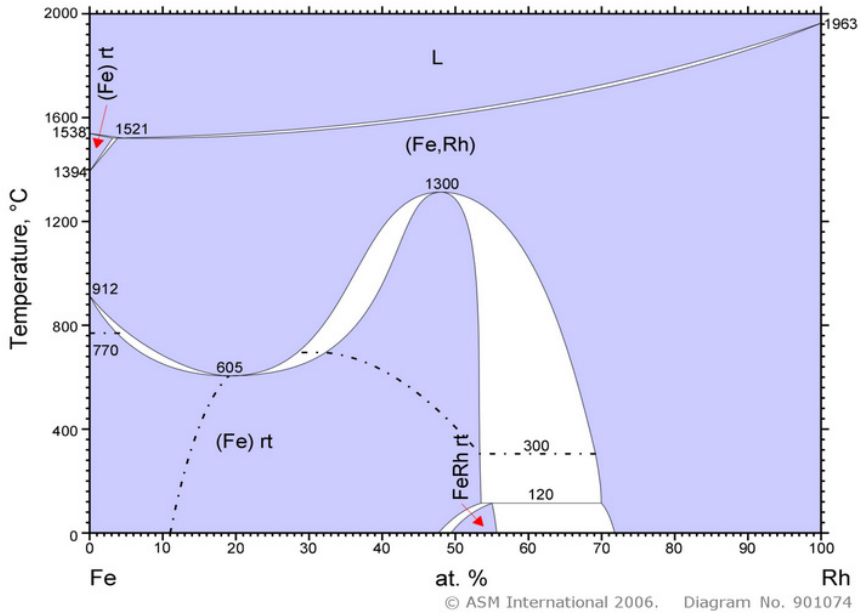

Figure 2.10: Fe-Rh Phase Diagram (1990 Swartzendruber L.J.) reproduced from ASM Alloy Phase Diagrams.

Proposed phase diagram

Controlling the Ar sputter pressure during our thin-film deposition process allows us to control the composition of the film. Further, for a given pressure, a composition drift was seen in the samples over time (estimated at 0.05±0.03 at.% per micron of film deposited). Films deposited close in time but at different pressure or at the same pressure but later in time cover the composition range of 48 at.% to 52 at. % Rh.

In an attempt to propose an updated region of the phase diagram, we turn to literature data of both bulk and thin film samples. After careful review of the bulk data referenced by Swartzendruber, only temperature/composition data sets for which the structure was determined by x-ray diffraction and the magnetic transition measured by magnetometry was selected [3, 45, 46, 48]. Additionally, from 2003 to 2013, a large amount of work has been reported on FeRh in thin-film form. A review of the literature was performed and to eliminate structural and strain effects that could affect the transition temperature, only thin films with a minimum thickness of 50 nm grown on MgO substrates were selected. Further selection of reliable data sets was based on the following criteria: the broadening of the transition was 50 K or less, the chemical composition was explicitely analyzed and the magnetic field applied during the $M-T$ measurement of the transition was clearly stated. Most of the data sets selected through this process are for samples fabricated by sputter deposition followed by a high temperature anneal and for which the composition was determined by RBS [7, 8, 9, 14, 28]. Error bars for all data points are added to take into account

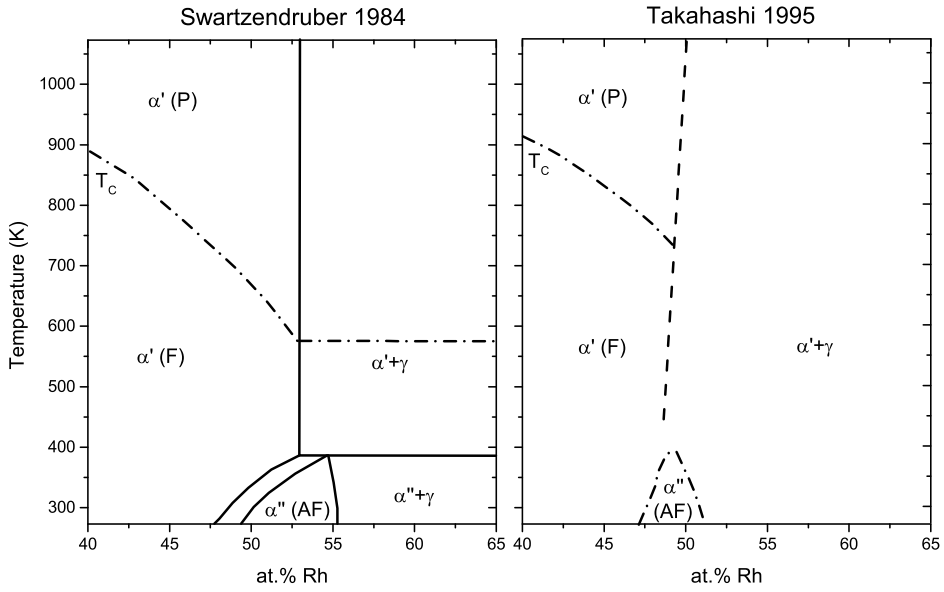

Figure 2.11: Binary phase diagrams of the Fe-Rh system proposed by Swartzendruber in 1984 and Takahashi *et al.* in 1995. The portion of the diagrams shown here is limited to the temperature range of 273 K to 1073 K and Rh composition range of 40 at. % to 65 at. % and contains the region of interest in which ordered FeRh experiences the 1st order magnetic phase transition.

the limited accuracy of the method of composition determination and any inaccuracy of the temperature measurement due to the breadth of the transition (the FWHM of derivative of $M(T)$ was used).

Figure 2.12 shows the comparison between our thin-film data and our selection of the existing literature data both on thin-film and bulk samples. The temperature plotted here is the average of the transition temperature upon heating and cooling, which are defined as the temperatures at which the magnetization reaches half of its maximum value, respectively upon heating and cooling. The combination of our data and the reference data agrees poorly with both existing phase diagrams which are outlined on the plot for reference. Instead, by using our error bars to draw boundaries to our data and extrapolating at higher at.% Rh, we propose an AF region which ranges from 47.5 at.% to 56 at.% Rh. The maximum transition temperature observed is around 397 K at 48.5 at.% Rh and is consistent with Takahashi *et al.*. Our update also qualitatively agrees with their diagram in showing that the transition temperature then decreases from the maximum value for higher Rh concentrations.

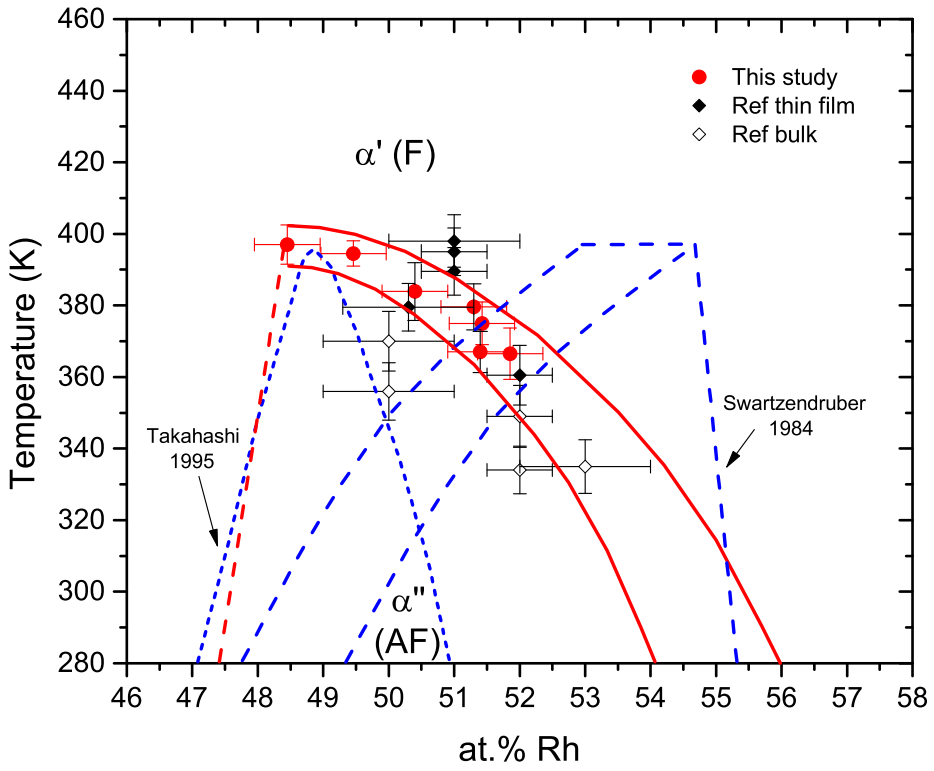

Figure 2.12: Proposed update (solid red lines) to the equiatomic region of the Fe-Rh phase diagram based on experimental measurements of single crystal thin films. Blue dashed (dotted) lines are for proposed phase boundaries (Swartzendruber and Takahashi respectively) from the literature.

On the lower Rh concentration on the other hand, a sharp decrease is observed as we have found that samples of composition 47.5 at.% Rh or lower are fully FM with no magnetic transition observed down to cryogenic temperatures. We suggest that the selected existing data, both bulk and thin film is in better qualitative agreement with our proposed diagram.

In the two-phase region shown on the diagram, at thermodynamic equilibrium, two phases with different composition given by the tie-line construction and the lever rule co-exist. In our measurement, we are not able to observe chemical separation of the two phases, instead we assume that the AF and FM phases have the same fixed composition. Therefore the diagram proposed is not the thermodynamic equilibrium diagram. Finally, we want to address the $\alpha + \gamma$ two-phase region. No γ phase was found in our samples from x-ray diffraction phase determination at room temperature.

This suggests that the $\alpha+\gamma$ region is not connected to the AF phase region but instead starts at composition 56 at.% Rh or above.

Chapter 3

Simulation and design of x-ray transparent heater stages

3.1 Introduction

The advancement of X-ray optics has allowed spatially resolved X-ray spectromicroscopies using synchrotron light. These powerful analytical techniques provide information such as chemical state, phase identification and structure determination at a local level in thin films and other nanomaterials. Temperature dependent in-situ measurements allows chemical, phase and structural analysis in real time. Microfabricated heaters have been used for in-situ experiments in a transmission electron microscope [49] and for in-situ catalysis experiments in a scanning transmission X-ray microscope [50], but most in-situ temperature dependent experiments still rely on traditional massive heater stages that require large amounts of power and are slow to stabilize.

Microfabricated membrane-based microcalorimeters have been used for well over a decade to study the thermodynamic properties of thin films and small samples [51]. Our group recently reported a scaled down design: a nanocalorimeter with an amorphous silicon nitride membrane as thin as 30 nm [52]. Figure 3.1 shows a top view micrograph of a typical nanocalorimeter. It consists of a silicon frame with a thin amorphous silicon nitride membrane, a platinum resistor heater and an ensemble of platinum and niobium-silicon alloy resistor thermometers on top. The central part of the membrane constitutes the sample area where for example a thin film can be deposited on the backside. The Pt resistor heater has heater line-width = 12 μm and spacing between heater lines = 68 μm.

The thinness of the membrane makes our nanocalorimeter a good candidate for a portable X-ray transparent platform with low power heating, rapid thermal response, and built-in temperature sensing capabilities. This new device offers a range of applications to temperature dependent spectromicroscopy studies in sensitive equipment

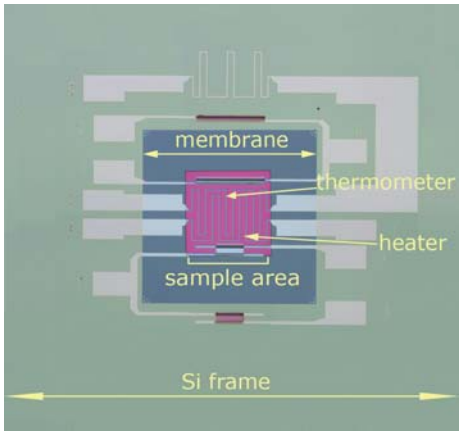

Figure 3.1: Micrograph of the nanocalorimeter. The Si-N membrane (2 mm by 2 mm) and the sample area (1 mm by 1 mm) are indicated. The arrows point to the Pt heater and thermometer. The other features on the sample area are additional thermometers and the features on the Si frame are matching thermometers to allow differential temperature measurements. The full device can be cleaved to fit on a 5 mm by 5 mm chip but the standard 10 mm by 10 mm chip is usually used.

that do not support macroscale heating of a sample platform. Applications include measurement of structure and magnetic domain changes at a phase transition and real time imaging of annealing effects on microstructure for materials ranging from magnetic films to polymers and photovoltaic thin films. For these applications, the sample area can be cycled between room temperature and hundreds of degrees in less than a second with mW of power while the frame of the device remains at room temperature. The temperature of the sample area can be measured either by the resistance of the heater itself or by one of the thermometers, allowing feedback control of the temperature.

The method used for calorimetry is based on small increases of sample area temperature above the base temperature of the frame T_0 (the so-called small-ΔT relaxation method, performed in high vacuum [53]). Many of the temperature-dependent spectromicroscopy applications require large ΔT. In addition, the typical environment of an X-ray microscope ranges from high vacuum to atmospheric pressure. We have previously performed simulation work to understand the thermal uniformity and heat transfer behavior of our device in vacuum and in the small ΔT regime for both thin films [54] and small bulk samples [55]. For spectromicroscopic applications, the high temperature and non-vacuum environment require that heat loss by radiation and by conduction and convection through the gaseous environment be taken into account and the consequences on the temperature uniformity of the sample area be investigated.

In this article, we first show experimental characterization of the thermal behavior

of our device in both vacuum and air with large ΔT. Then we present the numerical model that is used to simulate the steady-state temperature distribution in which heat loss contributions from conduction, radiation, and convection are analyzed. Small ΔT and large ΔT, and effects of radiation, convection and gas pressure will be discussed. Results of simulation will be discussed and used to suggest a new design. The new design has been fabricated and thermally characterized; results will be discussed.

3.2 Experimental measurement of power and temperature

Power versus temperature measurement

First we characterize how the power dissipation is affected by the environment (e.g. vacuum or non-vacuum) for large ΔT. The temperature of the sample area $(T_0 + \Delta T)$ here is measured by the resistance of the heater itself. The first step is to calibrate the resistance versus temperature, $R(T)$, of the Pt heater. This is done in a vacuum cryostat with the Si frame attached to a sample block which has an external heater and calibrated thermometer. The sample block temperature, T_0, is raised incrementally, and the resistance of the thin-film Pt heater is measured by a 4-wire measurement. The current I used in this $R(T)$ calibration measurement is kept small to prevent self-heating. Next, keeping the sample block and Si frame's temperature constant at some T_0, another 4-wire measurement is performed where the current I to the heater is incrementally increased, raising the temperature of the device Pt heater while the voltage V across the Pt heater is monitored. The temperature of the sample heater $(T_0 + \Delta T)$ is then determined from $R = V/I$ using the calibration curve. The power P dissipated by the sample heater is calculated from $P = VI$.

Figure 3.2 shows a measurement of the change in heater temperature ΔT as a function of power for different T_0 and in both air and vacuum. The curves labeled "vacuum" were taken in a high vacuum cryostat with a pressure of 4×10^{-7} Torr with the sample block held at different base temperatures T_0 ranging from 200 K to 363 K. ΔT decreases with increasing T_0 due to increasing thermal conductivities of the Si-N membrane and Pt leads with temperature. The curves labeled "air" were taken in air at atmospheric pressure with the sample block held at room temperature or on a hotplate with T_0 ranging from 323 to 363 K. These ΔT data also decrease with increasing T_0.

A large difference in power is observed between the thermal behavior of the device in vacuum and in air. As will be later detailed, this dramatic difference is due to heat transfer through the air. In vacuum, 0.4 mW is sufficient to reach ΔT=100 K at T_0 = 295 K. In air, the device reaches the same ΔT=100 K with 15 mW of power.

In this experiment, the temperature measured is the average heater temperature $\Delta T_{av,h}$. For small ΔT in vacuum, we have previously shown that the sample area is

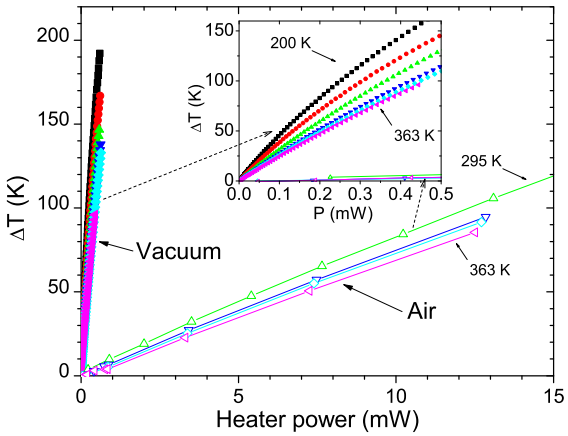

Figure 3.2: Measured temperature rise ΔT of heater from $R(T)$ calibration versus power P for a nanocalorimeter in vacuum and in air. As shown in Section 3.2, in vacuum, this is the sample area average temperature; in air, because of sample area thermal inhomogeneities, this is the average heater temperature $\Delta T_{av,h}$. Inset: same data on an expanded scale to more clearly show the data in vacuum. Sample block temperatures: $T_0 = 295$ K, 323 K, 338 K, 363 K. Additional temperatures in vacuum: $T_0 = 200$ K, 250 K.

isothermal to 2% of ΔT and the sample area average temperature is then the same as $\Delta T_{av,h}$. But in situations as described in this paper (large ΔT in air), non-uniformities in temperature in the sample area are found, resulting in $\Delta T_{av,h}$ being different from the sample area average temperature, and this measurement lacks information about the spatial temperature distribution.

Microscale thermography provides a complete spatial temperature distribution of the sample area which can then be compared to 2D simulation results presented in Section 3.3. However, limitations of the thermography techniques used, which are inherent to the specifics of our device, were discovered and will be discussed.

Two complementary microscale thermography techniques were used to perform thermal imaging of a nanocalorimeter in air: infrared microscopy and thermoreflectance microscopy [56]. Materials that are good reflectors can be easily imaged by thermoreflectance microscopy, while materials that are good emitters can be easily imaged by infrared microscopy. The membrane, consisting of thin highly transparent Si-N, is not suitable for either of these imaging techniques. Because we are unable to directly measure its temperature the Si-N outside of the sample area is not shown. Metal films (Pt heater and thermometer on the front, or Au film on the back, commonly used in our group to provide a thermal equilibration of the sample area) allow us to use these techniques to measure the sample area temperature distribution. Thermal images of the sample area of the nanocalorimeter with a 50 nm Si-N membrane and a 45 nm Au layer on the back using both techniques are shown in

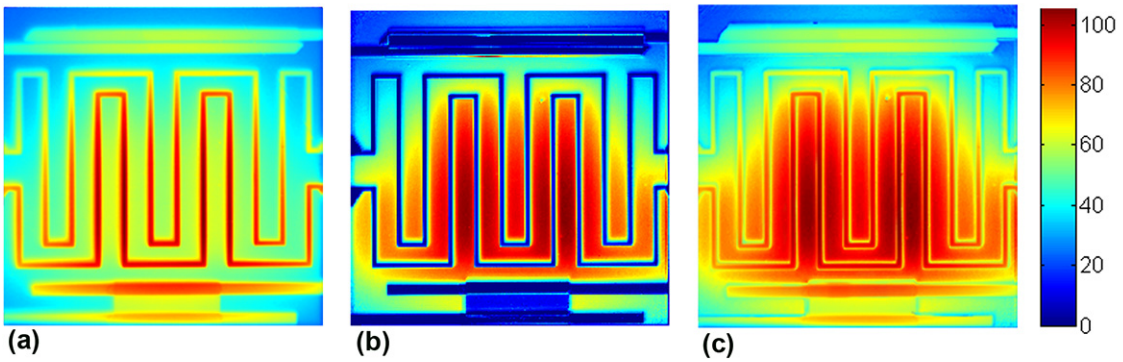

Figure 3.3: Experimental thermal maps showing ΔT of the sample area of a nanocalorimeter with a 45 nm Au thermal conduction underlayer, a 50 nm Si-N membrane and 50 nm Pt heaters and thermometers, obtained in air by (a) infrared thermography with heater power of 12.4 mW and an elevated base temperature $T_0 = 90°C$ to improve infrared emission, (b) thermoreflectance microscopy with heater power of 11.5 mW and a base temperature of $T_0 = 23°C$. Figure 3.3 (a) shows ΔT for Pt only due to low emissivity of Au and Figure 3.3 (b) shows ΔT for Au only due to low thermoreflectance coefficient of Pt. ΔT color scale is shown on the right of each image.(c) Composite image of the Pt area from image (a) and the Au area from image (b), as explained in text.

Figure 3.3 and discussed in Sections 3.2 and 3.2.

Infrared microscopy

Infrared microscopy measures the infrared thermal radiation (mid-wavelength infrared radiation 2 to 5.5 μm) emitted from the different areas of the device with a spatial resolution of 2 to 4 μm and a thermal sensitivity better than 0.1 K [57]. In addition it provides experimental emissivity parameters needed in the simulation. In particular this measurement shows that the Si-N has a low emissivity, contrary to what was assumed in previous work. Figure 3.3 (a) shows a thermal map obtained by infrared microscopy. The measurement was performed at an elevated base temperature $T_0 = 90°C$ to increase detection efficiency and image quality.

The first step is to calibrate the image by determining the materials' emissivity. This is done for each pixel by comparing the measured radiance to a blackbody reference. This calibration step assumes that the transmitted component is negligible. This assumption is not valid for the transparent Si-N membrane and even the metal layers are partially transparent at these wavelengths due to their thinness (40-50 nm). As a result the infrared calibration measurement overestimates the emissivitites of the Pt and Au areas of the device and therefore underestimates the temperature.

The measurement works best for the Pt layer (corresponding to the heater and one thermometer) as it is the thickest layer on the membrane and the least transparent. The backside Au layer is too thin to give a good infrared image and so it appears much colder (i.e. closer to the 90°C of the stage). The relative temperatures of the Pt regions are accurate to 0.4 K. In order to measure absolute temperatures, we must correct for the overestimation of the Pt emissivity and the consequent underestimation of the absolute temperature. The emissivity of Pt was measured to be $\epsilon^{Pt} = 0.155$ and is corrected to $\epsilon^{Pt} = 0.12$, as explained in Section 3.3.

Thermoreflectance microscopy

Thermoreflectance microscopy enables thermal mapping with a sub-micron spatial resolution and a thermal sensitivity as low as 0.01 K [58, 59]. It measures a relative change of reflectivity $\Re$ as a function of temperature. This change is small for most materials, but it is larger for Au than Pt by over an order of magnitude. It therefore provides a good thermal map of the Au thermal conduction layer and is shown in Figure 3.3 (b) which displays a non-uniform temperature distribution of the Au. Since the image is not calibrated pixel by pixel, but rather with one single value corresponding to the Au, both the Pt and Si-N appear cold due to much smaller change in $\Re$. In our measurement the change of reflectivity of the Pt and Si-N layers is lost in noise.

The relative temperatures of the Au regions in Figure 3.3 (b) are accurate to 0.5 K. In order to put an absolute temperature scale onto the Au data in Figure 3.3 (b), we need the thermoreflectance coefficient $d\Re/dT$. In addition to being material-dependent, the thermoreflectance coefficient $d\Re/dT$ is also wavelength dependent and is strongly affected by interferences with covering layers. The literature value of $d\Re/dT = -2.2 \times 10^{-4}\mathrm{K}^{-1}$ for bare Au. This value and the non-monotonic effect of overlayers is discussed in ref. [60]. Au covered with the 30 nm Si-N membrane was found in our experiment to have $|d\Re/dT| = 8.5 \times 10^{-4}\mathrm{K}^{-1}$ at a wavelength of 470 nm. Note that in this experimental set-up, only absolute values of $d\Re/dT$ were obtained. The error bar is associated with a visible variation across the sample area during the calibration procedure. Figure 3.3 (b) was taken with a 50 nm membrane. To get the value of $d\Re/dT$ for this sample, we use the heater $R(T)$ calibration, from which we calculate $\Delta T_{av,h}$ and from this and the data in Figure 3.3 (b), we derive $d\Re/dT = -3.6 \times 10^{-4}\mathrm{K}^{-1}$, which is within the expected range.

Figure 3.3 (a) therefore provides the temperature distribution of the Pt heater and thermometer with $T_0 = 90°\mathrm{C}$ and Figure 3.3 (b) the temperature distribution of the Au thermal conduction layer with $T_0 = 23°\mathrm{C}$. Both data sets are taken in air and show that the central sample area has a reasonably uniform temperature. A similar $\Delta T = 100\mathrm{K}$ is achieved for both measurements. The temperature distributions are similar, with small differences due to differences in base temperature T_0, heater power and environment between the two measurements. A composite image is constructed

by combining the Pt area from the infrared microscopy experimental map with the Au area from the thermoreflectance microscopy experimental map in Figure 3.3 (c). The two complementary techniques were combined to obtain the complete thermal characterization of the nanocalorimeter.

3.3 Simulation

Parameters determination

In order to model the heat transfer behavior of our nanocalorimeter used as a heater stage, we must take into account conduction heat transfer and two other significant contributions to heat loss not included in the 2D numerical simulation model previously reported [54] and [55]: radiation and convection / conduction through the gas. The first conduction term represents the heat lost by conduction through the different layers of materials that constitute the device and is modeled by the linear Fourier's law. The heat lost by radiation is non-negligible above 100 K and is modeled based on the Stefan-Boltzmann law of blackbody radiation $P = A\sigma\epsilon T^4$ making it a non-linear term in the equations. Finally, the heat lost by convection and conduction through the gas can be approximated by a term that is linear in ΔT, using a coefficient h determined by empirical correlations [61].

Therefore the steady-state heat equation has the form:

$$-\nabla \cdot (k_{2D}\nabla u) + hu + \sigma\epsilon\left((u+u_0)^4 - {u_0}^4\right) = P_{2D} \tag{3.1}$$

where $u = \Delta T$, k_{2D} is the two dimensional thermal conductivity in W/K (thermal conductivity multiplied by thickness of film), h is the convection heat transfer coefficient in W$\cdot$ K$^{-1}\cdot$ cm^{-2} (including conduction through the gas), σ is Stefan-Boltzmann constant, ϵ is the emissivity, $u_0 = T_0$ is the base temperature (for example room temperature) and P_{2D} is the two dimensional power dissipated in the heater in W/cm^2. In this equation all parameters depend on x,y coordinates which represent the different elements of the nanocalorimeter. Two dimensional thermal conductivities are assumed to add in parallel; for example, where Au is on top of Si-N $k_{2D}^{total} = k_{2D}^{Au} + k_{2D}^{Si-N}$.

This two-dimensional non-linear partial differential equation is solved to give $u(x, y)$ with a finite element method using the MATLAB partial differential equation toolbox function `pdenonlin`. The following approximations from the previous simulation work are still assumed to be valid: (1) the 2D approximation (because the out of plane dimension is orders of magnitude smaller than all in plane dimensions) and (2) uniform dissipation of power at all x,y points in the Pt heater. In the simulation, the tolerance on the size of the residual at termination, which controls the accuracy of the computed solution, had to be increased to 10^{-12} in order for the non-linear solution to converge. Each contribution to Equation 3.1 is modeled by one or several parameters. First, we discuss how each parameter is determined, and then we will turn to the simulation results.

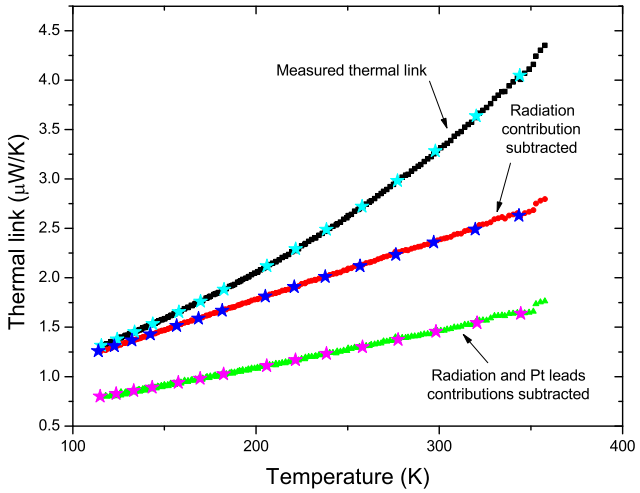

Figure 3.4: Thermal link of nanocalorimeter in vacuum $\kappa = P/\Delta T$ versus average temperature of the thermal link $T_0 + \Delta T/2$, comparison of experimental data taken with small-ΔT measurement (continuous lines) and simulation data using thermal conductivities and emissivities as explained in the text (star symbols).

Conduction

In order to determine the appropriate $k_{2D}(x, y)$ parameters, we turn to small-ΔT measurements in vacuum with different base temperatures. Figure 3.4 shows the thermal link of the nanocalorimeter $\kappa = P/\Delta T$ plotted as a function of its average temperature. In the limit of an isothermal sample area for small ΔT ($\Delta T \leq 0.01 T_0$), the average temperature of the sample area (Au layer) is $T_0 + \Delta T$ and the average temperature of the thermal link (Si-N membrane and Pt leads) is $T_0 + \Delta T/2$.

In vacuum, for small ΔT there are three different contributions to the thermal link between the sample area and the environment: conduction through the Si-N membrane, conduction through the Pt leads to the heater and thermometers, and the first order contribution to radiation, $A\sigma\epsilon T_0^3$. The contribution of conduction from Pt is calculated from a resistivity measurement of the Pt heater or thermometer using the Wiedemann-Franz law. The contribution from radiation is calculated from the cubic term of $\kappa(T)$. Both radiation and Pt contributions are subtracted from the measured κ to give κ^{Si-N} as a function of temperature. A detailed description of this analysis can be found elsewhere [62].

The simulation parameter k_{2D}^{Si-N} is adjusted until the simulated membrane contribution fits the experimental curve. The following relationship between the experimental thermal conductance and the two dimensional thermal conductivity used in the simulation is then determined: $\kappa^{Si-N} = 10.2 \times k_{2D}^{Si-N}$, where 10.2 is a geometric factor characteristic of the membrane, in good agreement with previous work [54]. The two dimensional thermal conductivity of the thermal conduction layer (in our case gold)

is calculated by $k_{2D}^{Au} = k^{Au} \times t$ with k^{Au} the thermal conductivity value reported in the literature [63] and t the thickness of the film. Note that we measured the electrical resistivity of the 45 nm Au thermal conduction layer and calculated the thermal conductivity to be k^{Au}=1.850 W$\cdot$ K$^{-1}\cdot$ cm^{-1} at 300 K using the Wiedemann-Franz law. This value is within a factor of 2 of the literature value used in the simulation (k^{Au}=3.17 W$\cdot$ K$^{-1}\cdot$ cm^{-1} at 300 K).

For the simulations to be used in this paper, a constant value of k_{2D} is assigned to each material layer. Including a temperature-dependent conductivity would vastly increase the computational time needed to iterate to a solution and for the limits examined in this work is not relevant. In vacuum for small ΔT ($\Delta T \leq 0.01 T_0$) at all T_0, k is to first order linear in T, so taking k as a constant value corresponding to the average temperature is correct. For example, the average temperature of the membrane is $T_0 + \Delta T/2$ so the value assigned for Si-N is $k_{2D}^{Si-N}(T_0 + \Delta T/2)$. In air at temperatures above room temperature the k_{2D} of all layers will be set to their value at T_0; this is a good approximation because temperature-dependent deviations in thermal conduction are negligible compared to the contributions from radiation and convection. This constant approximation would *not* be true for large ΔT at low temperatures, even in vacuum, and a more complete treatment of the thermal conductivity in a simulation would then be necessary [62].

Radiation

From the calibration done for the infrared thermography measurements shown in Section 3.2 we determined the emissivity of each material on the device. This revealed that the Si-N membrane is a low emitter compared to the metals due to its high transparency and thinness. The emissivity values of the metal layers were measured by infrared microscopy to be $\epsilon^{Au} = 0.085$ and $\epsilon^{Pt} = 0.155$, with the ϵ^{Si-N} much smaller than either. We therefore take the emissivity of Si-N to be zero and assume that only the metal layers on the device have a non-zero emissivity and radiate through the transparent Si-N. As discussed in the experimental section, emissivities determined by infrared microscopy were overestimated due to the partial transparency of all the materials. Not surprisingly, it is found that values smaller than the measured values are needed to obtain a good match between simulation and experimental data in Figure 3.4. The best match is achieved for $\epsilon^{Au} = 0.06$ and $\epsilon^{Pt} = 0.12$. These values also are in good agreement with values reported in the literature [64] and will be used in all the simulation results presented here.

Convection and conduction through the gas

There are three different regimes for heat loss through a gaseous medium for this geometry: a turbulent regime known as classical free convection, a laminar regime where conduction through the gas occurs very much like conduction through a solid,

and a molecular flow regime where the mean free path of the molecules exceeds the characteristic system size so heat is transfered by direct molecular impingement [36]. Using empirical correlations based on dimensionless parameters, the transition pressures between the different regimes were determined based on the characteristic length of our system (silicon frame thickness of 475 μm or Pt heater dimensions in the range of 300 to 500 μm).

The transition between laminar and turbulent regimes is determined by the Rayleigh number (See Appendix A for details). For our system, because of the small length-scale, the turbulent regime is estimated to occur well above 760 Torr so it is not accessible in our experimental conditions. The transition between laminar fluid flow and molecular flow is determined by the Knudsen number(See Appendix A for details). For nitrogen the transition is reached for $p \approx$140 mTorr, calculated for a characteristic length $d = 475$ μm. Variation of the characteristic length between 300 and 500 μm gives a transition pressure ranging from 230 mTorr to 130 mTorr.

In the laminar regime the convection coefficient h can be estimated by $h = 2 \times \frac{k}{d}$ with k the thermal conductivity of the gas and d the characteristic length of the system (factor 2 accounts for heat loss on top and bottom of the membrane). The thermal conductivity of gases is independent of pressure in this laminar regime. If we approximate air by its main constituent nitrogen ($k = 0.026$ W·K^{-1}·m^{-1} [63]) we find h=0.0109 W·K^{-1}·cm^{-2} at room temperature, calculated for $d = 475$ μm. Variation of the characteristic length between 300 and 500 μm gives a laminar regime convection coefficient h ranging from 0.02 W·K^{-1}·cm^{-2} to 0.01 W·K^{-1}·cm^{-2}.

In the molecular regime, the coefficient becomes highly pressure-dependent and decreases linearly with pressure. It is calculated from the molecular impingement flux $J(p)$ by $h = 2 \times J \times \frac{C_V}{N_A}$ with C_V the molar heat capacity of the gas and N_A the Avogadro constant [36] Å. For example, for a pressure of 10 mTorr, $h = 3.74 \times 10^{-4}$ W·K^{-1}·cm^{-2}.

We vary h to get the simulated $\Delta T_{av,h}$ to match the experimental $\Delta T_{av,h}$ calculated from the thermal maps. We obtain for
(a) infrared microscopy $h = 0.0151 \pm 0.0007$W·K^{-1}·cm^{-2} and for
(b) thermoreflectance microscopy $h = 0.0137 \pm 0.0006$W·K^{-1}·cm^{-2}.
With the above values well within the range of calculated laminar convection coefficient (0.01 to 0.02), experimental thermal maps shown in Figure 3.3 are well matched (further discussed in Section 3.4).

Simulation results

After determining the parameters of the model we simulate selected sets of conditions that cover the full range of applications of the device from small ΔT in high vacuum to large ΔT at atmospheric pressure. The isothermal contours of the calculated temperature solutions are shown in Figure 3.5. The frame T_0 is set to 295 K and 1% isothermal contours are shown. For each set of conditions a small $\Delta T_{av,h}$ of

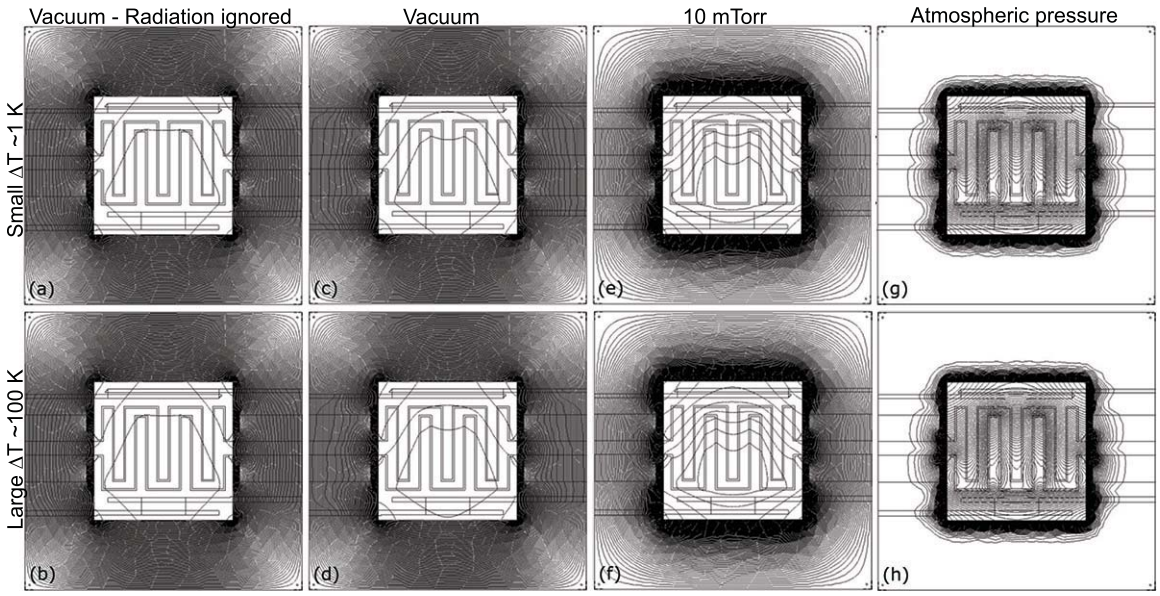

Figure 3.5: Comparison of simulations showing 1% isothermal contours for different operating conditions of the nanocalorimeter. Each layer of the modeled nanocalorimeter (Si-N membrane, Au thermal conduction layer and Pt heater and thermometers) is 50 nm thick. The base temperature $T_0 = 295$ K and the thermal conductivities input in the model are for 295 K for simplicity ($k_{2D}^{Si-N} = 1.434 \times 10^{-7}$ W/K, $k_{2D}^{Pt} = 5.824 \times 10^{-7}$ W/K and $k_{2D}^{Au} = 1.586 \times 10^{-5}$ W/K). The heater power ranges from 2.5 μW to 10.6 mW, chosen in each case to give a small $\Delta T_{av,h}$ of 1 K or a large $\Delta T_{av,h}$ of 100 K and is detailed in Table 3.1 with the other parameters used.

Simulation	(a)	(b)	(c)	(d)	(e)	(f)	(g)	(h)
ϵ^{Au}	0	0	0.06	0.06	0.06	0.06	0.06	0.06
ϵ^{Pt}	0	0	0.12	0.12	0.12	0.12	0.12	0.12
h	0	0	0	0	0.000374	0.000374	0.0109	0.0109
P_{2D}	0.0056	0.56	0.0080	0.90	0.021	2.1	0.25	25

Table 3.1: Parameter values used in the simulation presented in Fig. 3.5: emissivities ϵ^{Au} and ϵ^{Pt}, convection heat transfer coefficient h in W·K^{-1}·cm^{-2} and two dimensional power dissipated in the heater P_{2D} in W/cm^2.

1 K and a large $\Delta T_{av,h}$ of about 100 K are simulated. The heater power is adjusted to reach this $\Delta T_{av,h}$. The values of the different simulation parameters varied (heater power, emissivities and convection heat transfer coefficient) to obtain the results presented in Fig. 3.5 are summarized in Table 3.1 for completeness and clarity.

Figure 3.5 (a) and (b) were simulated using our previous model that ignored radiation (appropriate for the lower T_0 discussed there) [54]. The sample is shown to

be 3% isothermal (meaning that the 3% contour line is the highest contour that lies on corners of the sample area), slightly higher than the 2% previously reported at 20 K because the ratio of thermal conductivities $k_{2D}^{Au}/k_{2D}^{Si-N}$ is lower at 295 K than 20 K. No difference in thermal contour lines between the two different powers (corresponding to small ΔT and large ΔT) is observed in this linear model (no radiation). Note: this is observed because the thermal conductivities k are assumed independent of T in the simulation; differences are expected in large ΔT when including $k(T)$.

Figure 3.5 (c) and (d) show that by adding the radiation term the power required to reach $\Delta T = 1$ K and 100 K increases somewhat and is non-linear. The sample is now only 4% isothermal, and the contour lines slightly shrink toward the center with increased power, i.e. the value of the heater power now affects the thermal contour lines. These changes in power needed to reach $\Delta T = 1$ K and 100 K were seen experimentally in Figure 3.2.

Adding a convection term greatly increases the power required to reach $\Delta T = 1$ K and 100 K and great increases the thermal non-uniformity of the sample area, as can be seen in Figure 3.5 (e) and (f). In a N_2 pressure of 10 mTorr the sample area is now only 8% isothermal. The relative radiation loss contribution is diminished compared to the convection loss contribution; as a result the power needed to reach $\Delta T = 1$ K and 100 K is almost linear and only small changes are seen between small ΔT and large ΔT.

Finally, the power needed to reach $\Delta T = 1$ K and 100 K is 50 times greater than in vacuum. Figure 3.5 (g) and (h) show that in N_2 at 760 Torr, the convection heat loss is dominant. Most of the temperature gradient occurs on the sample area and the entire membrane is close to T_0. The power needed to reach $\Delta T = 1$ K and 100 K is linear and no difference can be seen between small and large ΔT regimes because at atmospheric pressure, the (linear) convection loss dominates the radiation loss.

3.4 Discussion

Vacuum

In vacuum, ignoring radiation and for small ΔT, we have previously shown that keeping the sample area better than 2% isothermal (a condition necessary for the relaxation method of heat capacity measurement to be valid) is achieved by using a thermal conduction layer of approximately the same thickness as the membrane [54]. Here we investigate if this still holds in the large ΔT regime, with and without radiation.

Figure 3.5 (d) shows that at room temperature, a nanocalorimeter with a Au thermal conduction layer as thick as the membrane is 4% isothermal. This is due to decreased $k_{2D}^{Au}/k_{2D}^{Si-N}$ at 295 K compared to earlier work at low T as mentioned in the previous section and to radiation heat loss.

Increasing the thickness of the thermal conduction layer is sufficient to recover the 2% isothermal criterion. For example 150 nm of Au is sufficient at a base temperature of 295 K for a large ΔT=200 K for a 50 nm Si-N membrane. We note however that 2% of 200 K represents a temperature gradient across the sample area of 4 K, which for some purposes is too large. At room temperature using a 150 nm Au thermal conduction layer the largest ΔT where the sample area will be 1 K isothermal is 50 K. The Au thickness must be increased further to maintain a 1 K accuracy at larger ΔT.

Atmospheric and other non high vacuum environment

In air the sample area becomes so non-isothermal that increasing the thickness of the thermal conduction layer is not a practical solution. Even for small ΔT, use of the current design as a heater stage requires an isothermal area large enough for X-ray spectromicroscopy and the ability to extract the temperature of that particular area. Simulated temperature profiles allow us to locate areas of interest on the current nanocalorimeter design and calculate their temperature. As explained earlier, the temperature measured experimentally is $\Delta T_{av,h}$. We calculate the equivalent in the simulation by averaging 176 points over the heater.

Figure 3.6 (a) shows a thermal map simulated in conditions corresponding to the thermoreflectance measurement (Figure 3.3 (b)). These conditions are similar to the conditions used in the thermal distribution simulated in Figure 3.5 (h) (large ΔT in air at 760 Torr). Using a coefficient h=0.0137 W·K^{-1}·cm^{-2}, a good match is achieved for $\Delta T_{av,h}$ between the experimental measurement and the simulation ($\Delta T_{av,h} = 90$ K). Comparison between experimental and simulated temperature profiles along the horizontal direction of the nanocalorimeter is shown in Figure 3.6 (b). Matching between the simulation and the experiment can be improved by increasing the coefficient h and decreasing the $d\Re/dT$ used in the thermoreflectance calibration in an iterative manner. Results from the first iteration are qualitatively good enough for the purposes of this work and are shown here.

Figure 3.7 shows simulated isothermal contours (same simulation as Figure 3.6). Two symmetric maximums in the temperature distribution are located along the heater. We can distinguish a large 1% isothermal area located between two thermometer segments, almost at the center of the device. Its temperature is 7 to 8% below the maximum temperature in the simulation, and 4% higher than $\Delta T_{av,h}$. A disk of diameter 50 μm fits in this area.

Since convection is the dominant term of heat loss, reducing it can result in substantial improvements in power consumption and uniformity of temperature distribution of the sample area. In some cases, this can be done by experimentally achievable intermediate pressures. Our simulation shows for example that the size of the largest 1% isothermal area increases by 50% when the pressure is decreased to 100 mTorr

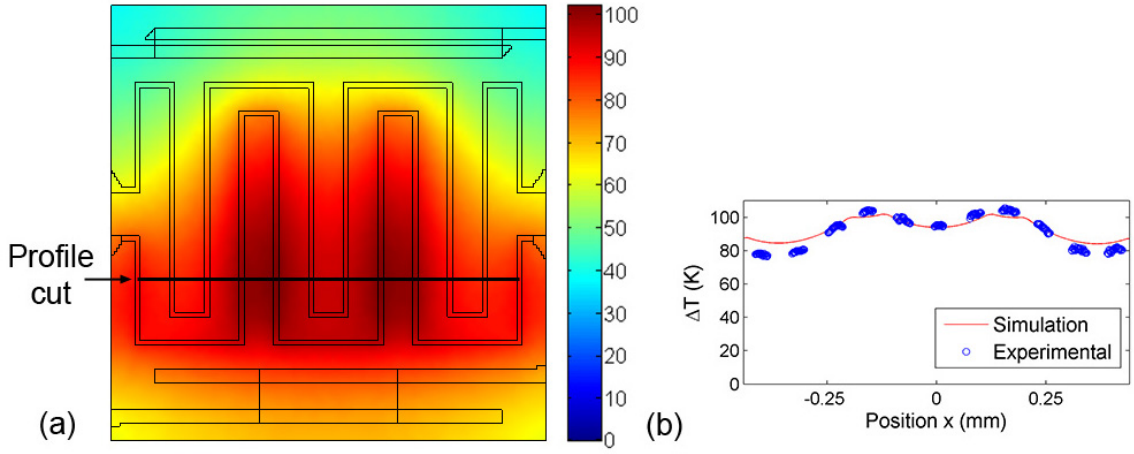

Figure 3.6: (a) Simulated thermal map with the following parameters chosen to match the thermoreflectance measurements of Figure 3.3: $T_0 = 295$ K, $k_{2D}^{Si-N} = 1.434 \times 10^{-7}$ W/K, $k_{2D}^{Pt} = 5.824 \times 10^{-7}$ W/K and $k_{2D}^{Au} = 1.427 \times 10^{-5}$ W/K, $P_{2D} = 27.1$ W/cm^2, $\epsilon^{Au} = 0.06$ and $\epsilon^{Pt} = 0.12$, h=0.0137 W·K^{-1}·cm^{-2} (large ΔT in air, similar to Figure 3.5 (h)). (b) Comparison of experimental and simulated temperature profiles along the horizontal profile cut indicated in (a). The experimental data points (blue circles) are from Au areas along the same horizontal profile cut of the experimental thermal map shown in Figure 3.3 (b).

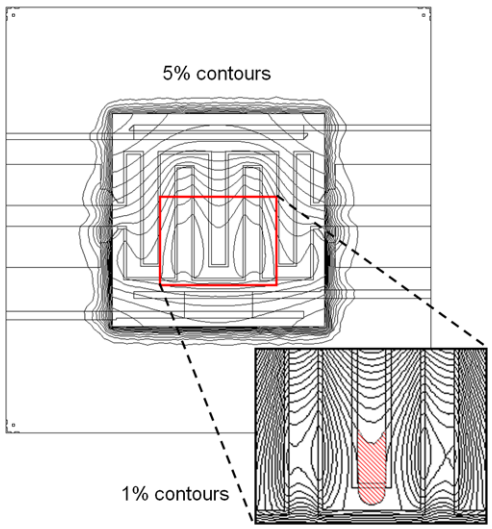

Figure 3.7: Isothermal contours simulated with the same parameters as Figure 3.6 (experimental conditions of thermoreflectance measurement). 5% contours are shown over the entire nanocalorimeter and 1% contours are shown in the expanded inset with the largest isothermal area highlighted.

(not pictured), and by more than a factor of 10 when the pressure is reduced to 10 mTorr, where the molecular flow convection regime is reached (Figure 3.5 (f)).

Improved design

Sections 3.4 and 3.4 show that the isothermal character of the calorimeter's sample area can often be improved by decreasing the background pressure and/or increasing the thickness of the thermal conduction layer, but in many cases these experimental conditions cannot be altered. Therefore, the intrinsic design of the heater stage needs to be improved for use as a versatile X-ray stage.

There are several current characteristics of the device that we would like to maintain as they fit the purpose of a portable X-ray transparent heater stage best. First, to maintain good X-ray transparency it is best to keep a similar design of a thin wire-like heater so that an X-ray beam can be focused on a small sample area without any additional metal layer. We maintain the same central square sample area so that both our nanocalorimeter and our heater stage are compatible with the same deposition mask used for the sample and a metallic thermal conduction layer [52]. The heater can serve the dual purpose of heater and thermometer. Finally, Pt is the ideal resistance temperature detector due to its linear behavior in the temperature range of interest and its excellent chemical stability at high temperatures, so we keep Pt as our heater and thermometer material.

We use experimental measurements and simulation to characterize the temperature distribution of an alternate heater geometry that consists of a double spiral Pt heater. The Pt heater line-width is increased and the spacing between Pt heater lines is reduced, compared to the nanocalorimeter geometry (12 μm heater line-width and 68 μm between heater lines). The geometry is shown in Figure 3.8. The double Pt spiral has a heater line-width = 40 μm and a heater line spacing = 20 μm. A device was fabricated with a 30 nm Si-N membrane and 20 nm thick Pt heater giving a room temperature resistance $R \approx 6\ k\Omega$. The temperature distribution of a 30 nm thick Au layer on the back of this device was measured experimentally by thermoreflectance microscopy.

Figure 3.8 shows the temperature contours of the improved design simulated in air with 15.5 mW of power dissipated in the heater, providing a ΔT of about 100 K. The new heater design results in only one maximum located at the center of the sample area instead of the previous 2 maximums observed on the nanocalorimeter. By reducing the Pt heater line spacings from the 68 μm of the original nanocalorimeter to 20 μm, the isothermal area is increased by a factor of more than 4 from the nanocalorimeter, resulting in an area that fits a disk of diameter 240 μm.

In this optimized design, the Pt heater covers the entire sample area therefore the average sample area temperature is relatively well measured by the heater. $\Delta T_{av,h}$ is found to be 102 K which differs from the 1% isothermal central area temperature (between 108 and 107 K) by only 5%, thus allowing use of the direct experimental

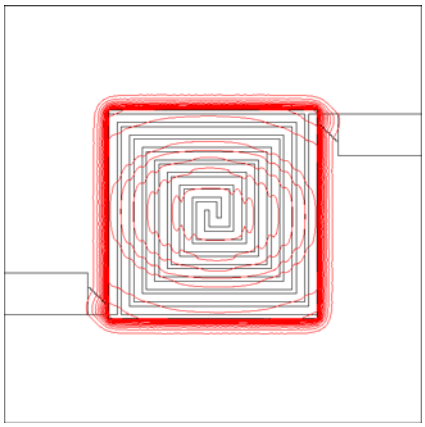

Figure 3.8: Improved design with simulated isothermal contours for ΔT = 108 K in air. The first five 1% isothermal contours are shown, which cover much of the sample area, and 5% contours are shown after that. The parameters used in the simulation are as follows: T_0 = 295 K, $k_{2D}^{Si-N} = 8.604 \times 10^{-8}$ W/K, $k_{2D}^{Pt} = 2.330 \times 10^{-7}$ W/K and $k_{2D}^{Au} = 7.1348 \times 10^{-6}$ W/K, P_{2D} = 2.33 W/cm^2, ϵ^{Au} = 0.06 and ϵ^{Pt} = 0.12, h=0.0137 W·K^{-1}·cm^{-2}, ΔT = 108 K. The double Pt spiral has a heater line-width = 40 μm and a heater line spacing = 20 μm.

measurement of the heater resistance. If the thickness of the Au layer is doubled to 60 nm, $\Delta T_{av,h}$ is only 2% below the 1% isothermal central area temperature.

Figure 3.9 (a) shows the experimental thermal map of the improved design measured by thermoreflectance and Figure 3.9 (b) shows the experimental and simulated temperature profiles, plotted along the central vertical cut of the sample area, as indicated on the thermal map. The thermoreflectance measurement is calibrated for the Au layer with $|d\Re/dT| = 8.7 \times 10^{-4}$K^{-1}. This value was chosen to match the simulation to these measurements along the vertical cut shown in Figure 3.9 (a). As an example, a horizontal profile cut would require a slightly smaller $|d\Re/dT|$ within the error bar. The Pt appears cold due to a smaller $|d\Re/dT|$. The experimental vertical profile data are pixels corresponding to the Au layer (in between Pt segments). It is in good agreement with the vertical profile data simulated using our model (line). The results are in good agreement and show a much improved central thermal homogeneity compared to the nanocalorimeter (Figure 3.6 (b)). The temperature gradient along the profile cut is reduced from 28 K for the nanocalorimeter to 8 K for the new device; more importantly the temperature gradient in the central 0.5 mm is 15 K versus 2 K.

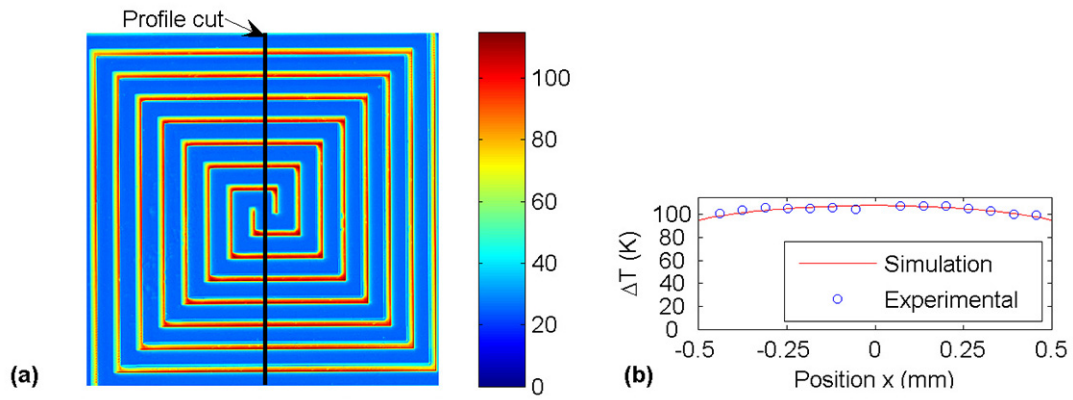

Figure 3.9: (a) Experimental thermal map of the new design measured by thermoreflectance microscopy and calibrated for Au. The device has a 30 nm Si-N membrane, a 30 nm Au thermal conduction underlayer and a 20 nm thick Pt heater. (b) Temperature profile along the central vetical cut of the sample area of the improved design shown in (a). Circles are experimental temperatures from the thermoreflectance Au thermal map and the solid line is the temperature simulated in the experimental conditions of the thermoreflectance measurement. The same parameters as in Figure 3.8 were used in the simulation.

3.5 Conclusion

By improving our previous simulation model we evaluated the applicability of our nanocalorimeter as an X-ray transparent heater stage at room temperature or above in both air and vacuum where the sample heater is used to produce a large temperature difference between the frame and the sample area.

Taking into account radiation, the nanocalorimeter with a thermal conduction layer of the same thickness as the membrane is 3-4% isothermal at room temperature in vacuum, and becomes increasingly less isothermal with either increasing T_0 or ΔT. While the isothermal criterion can easily be recovered in the small ΔT range by increasing the thickness of the thermal conduction layer, the thermal homogeneity rapidly decreases when ΔT is increased.

In the use of the device as a heater stage in air we identified convection as the dominant heat loss term which leads to a very large temperature non-uniformity with the current design. At 10 mTorr, the sample area is 10% isothermal, with 90% of the ΔT occuring across the membrane border, but by 760 Torr, the sample area is extremely non-isothermal with nearly the entire membrane remaining at T_0, even for large ΔT. Successful use of our device in non vacuum environment therefore requires re-design of the heater.

A simple double spiral design that achieves a relatively large isothermal sample area was fabricated. Thermal measurements and simulations show greatly increased

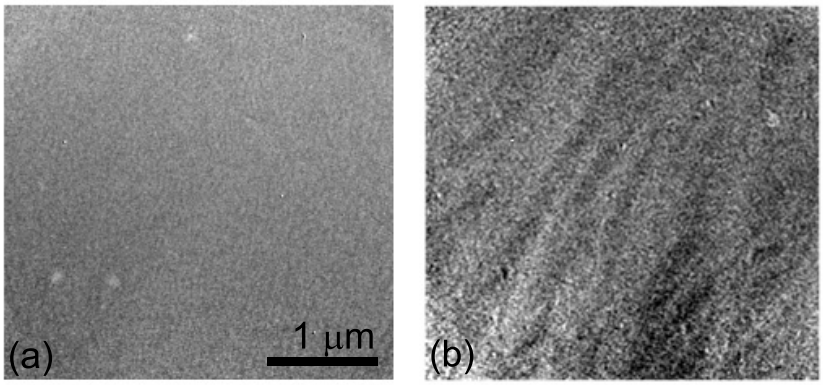

Figure 3.10: Polycrystalline Ni thin film imaged by transmission x-ray microscopy (a) heated above the Curie temperature at 400°C (no magnetic contrast) and (b) cooled below T_C at 320°C (FM domains).

homogeneous areas (up to 240 μm diameter at 1% homogeneity). This heater stage will enable x-ray transmission microscopy and spectroscopy studies with easy, fast and precise temperature control, in various environments.

The nanocalorimeter and the double spiral heater stage have been successfully used in soft X-ray transmission experiments. In a proof of principle experiment using the nanocalorimeter, the disappearance of magnetic domains in a 30 nm Ni thin film heated above its Curie temperature (358°C) was observed with a full field transmission x-ray microscope (XM-1 at the Advanced Light Source). Figure 3.10 shows the magnetic structure of the polycrystalline film imaged above T_C (400°C) and below T_C (320°C). As expected, the FM domains disappear above T_C and reappear after cooling. This experiment demonstrates that this membrane-based heater stage is capable of reaching elevated temperatures relevant to magnetic materials (e.g. Curie temperatures and metamagnetic transition temperature in FeRh) with very small power input and short amount of time. The temperature was successfully cycled several times without showing any degradation of the device.

Preliminary test transmission microscopy experiments of polycrystalline FeRh thin films were also performed using a-Si-N windows, nanocalorimeters and heater stages. These measurements were however limited to polycrystalline films. For the study of the first-order magnetic phase transition in FeRh, study of single crystalline or epitaxial films is necessary to exclude the influence of many extrinsic effects from defects seen in polycrystalline films and to obtain a sharper transition in temperature. Therefore the remainder of the work presented here will focus on FeRh films deposited on MgO single substrates (characterized in the previous section), using a non-transmission microscopy technique: photoemission electron microscopy.

Chapter 4

Temperature-driven nucleation of ferromagnetic domains

4.1 Introduction

While the first-order character of the transition in FeRh has been established from hysteresis of macroscopic measurements, the nucleation and growth of both FM (upon heating) and AF (upon cooling) domains and the coexistence of the two phases expected of a first-order transition has never been directly observed. Two previous studies were done on FeRh, both by magnetic force microscopy [18, 19] but they were limited by lack of temperature control which prevented a study of the nucleation and growth across the full transition. Moreover, these domain nucleation and growth processes are crucial to the proposed use and are affected by the surfaces and interfaces of the film. Here we report the temperature dependent imaging of FM domains in epitaxial FeRh thin films across the AF-FM transition on both heating and cooling by x-ray magnetic circular dichroism (XMCD) in photoemission electron microscopy (PEEM). We show that understanding the different stages of the transition at the microscopic level enables a consistent explanation of the macroscopic magnetization behavior. The coexistence of laterally separated AF and FM phases is observed and different stages of the phase transformation are studied: nucleation, growth and domain coalescence.

4.2 Thin film growth and characterization

90 nm thick (001) FeRh thin films were grown by magnetron sputtering from an FeRh alloy target onto (001) MgO substrates following the standard growth method presented in Chapter 2: substrate temperature of 873 K, DC power of 40 W and argon pressure of 2 mTorr. The growth rate measured by a quartz crystal microbalance was 0.04 nm/s. One of the films was capped with 2.5 nm of sputtered Al, the other

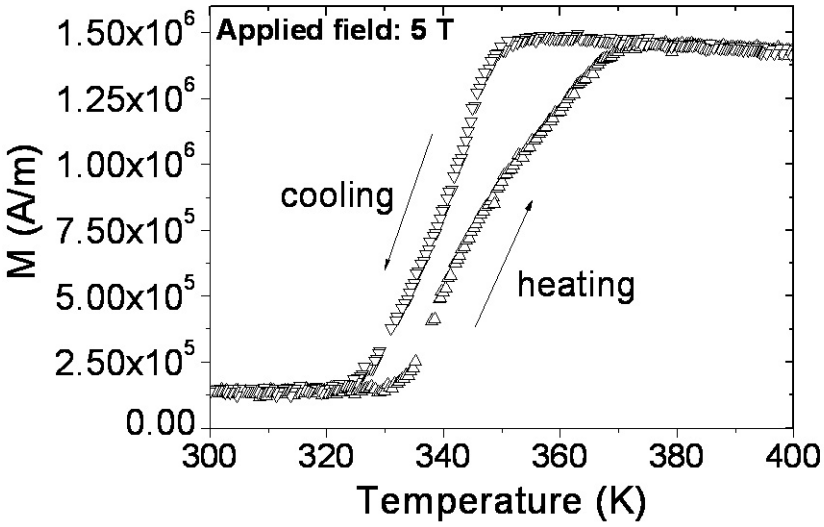

Figure 4.1: Magnetization hysteresis loops of the uncapped FeRh thin film as a function of temperature.

was left uncapped. X-ray absorption spectroscopy showed no oxidation of Fe in the capped thin film and very minimal oxidation in the uncapped thin film. We have also verified by x-ray photoelectron spectroscopy that the Al is not fully oxidized, leading to the conclusion that the interface of the capped film is metallic Al against FeRh. The thickness of the oxide formed in the uncapped film was later estimated from hard x-ray photoemission spectroscopy to be less than 2 nm.

The CsCl structure and epitaxy of the thin film was verified by x-ray diffraction. $\theta - 2\theta$ geometry scans showed (001) orientation out-of-plane and a ϕ scan on the 101 peak showed four-fold symmetry. The mosaic spread was measured to be 0.33 indicating good structural order. The in-plane and out-of-plane lattice parameters were measured to be a = 0.2988 nm and c = 0.2986 nm respectively, showing a very good agreement with the lattice parameter of bulk FeRh (0.299 nm) with negligible tetragonal distortion.

The magnetic phase transition of both the capped and uncapped samples was verified by SQUID magnetometry. Figure 4.1 shows the temperature dependence of the magnetization of the uncapped sample in an applied field of 5 T. The capped sample magnetization data was very similar, with the saturation magnetization being 10% higher. The middle of the transition occurs at 340 K in 5 T, with a small hysteresis of 4 K between heating and cooling. The transition temperature of the first-order phase transition between AF and FM shifts with field according to dT/dH = - 8 K/T. By correcting for the temperature shift due to the field the transition is expected to occur at 380 K in the absence of applied magnetic field.

4.3 Microscopy results

PEEM imaging of both samples was performed at BESSY II beamline UE49-PGM-a-SPEEM at the Fe L_3 edge (705.6 eV), using low-energy secondary electrons with a probing depth of ∼5 nm (larger than the thickness of the cap and the oxide layer) [65] and a spatial resolution of ∼30 nm. The magnetic contrast that allows imaging of FM domains is obtained by using XMCD at the Fe L_3 edge [66]. PEEM images were recorded with left-circularly-polarized (LCP) and right-circularly-polarized (RCP) x-rays. In the following images the magnetic contrast is displayed as the difference of two PEEM images taken with opposite helicities divided by their sum, to yield the XMCD asymmetry. This XMCD asymmetry is finally proportional to the projection of the Fe magnetic moment on the incident direction of the x-ray beam [67] and is computed pixel-by-pixel. To improve the signal-to-noise ratio, each PEEM image is constructed by averaging 120 single snapshots, with each acquired over an exposure time of 3 seconds. A blue-white-red colorscale was chosen in XMCD-PEEM images so as to show areas with zero asymmetry as white. The sample temperature was ramped up continuously from room temperature to 415 K and back, so as to record the complete transition upon heating and cooling. The temperature increased by about 5 K during the recording time of each PEEM image; the average temperature during the measurement is presented. Changes in magnetic contrast can generally be attributed to 3 individual factors: the magnitude of the Fe moments, the direction of the Fe moments, and the fraction of Fe atoms within the probing depth of ca. 5 nm that carry a FM moment. No external magnetic field was applied during the measurement.

Figure 4.2 shows representative images of both films near RT (AF state) and above 400 K (FM state) taken at the Fe L_3 edge. While the high temperature image in each film (Fig. 4.2 (b) and (d)) shows a similar complex pattern of micron size FM domains with strong asymmetry ranging from -0.15 to 0.15 (the same order of magnitude as asymmetry of pure Fe at the Fe L_3 edge), a striking difference can be observed between the two room-temperature images shown in Fig. 4.2 (a) and (c). The uncapped sample shows no magnetic contrast, whereas the capped sample clearly shows FM domains, albeit with reduced contrast compared to the fully FM images. Since the oxide layer of the uncapped sample is thinner than the probing depth, the vanishing magnetic contrast of the uncapped sample is attributed to FeRh in the AF phase, while the domains of the capped sample reveal a stable FM phase at the interface with the Al capping layer.

In fact, interfacial FM at RT has been previously observed by total electron yield XMCD in FeRh thin films capped with MgO and Au by Ding *et al.* [20]. In a subsequent study Fan *et al.* [21] used polarized neutron reflectometry to model the magnetic depth profile of FeRh (in a magnetic field applied in the plane of the film) capped with MgO at RT and confirmed the presence of interfacial FM near the top interface, but with a highly reduced signal compared to that of a fully FM film at

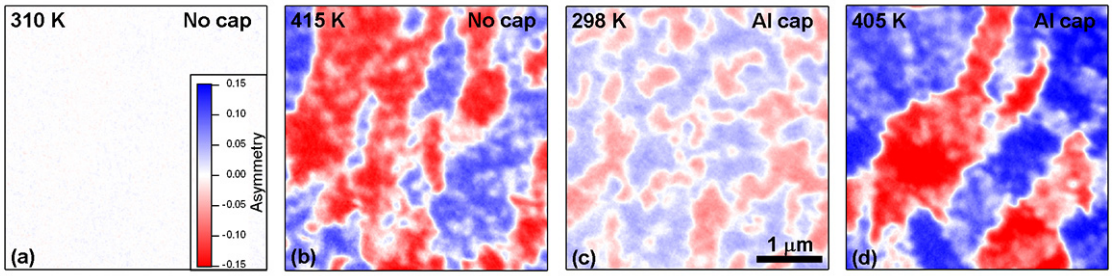

Figure 4.2: Effect of capping layer and temperature on FM domains in FeRh thin film. XMCD-PEEM asymmetry images (difference between right and left polarization images divided by their sum, in zero applied magnetic field) of FeRh thin films showing FM domains in the AF and FM states (temperature of image shown in upper left corner) for the film without capping layer (No cap (a) and (b)) and the film capped with 2.5 nm of Al (Al cap (c) and (d)). FM domains with a positive (negative) projection of the magnetization onto the x-ray beam direction are shown in different intensities of blue (red). The asymmetry colorscale used for the 4 images is shown in a.

400 K. The stabilization of the FM phase at the interface is assumed to result from a combination of Fe deficiency and strain effects due to the cap. The thin native oxide does not have a similar effect or it is so weak as to be undetectable. These effects will be further investigated in Chapter 6.

Our observation is in good agreement with these prior results. We attribute the reduced magnetic contrast in Fig. 4.2 (c) relative to (d) to a possible combination of reduced atomic Fe moments and a thin FM layer compared to the probing depth of ca. 5 nm. An alternative explanation for the reduced contrast is canting of the moments out of the plane; however, this is unlikely as it would result in some regions with increased magnetic contrast which we do not observe.

Since the presence of the Al cap generates FM domains near the interface even at RT we turn to the uncapped sample to study the transition from the fully AF to the fully FM state. The spatial resolution of the PEEM technique allows us to look at the evolution of the FM domains as a function of temperature without an external magnetic field, as shown in Fig. 4.3 ((a) (e) heating and (f) (j) cooling).

In an effort to relate the transition at the microscopic level to the macroscopic behavior, we calculated the integrated absolute XMCD (|XMCD|) for a circular region of interest at the center of the field of view, shown as an inset in Fig. 4.3 (k). Figure 4.3 (k) compares the evolution of |XMCD| as a function of the sample temperature to the temperature evolution of the macroscopic magnetization. The magnetization was recorded by SQUID magnetometry in an applied field of 5 T (Fig. 4.1) and was then corrected by an 8K/T shift determined experimentally so as to extrapolate the M-T transition to zero field. The magnetization recorded by magnetometry in 5 T is a

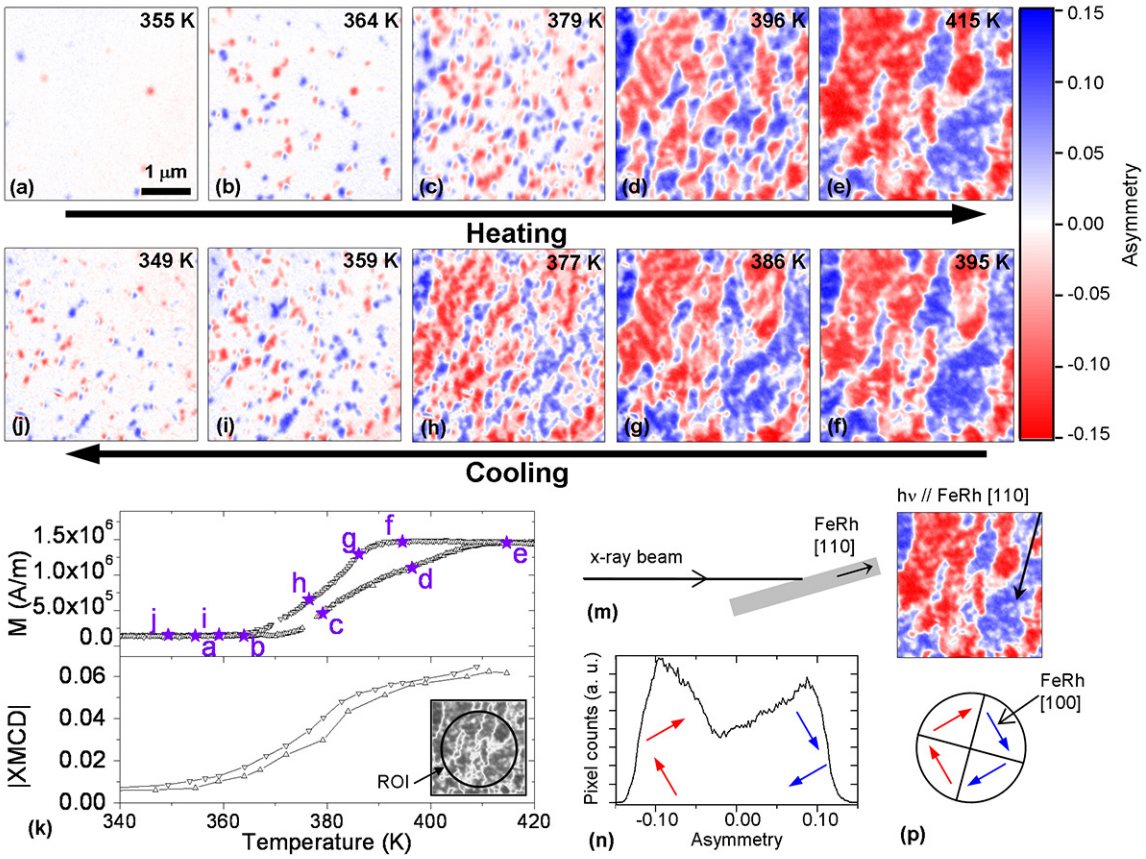

Figure 4.3: Temperature evolution of FM domains in the uncapped FeRh thin film, temperature hysteresis and FM domain configuration. (a) to (e) shows heating from AF to FM and (f) to (j) shows cooling from FM to AF, in zero field. The asymmetry (difference between right and left polarization images divided by their sum) colorscale used for these images is from -0.15 to 0.15. Normalized M-T hysteresis measured at 5 T is shown in the upper panel of k; the temperature axis has been corrected to zero field. Integrated absolute XMCD of a representative region of interest (ROI - shown in inset) as a function of temperature is shown in the lower panel of (k). The sample configuration with respect to the x-ray beam and direction of the projection of the beam in the images is shown in (m). The distribution of asymmetry in (e) (415 K) is shown as a histogram in (n). The two maxima are assigned to two pairs of equivalent FeRh <100> in-plane directions as preferred orientation of FM domains (easy axis). The four <100> directions are sketched in (p).

close approximation to the fraction of FM phase. The |XMCD| measurement includes domains and therefore is not as good a representation of the fraction of FM phase but still shows a similar hysteretic behavior to the M-T curve. In particular the middle of the transition agrees on both curves around 380 K. Since magnetization is the better representation of the fraction of FM phase we relate each PEEM image to its position on the M-T hysteresis curve using letter labels in Fig. 4.3 (k).

Figures 4.3 (a) (e) thus show the nucleation and growth of FM domains and confirm the first-order character of this magnetic transition. At RT the uncapped film has vanishing magnetic contrast (due to a fully AF surface). Upon heating, we observe the appearance of small spots of magnetic contrast, attributed to the nucleation of small FM islands in an AF background. The nucleation of FM islands out of the AF matrix starts near 355 K (Fig. 4.3 (a)). Over a broad temperature range (about 30 K) we observe the coexistence of FM and AF areas. FM islands continue to nucleate in different areas of the sample, as seen at 364 K and 379 K (Fig. 4.3 (b), (c)). Above 380 K, where a change of slope is observed on the magnetization curve (Fig. 4.3 (k)), the phase transformation switches into a domain-growth regime. The number of domains stops increasing but their size starts to significantly increase. This continues over a range of 30 K (from 380 K to 410 K). In the middle of the growth regime, at 396 K, the domains can be observed to have more than doubled in size (Fig. 4.3 (d)). At 415 K, the image shows a fully FM phase (Fig. 4.3 (e)) with a complex pattern of domains similar to the results of magnetic force microscopy by other groups [18, 19]. Two stages of the phase transformation were observed, one dominated by domain nucleation at low temperature and one dominated by domain growth at high temperature, as supported by classical nucleation theory, and further confirming the first-order character of the transition.

The in-plane projection of the x-ray beam is along the [110] direction of the FeRh film, as shown in Fig. 4.3 (m), where the beam direction is indicated in the PEEM image taken at 415 K. As noted above, XMCD-PEEM is sensitive to the component of magnetization parallel to the beam. Magnetization directions with the same projection have the same contrast. The histogram of asymmetry distribution shown in Fig. 4.3 (n) exhibits two maxima. Because of the in-plane cubic symmetry of the FeRh film, magnetocrystalline anisotropy should result in four equivalent preferred directions, at 90° angles from each other. The <100> directions are at 45° from the beam direction and therefore their projections are equivalent two by two, as shown on Fig. 4.3 (p). This is compatible with the two maxima of the histogram. If domains were <110> type, there would be a maximum at zero asymmetry, and if the film had no anisotropy there would be no peak in the histogram. Therefore the FM domain structure consists of four types of in-plane domains along <100> easy axes separated by 90° domain walls.

Upon cooling, the reverse transition from FM to AF is observed. At 395 K the sample is still fully FM, in agreement with the M-T hysteresis. From 395 K to 377 K, the FM domains decrease in size (Fig. 4.3 (f) to (h)) but continue to occupy the

full field of view. From 377 K to 359 K, the fraction of AF phase (white regions) increases, indicating the nucleation and growth of the AF phase. At 359 K (Fig. 4.3 (i)) the coexistence of the two magnetic phases is again clearly seen and the hysteretic behavior of the transition is evidenced by the larger number of FM nuclei compared to the PEEM image taken at 364 K upon heating (Fig. 4.3 (b)). Finally a small fraction of the thin film is still FM at 349 K as seen on Fig. 4.3 (j) but is gone completely by 310 K (Fig. 4.2 (a)).

Comparison of the beginning of the AF to FM transition at 364 K upon heating (Fig. 4.3 (b)) to the end of the FM to AF transition at 349 K upon cooling (Fig. 4.3 (j)) shows that the majority of the nucleation sites identified upon heating are conserved upon cooling, evidence of heterogeneous nucleation as inferred from macroscopic magnetization measurements by Maat *et al.* [7]. The transition at the surface of the film seen in PEEM thus follows very closely the temperature hysteresis of the entire film as measured by magnetometry upon heating and cooling.

4.4 Discussion

We now turn to the details of the nucleation of the FM phase upon heating. In the early stage of this nucleation, we observe single domain FM nuclei with a diameter as small as 100 nm. Four different representative single domain nuclei are indicated in the inset in Fig. 4.4 (a). The nuclei were chosen to show the extent of the nucleation phase over a wide temperature range.

In the XMCD-PEEM image taken at 372 K all four nuclei are present but they actually nucleated at different temperatures as shown by plotting the absolute asymmetry of the center of each nucleus (6 by 6 pixels, 60 nm wide) as a function of temperature in Fig. 4.4 (a). The temperature spread is attributed to different heterogeneous nucleation sites. The activation energy ΔG_b for heterogeneous nucleation at a defect (e.g. grain boundary) can be written as $\Delta G_b = f\Delta G_H$, with f a shape factor dependent on the nature of the defect, and ΔG_H the activation energy for homogeneous nucleation. Different types of defects, for example low-angle grain boundaries with varying angles, result in a range of shape factors, therefore a range of activation energies and ultimately a range of nucleation temperatures.

The four different nucleation sites indicated in Fig. 4.4 show that the nucleation temperature range extends over 25 K, in good agreement with the observation of the nucleation phase from 355 K to 380 K in Fig. 4.3. When the probing area is the size of a single nucleus, the transition between the two distinct phases is observed to be quite abrupt. The width of the local transition is less than 10 K, as indicated by a rapid increase of asymmetry from 0 to 0.10 within 10 K or less. Note, however, that the temperature was ramped continuously during the recording time of each PEEM image; this temperature ramp results in a 5 K temperature increase during the recording of each data point on Fig. 4.4 (a), which becomes convoluted into the

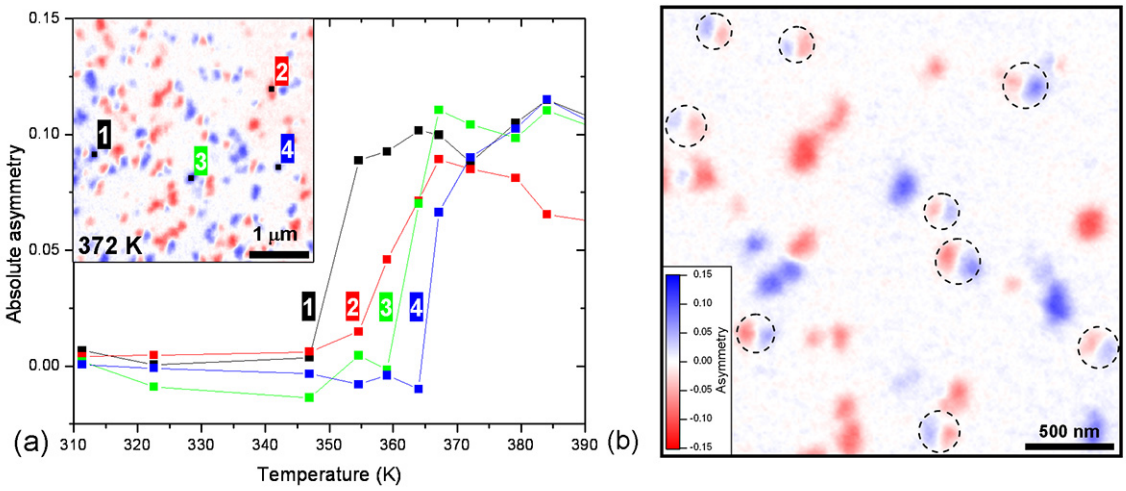

Figure 4.4: (a) Temperature evolution of absolute asymmetry of 4 different local areas (6 pixels by 6 pixels) showing the sharp local increase in magnetic contrast at the single domain nucleus scale and the spread of the nucleation regime over about 25 K. The location of the nuclei is indicated in the inset (XMCD-PEEM asymmetry image at 372 K). While islands initially nucleate as single domains, they then break into several domains upon increasing size. (b) is an enlargement of the XMCD-PEEM image from Fig. 3(b) taken at 364 K showing FM nuclei in AF matrix in an uncapped FeRh thin film. Several nuclei with diameter of 200 nm or above are indicated by dotted circles and show multidomain flux closure patterns as seen by red and blue lobes.

local transition temperature spread. The local transition may therefore be as sharp as 5 K. By contrast the overall width of the transition seen in Fig. 4.3 (k) results from an average over the entire sample, thereby broadening the transition to the 25 K of the nucleation phase, as well as additional broadening of about 30 K from the growth phase.

Figure 4.4 (b) is an enlargement of an area of the PEEM image taken at 364 K (shown in Fig. 4.3 (b)). While initially the FM nuclei form single domains many of the freshly nucleated FM islands later minimize their magnetostatic energy by formation of flux closure patterns, seen as red and blue lobes in Fig. 4.4 (b). These flux closure patterns can be four-domain patterns (¡100¿ type, as shown in Fig. 3(p)) or vortex patterns with a continuously flowing magnetization and no domain walls if domain wall creation is not energetically favored in these small nuclei. Both would appear the same in these images.

The drastic change in domains between 379 K and 396 K upon heating (Fig. 4.3 (c), (d)) shows the transition from FM domain nucleation to domain growth. Fig-

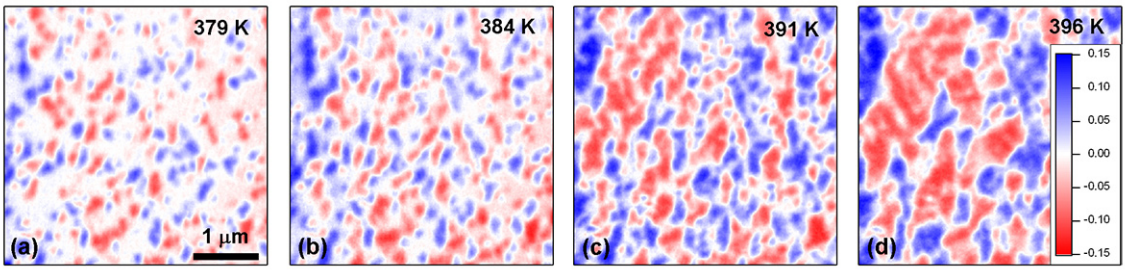

Figure 4.5: XMCD-PEEM asymmetry images showing the transition from nucleation regime to growth regime in FeRh thin film between 379 K (same as Fig. 4.3 (c)) and 396 K (same as Fig. 4.3 (d)). The coalescence of FM domains is seen between (b) 384 K and (c) 391 K.

ure 4.5 shows this transition in more detail; the magnetic domain morphology changes from numerous small domains to a smaller number of larger domains. By looking at intermediate steps we see the phenomenon of coalescence. While at 379 K many FM islands form flux closure patterns, between 384 K (Fig. 4.5 (b)) and 391 K (Fig. 4.5 (c)) the percolation limit is reached so that the exchange interaction energy favors the formation of larger domains, i.e. small islands start to overlap and coalesce into larger FM areas. The small second increase in the slope of the M-T curve (Fig. 4.3 (k)) around 388 K is attributed to the start of the coalescence between 384 K and 391 K.

Finally we turn to the evolution of local nucleation sites upon the FM to AF cooling transition. The magnetic contrast of the same 4 nuclei presented in Fig. 4.4 is studied upon cooling, over the temperature range 359 K to 341 K, taking into account the temperature hysteresis of the transition of $\sim$13 K.

Figure 4.6 shows in the upper panels the images recorded upon heating, with the 4 nuclei labeled 1 to 4, and in the lower panels, the images recorded upon cooling, with the corresponding heating and cooling temperatures shifted by the hysteresis of 13 K. A strong correspondence in the FM domain pattern is seen between the heating image at 372 K and the cooling image at 359 K. While the nucleation of the FM nuclei is spread out from 359 K to 372 K upon heating, the disappearance of the same FM regions upon cooling follows a different behavior. All 4 FM regions reduce in size but persist until 349 K, followed then by complete disappearance of the magnetic contrast between 349 K and 341 K. Note that no image was recorded at an intermediate temperature between 349 and 341 K. Nevertheless, this shows that there is an asymmetry in the evolution of the FM phase between heating and cooling, even at the local level. This observation is in agreement with the asymmetry between the heating and the cooling transition seen in the M-T measurement.

To further understand the difference between heating and cooling, we turn to

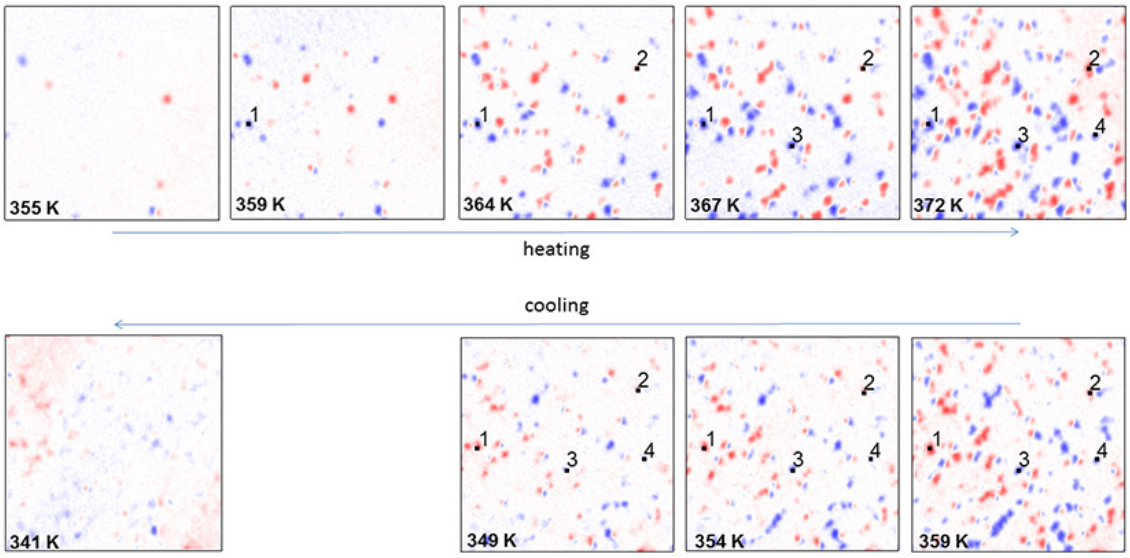

Figure 4.6: Temperature evolution of 4 local regions (labeled 1 to 4) upon heating from 355 K to 372 K (upper panels - same as Fig. 4.4 (a)) and upon cooling from 359 K to 341 K (lower panels). Images aligned vertically correspond to a temperature hysteresis of ∼13 K. No image was recorded around 345 K upon cooling so the panel is left intentionally blank.

the local evolution of the asymmetry. Figure. 4.7 shows the evolution of the absolute asymmetry of the center of the selected 4 different nuclei as a function of temperature during a full transition from AF to FM and back to AF. The sharp heating curves from Fig. 4.4 (a) are reproduced and the cooling curves of each nucleus are overlaid so as to allow comparison between the heating and the cooling transition. This analysis offers a mixed picture of the transition. On one hand, the reverse order of nucleation is observed upon cooling with nucleus ♯4 disappearing first and nucleus ♯1 disappearing last, confirming a heterogeneous effect in the nucleation where non-random regions are first to be FM upon heating and last to be AF upon cooling. On the other hand, while the four regions have distinct well-defined transition temperatures upon heating with a width of 5 to 10 K, the cooling transition is spread over a broader temperature range of 16 to 27 K and regions ♯2 to ♯4 transition over practically the same temperature range of 364 K to 341 K. The loss of magnetic contrast in the selected regions upon cooling is due to the growth of the AF phase. Note that since the size of each local region is fixed to 6 by 6 pixels (60 nm wide) and the asymmetry is averaged over this area, the progressive decrease in asymmetry is due to the AF phase growing into the region. The difference in behavior observed between heating and cooling is therefore attributed to the difference between the heterogeneous nucleation of the FM phase

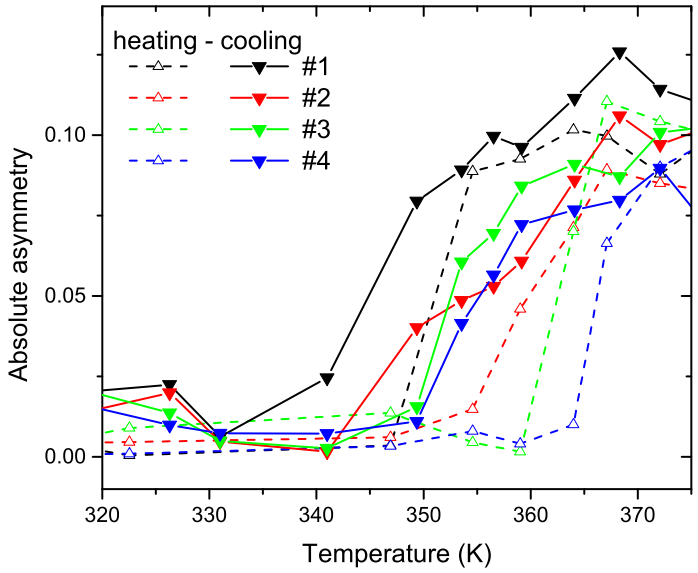

Figure 4.7: Temperature evolution of absolute asymmetry of the 4 different local areas labeled in Fig. 4.4 and Fig. 4.6 showing the difference in magnetic contrast evolution between heating and cooling.

and the growth of the AF phase.

4.5 Conclusion

In summary, FM domains were imaged near the surface of high-quality FeRh thin films. The sample capped with Al showed interfacial (FeRh/Al interface) FM domains which are stable at room temperature, while the bulk of the film is AF. An identical film with no cap has no observable surface FM domains at room temperature and is shown to follow the expected transition as measured by magnetometry. Nucleation, growth and coalescence stages were identified in the phase transformation mechanism from AF to FM. The coexistence of FM and AF phases inherent to a first-order phase transition was observed in the early stages of the transition and small FM nuclei were seen to form flux closure patterns. A locally sharp nucleation of the FM phase upon heating was observed, in contrast to a broad growth of the AF phase upon cooling, confirming the asymmetry between the heating and cooling transition. This study of the transition at the microscopic level has thus led to a better understanding of the true dynamics and the breadth of the macroscopically observed transition.

Chapter 5

Temperature-driven evolution of the antiferromagnetic phase

5.1 Introduction

In Chapter 4 we showed that the evolution of the FM phase followed the expected transition as measured by magnetometry but that the different stages of nucleation, growth and coalescence could be identified as well as other local details of the transition using the microscopic probe. While XMCD at the Fe L_3 edge was used to image FM domains, a vanishing magnetic contrast was attributed to the AF phase of FeRh. XMCD is sensitive to the average magnetization $< M >$ and is therefore not sensitive to AF order which has no net magnetization. For this reason, details of the AF phase domain structure could not be obtained in this previous study.

Originally thought as lacking technological interest due to the non-existence of a net moment, AF materials have in fact turned out to be extremely important for memory technology. In particular, there has been significant interest in AF thin films due to the exchange bias phenomenon [68] and several studies have been successful at studying the microscopic structure of AF thin films in exchange-biased systems, in particular AF domains, using x-ray magnetic linear dichroism (XMLD). In its proposed use for heat-assisted magnetic recording (HAMR), FeRh is AF at the magnetic storage temperature ; therefore, information about the structure of the AF phase is useful for its technological application. Analogous to FM domains, AF domains are defined as regions in a crystal in which the pattern of magnetic moments is periodic in all three directions of space. Although the domains have no net magnetization, each antiparallel sublattice carries a magnetization M and XMLD is sensitive to $< M^2 >$ and can probe identically ferromagnets and antiferromagnets.

The AF structure of FeRh has been studied by neutron diffraction and is known as G-type [43, 69, 70]: the Fe site moments have FM coupling in (111) planes and AF coupling between the planes. The crystallographic direction of the moments

themselves has not been reported. In the classic antiferromagnet NiO, which has a G-type AF structure like FeRh, the domain walls that separate different AF domains can be due to either a change in crystallographic orientation of the FM planes (T domains for twinning) or a rotation of the direction of the moments within the FM planes (S domains for spin-rotation) [71]. The twin walls are obviously directly related to crystallographic defects but it was seen that the second type of walls are also stabilized by imperfections in the crystal. Therefore AF domains in epitaxial FeRh thin films are likely to correlate to the defects present in the thin film such as anti-phase boundaries, dislocations and low-angle grain boundaries.

Most of the XMLD spectroscopy and microscopy studies of AF have been limited to oxide compounds such as NiO, Fe_2O_3 and $LaFeO_3$ [72, 73, 74]. The typical challenge with using XMLD is that it probes the anisotropy of the electronic structure that is induced by axial spin alignment from the magnetic order (FM or AF). This usually results in changes in the fine structure of the x-ray spectrum which require a good energy resolution to be distinguished. Moreover, while for oxides the XMLD can be as large as 40 % of the absorption signal, the reduced crystal-field splitting of electronic states in metals is thought to reduce this effect for metallic systems [75]. Nevertheless, several studies have reported successful experimental XMLD on magnetic transition metals (Fe, Co and Ni) in their metallic state, as a way to probe the magnetocrystalline anisotropy, with maximum relative difference in absorption between the two linear polarizations ranging from 6 to 11 % for Fe [76, 77, 78]. Several studies have also reported on the XMLD microscopy of metallic FM domains [79, 80] but few studies have attempted at direct imaging of AF domains in a metallic sample. One reason is that metallic simple AF are not common: the well-known AF (Cr, FeMn) have spin-wave or non-collinear structures which do not generate any XMLD signal, since the projection of the AF sublattice onto the x-ray direction is zero.

Equiatomic FeRh is a simple AF but it poses an additional challenge in that it undergoes a first-order AF to FM transition near 350 K and the two phases coexist over a temperature range of 20 to 30 K across the transition. The spatial resolution of both AF and FM domains ideally would be addressed by the use of two effects exclusively sensitive to each magnetic order. XMCD has been successfully used to resolve FM domains in FeRh, without any sensitivity to the AF phase but as mentioned earlier, XMLD is sensitive to both AF and FM order.

In this work, we use both XMCD and XMLD in photoemission electron microscopy (PEEM) combined with image processing techniques to study the characteristics of the AF phase and its evolution with temperature upon cooling across the FM to AF transition in an epitaxial FeRh thin film. The goal of this work is double: to determine the domain structure of the stable AF phase and to study its evolution through the transition in comparison to the evolution of the FM phase, so as to obtain a complete picture of the nucleation and growth mechanisms involved in both sides of this unusual transition.

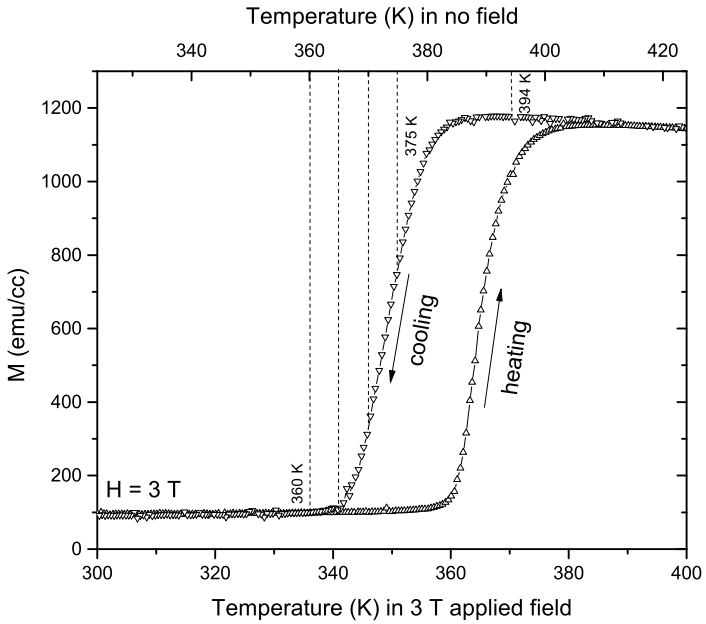

Figure 5.1: Magnetic characterization of the FeRh thin film. The magnetization as a function of temperature was measured in 3 T (bottom axis). The vertical dashed lines show the temperature at which the PEEM images were recorded upon cooling in no external field (top axis): 394 K (fully FM), 375 K, 370 K, 365 K (mixed FM and AF) and 360 K (fully AF).

5.2 Experimental techniques

100 nm thick (001) FeRh thin film was grown by magnetron sputtering from an FeRh alloy target onto (001) MgO substrates, following the standard growth method presented in Chapter 2. Details of the sample synthesis can also be found in Ref. [24]. The film was left uncapped since several capping materials have shown to modify the magnetic properties near the top interface, which will be the focus of Chapter 6. To limit the formation of the native oxide layer seen in Chapter 4, the sample was fabricated in our laboratory and then introduced in the PEEM microscope chamber on the same day. X-ray absorption spectroscopy (XAS) was recorded in the PEEM microscope chamber at room temperature before imaging and showed no significant oxidation of Fe.

The magnetic phase transition was verified by SQUID magnetometry. Figure 5.1 shows the temperature dependence of the magnetization of the uncapped sample in an applied field of 3 T (a large field is used to shift the transition below 400 K, the maximum temperature of the SQUID magnetometer). The middle of the transition upon cooling occurs at 349.5 K in 3 T, with a width of 25 K between the beginning

and the end of the transition (bottom axis). By correcting for the temperature shift due to the field (dT/dH = - 8 K/T) the transition from FM to AF is expected to occur between 388 K and 363 K in the absence of applied magnetic field (top axis). Therefore we limit our imaging as a function of temperature between 394 K (no AF phase) and 360 K (fully AF according to magnetometry), with additional imaging in the fully AF phase at 300 K for confirmation.

PEEM imaging was performed at ALS PEEM Beamline 11.0.1 at the Fe edge, using low-energy secondary electrons with a spatial resolution of 30 nm. Magnetic contrast is obtained by using either left and right circularly or parallel p and perpendicular s linearly polarized x-rays in XMCD and XMLD respectively. XMCD images were recorded at 707.8 eV. The XMCD energy was determined from the position of the Fe L_3 peak in the Fe XAS spectrum (differences with theoretical Fe L_3 of 706.8 eV are in part due to beamline calibration offset). XMLD images were recorded at two different energies. These energies were selected by recording PEEM images at 10 different energies around the Fe L_3 peak to determine the maximum XMLD signal. The signal was optimized when comparing two energies respectively 0.1 and 1 eV below the L_3 peak.

Figure 5.2 shows spectra recorded on FeRh at room temperature (AF phase) with parallel p and perpendicular s linear polarizations. Two different features in the XLD $s - p$ signal are seen: a positive maximum at the L_3 peak and a negative minimum about 1 eV below, with a maximum $s - p$ signal as high as 9 % relative to the XAS intensity, very similar to the XMLD spectra reported for FM Fe [76, 77, 78, 81]. The data was treated following the standard x-ray dichroism method: direct beam intensity was subtracted and the jump in XAS before and after the Fe L_3 edge was normalized to 1. Smoothing was applied to remove instrumental noise.

Two distinct features can be observed in XLD shown in Fig. 5.2. The main feature (dipolar shape near 710 eV) is seen on three samples grown on different substrates (MgO, c-plane sapphire and ion-beam-assist-deposited (IBAD) MgO). Since these samples were prepared on different substrates, their crystallographic orientation differ: films grown on MgO and IBAD MgO have [001] out-of-plane orientation while deposition on c-plane sapphire induces [111] orientation. In addition, MgO and IBAD MgO have been shown to induce different strain state in FeRh, with a significant tetragonal distortion in the films grown on IBAD MgO and a mostly cubic film on MgO. Specifically, x-ray diffractometry shows that films deposited on MgO are unstrained within the 0.3 % accuracy of the measurement. The same dipolar shape of the dichroic signal at room temperature in all three films is a strong indication that at least part of the signal is independent from structural distortion of the AF phase and therefore is magnetic in origin. A secondary peak (also near 710 eV) is observed with a different intensity for the different samples. This secondary feature could be structural in origin.

Another possible cause of a room temperature linear dichroism is a parasitic moment, e.g. AF moments which are not completely collinear and result in some net

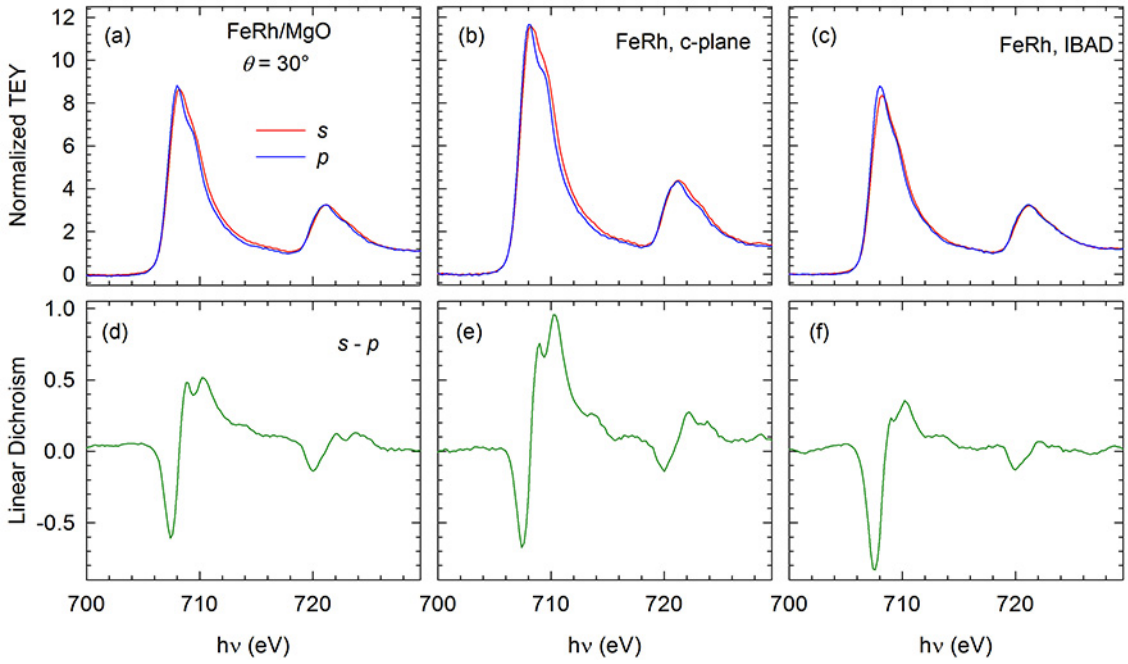

Figure 5.2: XLD spectrum recorded at room temperature (AF phase) in total electron yield mode on an FeRh film capped with MgO deposited on (a) MgO substrate, (b) c-plane sapphire substrate, and (c) IBAD MgO. The upper panels show the two spectra recorded with s and p polarizations and the lower panels show the difference $s - p$ and the presence of a maximum and a minimum near the Fe L_3 edge.

uncompensated moment. No interface canting effects are known in FeRh and such effects seem unlikely based on the low anisotropy of this system in both AF and FM phases in the absence of tetragonal distortion, which is the case of the film deposited on MgO [37].

Four different image configurations were recorded: two different energies (E_1=706.7 eV, E_2=707.7 eV) and two different polarizations (parallel p and perpendicular s). Note that 0.1 eV is at the limit of the energy resolution of the beamline, therefore a small energy drift can easily affect the quality of the XMLD images. In particular, there is some energy dispersion in the vertical direction of the x-ray beam which means that the XMLD magnetic contrast is optimized only over a horizontal portion of the image, since the features are very close in energy. The angle between the incident x-ray beam and the sample is fixed at 30 degrees and in this sample/beam geometry, the p polarization corresponds to the vertical direction which is parallel to the plane of the film and the s polarization to the horizontal direction, with a projection closer to the perpendicular of the film.

We found that dividing the signal obtained for the different polarizations and then for the different energies improved the XMLD contrast (close to the limit of the

instrument of 0.2 %) and we used this operation to generate XMLD images:

$$I_{XMLD} = \frac{p(E_1)/s(E_1)}{p(E_2)/s(E_2)} \tag{5.1}$$

Note that this division is a good approximation for actual asymmetry operation. The asymmetry A is defined as

$$A = \frac{I_1 - I_2}{I_1 + I_2} \tag{5.2}$$

By subtracting two images taken with different polarizations, any non-XMLD contrast which is chemical or topographic in origin does not depend on polarization and therefore is eliminated. Using the notation $I_2 = I$ and $I_1 = \Delta I$, since the difference in intensity ΔI is small compared to the intensity I itself, we can deduce:

$$A = \frac{\Delta I}{2I + \Delta I} \approx \frac{\Delta I}{2I} \tag{5.3}$$

and compare it to the division:

$$\frac{I + \Delta I}{I} = 1 + \frac{\Delta I}{I} \approx 1 + 2A \tag{5.4}$$

and confirm that the division of two images is a close approximation of the asymmetry (save with constant coefficient and offset). To improve the signal-to-noise ratio of the images, a large number of snapshots was recorded and then averaged, typically 100 to 200 snapshots for XMLD images and 10 to 20 snapshots for XMCD images. The XMCD contrast is quite strong and does not require the same statistics to produce good quality images.

The temperature of the sample was controlled by a custom stage with a tungsten filament for heating power, a cryogenic cold source for controlled cooling power, and a silicon diode thermometer for temperature reading. The temperature of the sample was stabilized for each measurement and kept constant for the duration of recording of the several snapshots required for each image (time ranging from a few minutes to about an hour).

XMCD and XMLD PEEM images are analyzed using autocorrelation. The autocorrelation of a function is the cross-correlation between itself as defined by

$$\Phi_{f,f}(x, y) = f(x, y) * f(x, y) = \int\int f(\xi - x, \eta - y) f(x, y) d\xi d\eta \tag{5.5}$$

and is easily numerically computed using the following theorem:

$$\Phi_{f,f}(x, y) = F^{-1}[F(u, v)F^*(u, v)] \tag{5.6}$$

with $F(u, v)$ the Fourier transform of $f(x, y)$ calculated in MATLAB by Fast Fourier Transform (FFT). The origin of the autocorrelation image $\Phi_{f,f}(0, 0)$, located at the

center of the image, is a global maximum of the autocorrelation function. For the images analyzed here, the amplitude of the autocorrelation function then decreases sharply with increasing x and y. The autocorrelation images are found to be mostly radially symmetric (the only exception is the XMCD image of the fully FM phase), indicating that the average size of the features is isotropic with x and y, therefore a radial average of the autocorrelation is calculated and plotted as a function of radial pixel. The radial profile is fitted with a Gaussian $a\exp(-(x/b)^2)$ distribution or a combination of Gaussian distributions. The number of Gaussians used depends on the nature of the autocorrelation and will be discussed in more details in Section 5.4. The correlation length of the image is defined as twice the Gaussian fit parameter b. This standard autocorrelation method is used for example to analyze chemical heterogeneity in scanning transmission microscope images, grain size distributions in geology and fluorophore distributions in biology [82, 83, 84]. Note that the correlation length referred to in this work is the characteristic length of the image and is not the spin-correlation length related to the magnetic order.

A similar method can also be applied to determine if two different images (e.g. XMCD and XMLD images at the same temperature or XMLD images at different temperatures) are correlated. The cross-correlation $\Phi_{f,g}$ is computed instead and the same treatment is applied. If there is long-range correlation between f and g, the origin $\Phi_{f,g}(0,0)$ is a maximum and the cross-correlation decays exponentially from there. A maximum located at any other position in the image indicates no long-range correlation between the two images.

To extract a correlation length that is representative of the actual lengthscale of the image features, one needs to account for different contributions to the autocorrelation function. One contribution is from the point spread function of the charge-coupled device detector which results in a short range contribution with a sharp peak at $\Phi_{f,f}(0,0)$. An additional contribution from the image background can result in a long-range contribution (e.g. non-flat image background) with a broad peak. Note that all the images are processed by applying 3 passes of an order 3 polynomial flattening in the beamline image analysis software PEEMVision7.0. This operation does not correct well for intensity gradients along the diagonal of the image, therefore an additional flattening operation is performed in MATLAB. The background of the image is determined by plotting the image as a surface and fitting a 2-dimensional linear plane to this surface, and is then subtracted. While the contributions from the detector and the background can be negligible when the signal to noise ratio is large, they become apparent in low signal to noise ratio images, such as here in XMLD images.

The uneven background is due to the non-constant profile of the x-ray beam. The illumination profile changes with the polarization of the beam and gives rise to regions of increased or decreased intensity in the computed XMCD or XMLD images, in particular in the corners. This is a known artefact of the measurement technique and is not a magnetic effect.

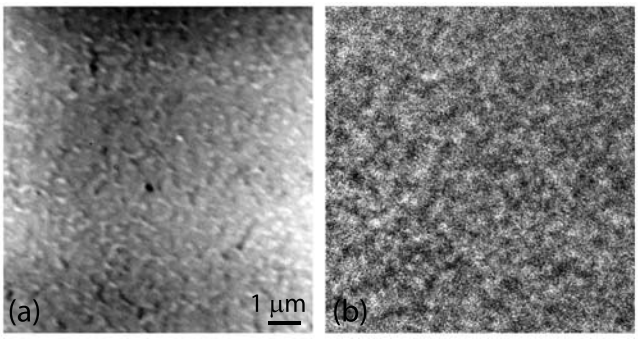

Figure 5.3: (a) Topographic PEEM image of FeRh thin-film surface recorded at Fe L_3 edge showing relatively smooth and uniform surface with small defects due to film roughness and (b) XMLD image of the same location recorded at room temperature.

The robustness and consistency of the autocorrelation is tested by computing the autocorrelation with different window sizes (ranging from 512 by 512 to 900 by 900 pixels) and error bars in correlation length are extracted from the standard deviation of the fits produced with different window size. Note that the full field of view size is 1024 by 1024 pixels.

5.3 Microscopy results

Figure 5.3 (b) shows that small features with a weak but noticeable XMLD contrast are observed at room temperature. We consider the possibility of the weak XMLD contrast coming from residual topographic features that did not get properly removed in the image computation (due to increased error in correction of the spatial drift with large acquisition times). Visual comparison to the topography of the sample in Fig. 5.3 (a) shows no clear similarity between the two, indicating that the spatial features resolved in the XMLD image are not topographic in origin and the image computation correctly removes non-XMLD features. Calculation of the cross-correlation image of the topography and XMLD image confirms that no long-range correlation is found between the two. Therefore, these XMLD contrast features are most likely AF in origin, and we now turn to their evolution with temperature across the transition, which will help us validate this assumption.

Figure 5.4 shows the XMCD (a) and XMLD (b) images recorded in the FM phase at 394 K. An XMLD pattern with strong contrast is clearly visible, due entirely to the FM phase (as previously discussed, XMLD includes contributions from both AF and FM phases). This is confirmed by comparing the XMLD image to the XMCD image and establishing spatial correlation between the two: constant intensity contours are overlaid on each dichroic image (Fig. 5.4(a) and (b)) and the two contour patterns are then compared to each other in Fig. 5.4(c). An excellent match is observed between

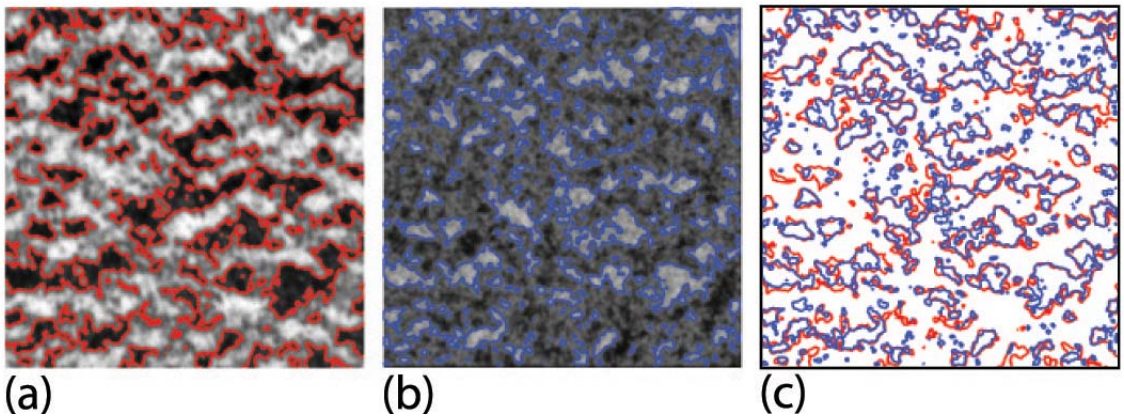

Figure 5.4: Comparison of domain pattern in XMCD-PEEM image to XMLD-PEEM features in the fully FM phase at 394 K. Contours of constant intensity are drawn to make (a) the FM domains apparent in the XMCD image and (b) the corresponding XMLD pattern in the XMLD image recorded at the same temperature. (c) Overlay of the two contour images showing the good spatial correlation between the two signals.

the two patterns. This clearly shows that a spatially resolved XMLD signal is detected from the FeRh FM phase. We further confirmed that the high temperature XMLD contrast is magnetic in origin by heating a similar sample above its Curie temperature $T_C = 573$ K [6]. Both XMCD and XMLD contrasts disappear above T_C which supports that both contrasts are due to the FM phase. Note that this temperature treatment of the sample resulted in a permanent FM surface (no magnetic transition upon cooling), likely due to chemical modification of the surface by diffusion, as will be discussed in Chapter 6. This effect means that the sample once heated this hot is no longer useful for the experiments described here, but nonetheless proves that the XMLD signal at 394 K was due to the FM phase. The FM origin of the XMLD contrast in the FM phase is also strong evidence of the magnetic origin of the XMLD contrast in the AF phase as well. Since the magnitude of the Fe moments in the FM and AF phases are similar with 3.2 and 3.1 μ_B respectively [37] and the mechanism for XMLD contrast is independent of the AF or FM order, our measurement should be capable of detecting magnetic contrast from the AF phase.

We now turn to the evolution of the XMCD and XMLD patterns with temperature. Figure 5.5 shows a summary of the XMCD images recorded at different temperature across the cooling transition from FM to AF, starting at 394 K in the fully FM phase and cooling to 360 K at an almost completed transition with only few residual FM nuclei left (Fig. 5.5(a) to (e)), and the XMLD images recorded at the same temperatures (Fig. 5.5(f) to (j)). With the XMCD images, we observe the progressive disappearance of the FM phase upon cooling: first a reduction in the size of the domains, then in the number of the FM domains, in full agreement with our

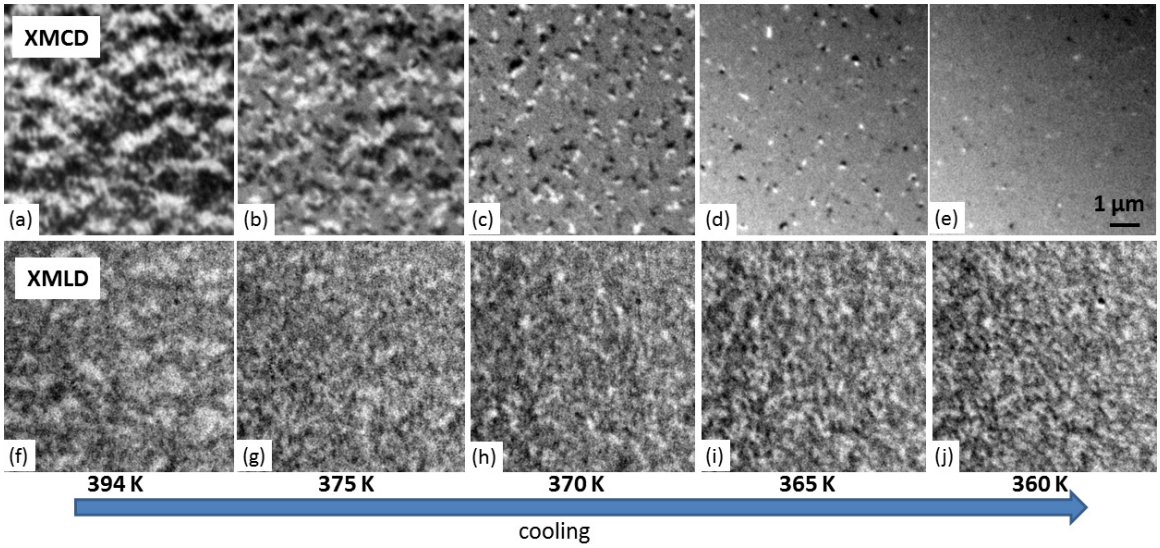

Figure 5.5: Comparison of (a)-(e) XMCD and (f)-(j) XMLD PEEM images recorded upon cooling of FeRh thin film from 395 K (fully FM) to 360 K (mostly AF). Several intermediate mixed phase state are shown at 375 K, 370 K and 365 K. Each XMLD-PEEM image is obtained by averaging 60 snapshots taken at two different energies (E_1 =710.8 eV, E_2 =711.8 eV) and two different polarizations (parallel p and perpendicular s) (240 snapshots total) and computing $(p(E_1)/s(E_1))/(p(E_2)/s(E_2))$ so as to maximize the XMLD contrast. Each XMCD-PEEM images is obtained by averaging 6 snapshots taken at the Fe L_3 edge for opposite circular polarization (12 snapshots total) and dividing them (approximation of asymmetry).

previous observation reported in Chapter 4 and ref. [24]. The XMLD images taken at 394 K show the FM domain structure, as previously discussed; those taken at 375 K and below show a structure finer than the FM structure with no change striking to the eye from 370 to 360 K.

5.4 Discussion

To study in more detail the evolution of FM and AF domains across the FM to AF transition upon cooling, we use the correlation length analysis described in Section 5.2. Figure 5.6 shows the average radial profile of the autocorrelation of the XMCD images at all 5 temperatures. The x axis has been converted from pixel to nm based on the magnification of the microscope used. All images were recorded with a field of view of 10 μm onto a CCD of 1024×1024 pixels. The steepness of the autocorrelation profile increases with decreasing temperature, indicating a decrease in the correlation length. The first 3 temperature steps (394 K to 370 K) show a single

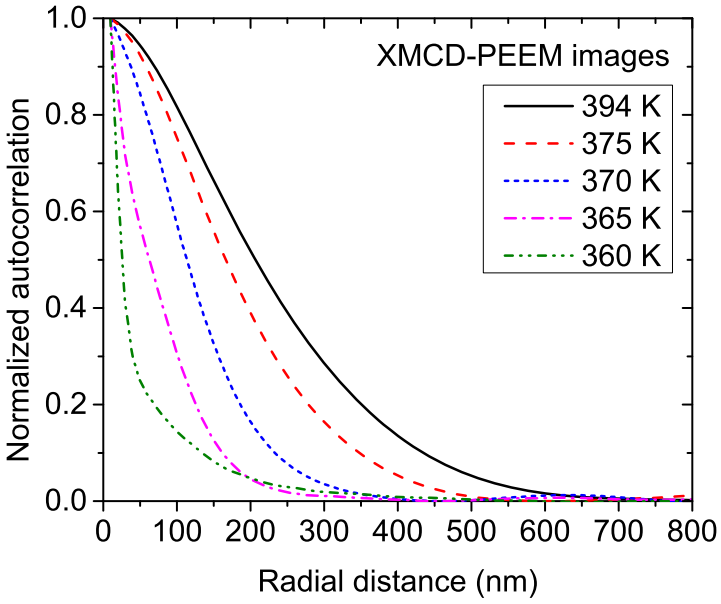

Figure 5.6: Normalized autocorrelation profile (radially averaged) for XMCD images at 394 K, 375 K, 370 K, 365 K and 360 K. Note that the magnitude of the autocorrelation signal decreases as the temperature decreases (due to decrease in number of pixels that carry a FM signal), but we choose to show here the normalized signal to emphasize the change in correlation length.

smooth decaying curve while the 365 K and 360 K curves become sharper and have a kink, especially visible at 360 K. The appearance of the kink is due to the increase in relative magnitude of contribution from the detector resulting in a sharp Gaussian with small correlation length near the origin. Above 370 K, the number of pixels that carry a FM signal is large compared to the non-magnetic background. Below 365 K, FM pixels are a minority compared to the background, and the contribution from the detector is dominant in the autocorrelation.

We compute the correlation length for XMCD images taken above 370 K from a single Gaussian fit to the radial average of the autocorrelation and find that it ranges from 554±15 nm at 394 K to 323±10 nm at 370 K. Figure 5.7 shows that the correlation length is a good quantitative measure of the average FM domain size. Circles of diameter equal to the correlation length are overlaid on the XMCD images taken at 394 K (Fig. 5.7 (a)) and 370 K (Fig. 5.7 (b)) and show a good agreement with the size of the domains observed at each temperature. The FM domains at 370 K are smaller in size because the FM phase coexists with the AF phase, so only finite regions of the film are FM as opposed to the entire field of view at 394 K.

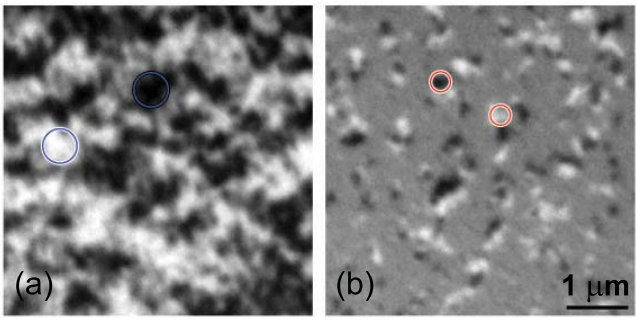

Figure 5.7: Comparison of the correlation length as calculated by the autocorrelation method to the observed FM domain size at (a) 394 K with circles of diameter 554 nm and (b) 370 K with circles of diameter 323 nm.

While a single Gaussian fit works well for XMCD images ranging from 394 K to 370 K, the strong contribution from the detector point spread function in the autocorrelation profiles at 365 and 360 K is seen in Fig. 5.6. At 365 K and below, the autocorrelation profiles are fit to two Gaussians, as shown in Fig. 5.8. The Gaussian with the smaller decay length corresponds to the point spread function of the detector being 48±2 nm. A single pixel is equivalent to 9.8 nm. Therefore the detector is found to induce a spread of ∼5 pixels. Next we look at the relative magnitude of the detector Gaussian compared to the second Gaussian. Both Gaussians are plotted in Fig. 5.8 (a) and (b). While at 365 K, the detector Gaussian is lower than the second Gaussian, the opposite is seen at 360 K. Note that the amplitude of the normalized autocorrelation at the kink is a good estimate of the magnitude of the second Gaussian. This means that at 360 K, the amplitude of the physical signal is lost in the instrument broadening and noise and the correlation length analysis is not meaningful. This is consistent with the fact that the number of pixels with FM contrast is not large enough for a statistically meaningful autocorrelation analysis. The low amplitude broad residual contribution to the autocorrelation is attributed to error from an imperfect background subtraction. 365 K is at the limit, with the detector Gaussian height at 0.3 and the signal Gaussian height at 0.65, just a factor of 2 larger. From the second broader Gaussian, we extract a length of 233±8 nm.

We now compute the normalized autocorrelation radial profiles of the XMLD images from Fig. 5.5. In Fig. 5.9 we notice that the autocorrelation radial functions of the XMLD images from 375 K to 360 K are very similar in shape to the XMCD at 365 and 360 K, with a sharp peak near the origin and a second broader peak overlaid. This could indicate that the autocorrelation analysis will also reach its limit on the XMLD images.

By applying the same two-Gaussian fit as for the 365 K XMCD image autocorrelation to the 394 K XMLD image, we find a detector spread of 53 nm (consistent

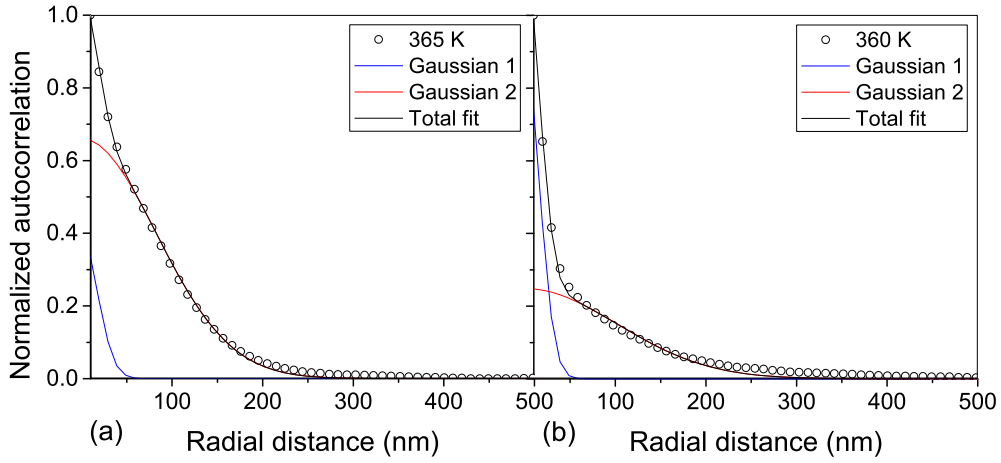

Figure 5.8: Double Gaussian fits of autocorrelation radial profiles at (a) 365 K and (b) 360 K. Each separate Gaussian is shown as well as the total fit of the sum of both Gaussians. The relative magnitude of the two Gaussians with each other is evidenced.

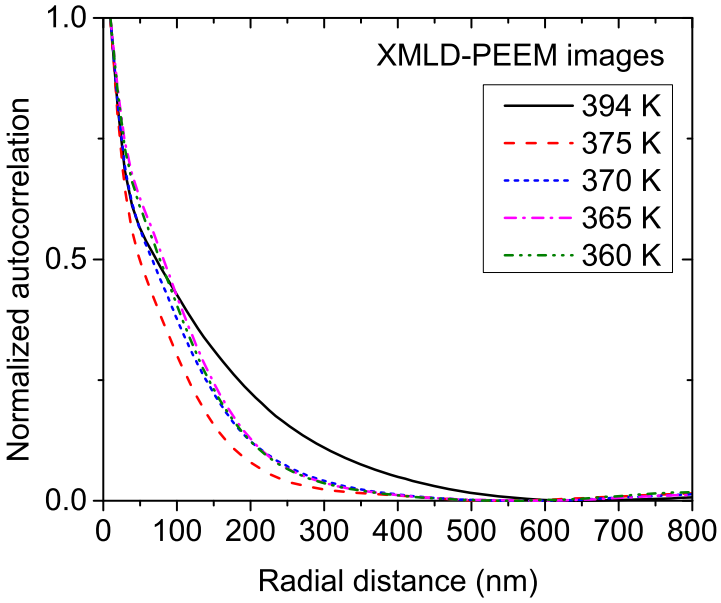

Figure 5.9: Normalized autocorrelation profile (radially averaged) for XMLD images at 394 K, 375 K, 370 K, 365 K and 360 K.

with 48±2 nm) and a correlation length of 457±10 nm. This is ∼100 nm lower than the correlation length of the XMCD image at the same temperature. We attribute the discrepancy to the lower magnitude of the XMLD signal compared to the XMCD signal. Indeed while the XMCD autocorrelation is dominated by the magnetic signal, almost half of the XMLD autocorrelation amplitude is due to the detector spread. This difference in signal quality is further confirmed by comparing the contrast to noise ratio (CNR) of the XMCD and XMLD images of the same FM domain pattern recorded at 394 K. CNR is similar to the signal to noise ratio but is defined as the difference in signal intensities for signal producing structures A and B in the region of interest, divided by the standard deviation of the pure image noise:

$$C = \frac{|S_A - S_B|}{\sigma} \tag{5.7}$$

The two structures A and B are two different FM domains, the signal S is the mean pixel intensity of the XMCD or XMLD image over the specific domain and σ is estimated by the standard deviation of S across a single domain. Calculation for a representative pair of domains with opposite contrast gives a CNR of 22.8 for the XMCD image and 8.4 for the XMLD image. The reduction in CNR by a factor of almost 3 indicates that, similar to the case of the 365 K XMCD image, we are at the limit of the autocorrelation and correlation length analysis.

The change in correlation length with temperature as calculated for each XMCD image and each XMLD image is shown in Fig. 5.10. The XMCD correlation length, a good measure of the average FM domain size, decreases gradually upon cooling, following the decrease in size of FM regions. The XMLD correlation length starts near the XMCD at 394 K in the FM phase, consistent with the fact that both XMCD and XMLD images resolve the FM structure in the fully FM phase. It then follows a sharp decrease to 279 nm at 375 K, outside the typical error bars of 10 nm, before increasing slightly above 300 nm and remaining mostly constant upon subsequent cooling. Note that 300 nm is much larger than the spatial resolution limit of the microscope since FM nuclei as small as 60 nm are resolved in XMCD images.

The almost absence of change in the evolution of the XMLD images morphology and their correlation length upon cooling below 370 K can be due to two possible reasons: (1) the AF domain size is below the spatial resolution limit of the microscope (30 to 60 nm), (2) the AF domains experience little or no growth below 370 K. An AF phase transformation limited by nucleation is consistent with the knowledge that AF domains are typically associated with crystallographic defects, therefore their size is limited by the size of defect-free regions in the FeRh thin film. Both explanations therefore point to a small AF domain size (300 nm or less) limited by defects. The average crystallite size determined by Scherrer's formula on a 001 peak for FeRh thin films of similar quality to this one is 33 nm. The 300 nm correlation length is an order of magnitude higher and could correspond to the size of groups of several AF domains, instead of single domains, or the AF domains could cover an average of

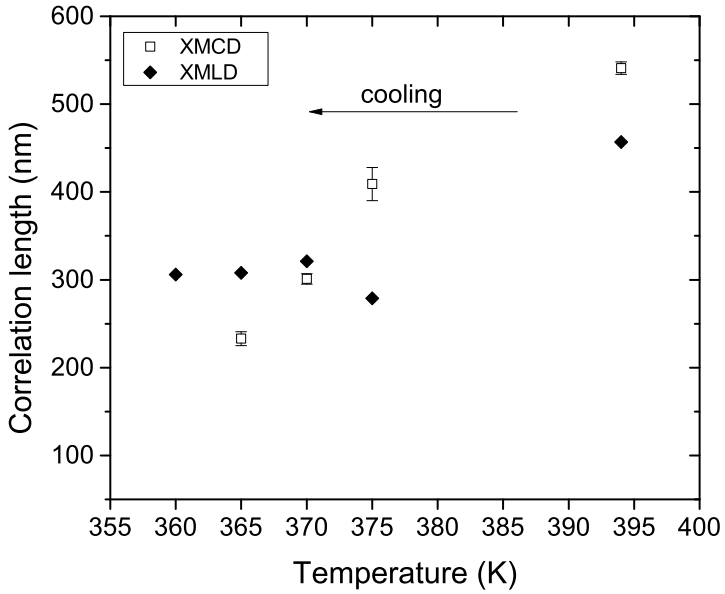

Figure 5.10: Evolution of the correlation length of XMCD and XMLD images with temperature. The correlation length is equal to twice the Gaussian fit parameter (of the broader Gaussian when two Gaussians are used). A single Gaussian fit was used for XMCD autocorrelations at 394 K, 375 K and 370 K and a double Gaussian fit was used for XMCD autocorrelation at 365 K, and for all XMLD autocorrelations.

10 grains. The features actually appear smaller to the eye in the images but due to the high noise level, their size is difficult to measure. The larger correlation length could also be due to a domain morphology that is not granular (e.g. meandering domains) [85].

We acknowledge that the correlation length analysis might be at the limit of its validity for the XMLD images. To show that the AF features are nevertheless spatially resolved in the XMLD images, we turn to a cross-correlation analysis of XMLD images at different temperatures, as a way to evidence a progressive evolution of features in the images. Two cross-correlation images are shown in Fig. 5.11 with the autocorrelation of the 365 K image for comparison. Cross-correlations between XMLD image at a given temperature step and the temperature step immediately preceding and following have a global maximum at the origin. This means that the two successive images are spatially correlated and that many of the features are the same between the two images. A cross-correlation analysis of the XMLD images at 394 K and 360 K shows that they are not correlated confirming that the FM and AF phase morphologies are different (not shown).

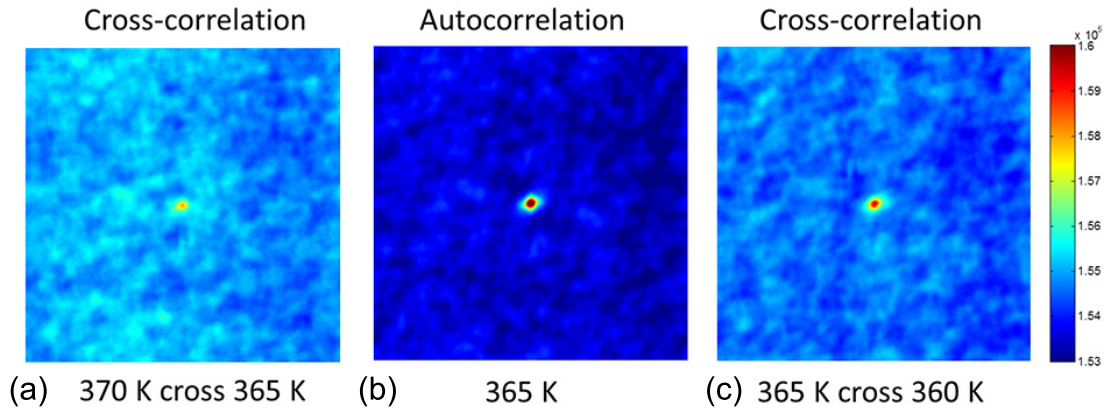

Figure 5.11: Autocorrelation of 365 K XMLD image (recorded upon a second cooling cycle) and cross-correlation with 370 K and 360 K images. Care was taken to compute the cross-correlation of the exact same region of the sample.

To further look at the nucleation of AF domains, we repeated the imaging of AF and FM phase in the same region of the sample upon a second cooling cycle. In the case of heterogeneous nucleation, nucleation starts preferentially at defect sites. Although we do not spatially resolve the defects here, by comparing the nucleation sites between two different cooling cycles, we can determine to what extent they affect the transition. After a full transition upon cooling was recorded from 394 K to 360 K as shown in Fig. 5.5, the sample was heated back to 394 K and the same temperature steps were recorded during the second cooling. Figure 5.12 shows the identical region of the sample in the fully FM phase (XMCD images (a) and (b)) before the first and second cooling, and in the mostly AF phase (XMLD images (d) and (e)) after the first and second cooling. The cross-correlation of the two XMCD images, shown in Fig. 5.12 (c), allows us to determine how similar the first and second FM domain patterns are, which is otherwise difficult to evaluate visually. The absence of global maximum at the center of the image indicates that no long-range correlation exists between the first and second FM patterns. In contrast, the same cross-correlation evaluation of the two XMLD images, shown in Fig. 5.12 (f), finds a global maximum at the center which means that the two images are strongly spatially correlated. Note that in Chapter 4 we showed that the nucleation of FM domains upon heating is heterogeneous, with a spread in nucleation temperature and a correspondence between the initial nucleation sites upon heating and the last remaining FM regions upon cooling. This heterogeneous nucleation nevertheless leads to a final FM domain structure that is not as sensitive to defects and is not reproducible between repeated heating cycles.

The observation of spatial correlation between the AF structures obtained in two separate cooling cycles is consistent with our interpretation that the AF domains are

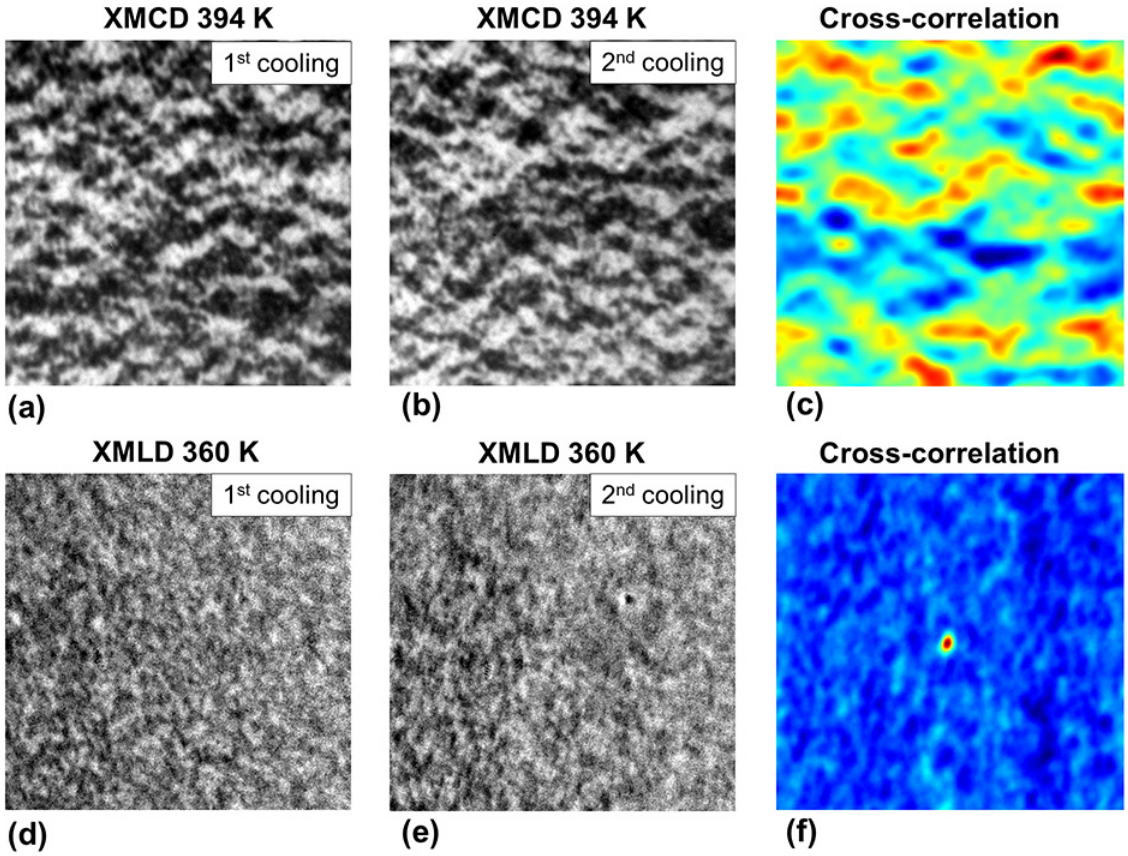

Figure 5.12: Side by side comparison of XMCD and XMLD images recorded at the same temperature during 2 successive cooling cycles. XMCD images at 394 K in the fully FM phase before (a) the first cooling cycle, (b) the second cooling cycle, and their cross-correlation image (c). XMLD images at 360 K (mostly AF phase) at the end of (d) the first cooling cycle, (e) the second cooling cycle, and their cross-correlation image (f).

influenced by crystallographic defects. Even though the initial FM matrix is different between the two cooling steps, the final AF structure obtained is similar. This structure is not random. We suggest that the AF domains are pinned by the FeRh thin film surface defects which are stable through this temperature range, including the transition.

5.5 Summary

In summary, we showed that XMLD-PEEM can be used to spatially resolve the AF phase in FeRh thin film. As expected, the FM phase was detected by XMLD-PEEM as well. We established the magnetic origin of the XMLD features in the FM phase, and by comparison of FeRh XLD spectra with known XMLD spectra, extended the magnetic origin to the AF phase as well. Autocorrelation analysis was used to determine the characteristic length of the magnetic features in the XMCD and XMLD images. While in the XMCD images the correlation length proved to be a good measure of the average FM domain size, the accuracy of this analysis was limited for the XMLD images. A correlation length of $\sim$300 nm was computed for the AF phase. This value could correspond to the size of groups of several AF domains, instead of single domains, and point to an AF domain size limited by defects. By studying the cross-correlation of successive XMLD images, we evidenced small local changes in the AF morphology upon cooling, further confirming the spatial resolution of the AF phase. Finally, we found that a non-random similar AF structure is reproduced by repeating the cooling transition, confirming that the AF domains are correlated to defects. We hope that this work will be useful for continued microscopic studies of the FeRh AF phase as well as other metallic AFs.

Chapter 6

Effect of capping material on interfacial ferromagnetism

6.1 Introduction

In most of the thin-film studies, both fundamental and applied, FeRh is capped with a thin film layer to protect against oxidation, commonly a noble metal (Au, Pt) or a light self-passivating metal such as Al. This is especially important for magnetic and structural studies based on surface-sensitive probes. However a series of recent studies have showed that substrate and capping materials can induce interfacial effects where the magnetic properties of the FeRh film are modified near the interface with the capping layer as well as the substrate [20, 21, 22, 24]. Specifically, a thin FM layer can be stabilized at temperatures where the stable phase in the bulk is AF, referred to in this work as interfacial FM. These interfacial effects are directly relevant to the successful integration of FeRh in HAMR technology.

Interfacial FM at RT has been previously observed by total electron yield XMCD in FeRh thin films capped with MgO and Au by Ding *et al.* [20] and by magnetic depth profile modeling of polarized neutron reflectometry results in FeRh capped with MgO by Fan *et al.* [21]. Both studies confirmed the presence of interfacial FM near the top interface, but with a highly reduced signal compared to that of a fully FM film at 400 K. The interfacial FM was attributed to a combination of the effect of strain and Fe deficiency causing a mixed state of FeRh CsCl α (FM) and fcc γ (PM) phases with reduced moment and lowered AF-FM transition temperature T_0 compared to the single FeRh α phase. For the film capped with MgO, an extremely weak interfacial moment of 0.02 μ_B/atom (compared to 1.56 μ_B/atom for FM film at 400 K) is estimated.

Our group recently reported on interfacial FM observed at RT with XMCD-PEEM on FeRh films capped with Al; these films are nominally AF at room temperature (RT) according to magnetometry characterization [24]. The interface with the FeRh

native oxide of an uncapped film was found to be non-magnetic.

Finally, Loving *et al.* [22] used diffusion from an Au capping layer to tune T_0 of FeRh thin films, showing that a structure with a magnetization gradient as a function of depth can be created. In particular they found interfacial FM in films where the FeRh and Au had been deposited at high temperature, thereby allowing inter-diffusion between the two. These previous works point to effects coming from a combination of strain, Fe deficiency, and chemical diffusion from the cap but the variety of systems studied and experimental techniques used renders the interpretation difficult. A systematic study of the effect of different materials is required to elucidate the role of chemical diffusion and is the focus of this paper.

T_0 has been shown to be sensitive to small changes in at. % Rh composition as indicated in the reported phase diagrams for the Fe-Rh system [6, 16] constructed from data on bulk samples. The effect of the composition on T_0 (here defined as the average of T_{AF-FM} and T_{FM-AF}) has been reported in thin films as well [25, 86]. In particular we have observed a significant reduction of 10 K per 1 at. % Rh composition change (from 397 K at 48.5 at. % Rh to 367 K at 51.5 at. % Rh, see Section 2.6). For lower Rh concentration, we found that alloys with composition $\leq$ 47.5 at. % Rh are FM from 300 K to 10 K, in good agreement with the existing phase diagrams indicating that the AF phase exists only over a small composition range near equiatomic(see Section 2.6). Deviations from equiatomic composition of a few at.% can thus significantly lower T_0 or even stabilize the FM phase over the entire temperature range. Doping with small amounts (1 to 10 at.%) of ternary metallic elements also affects this sensitive system [46, 87, 88, 89]. Some elements such as Ni and Pd lower T_0, while others such as Ir and Pt raise it. An increased T_0 (near 500 K for 5 to 10 at. % Pt) improves the suitability of FeRh for magnetic recording. In addition, the likely high anisotropy media that FeRh would be coupled to is FePt, and therefore understanding the effect of Pt diffusion on interfacial FeRh is crucial [17, 89, 90].

In this work, we use a surface sensitive magnetic spectromicroscopy technique to directly probe the magnetic structure in the region near the interface with different capping layers and polarized neutron reflectivity to model the magnetic profile of the different samples as a function of depth to understand the origin of the interfacial effects. In an effort to focus on the chemical effects such as species segregation and diffusion at the interface, we systematically studied 5 different capping materials. Due to the differences in cap material, growth modes and small variations in cap thicknesses, a constant strain state is not guaranteed between the different samples, nevertheless attempts were made at keeping differences in strain state small by keeping the thickness of the cap small (1.8 to 2.5 nm) compared to the thickness of the FeRh layer of $\sim$100 nm and depositing all caps at RT to eliminate differential thermal expansion between the two layers. All films were grown at the same temperature and on the same substrate.

The effect of 5 different caps was studied: three metallic caps, Al, Pt and Ag and two oxides, FeRh native oxide and alumina. The effect of two alumina caps with

different thicknesses (1.8 and 2.5 nm) was also studied to look for any strain effect. The magnetic domain structure is imaged in the region near the interface between FeRh and these different caps (native oxide, alumina 1 and 2, Al, Pt) below and above T_0 and the magnetic and structural depth profile is modeled below and above T_0 (Al, Ag). In addition, the magnetic domain structure in the region near the interface between FeRh and Ag is imaged at RT.

6.2 Experimental methods

Thin films of FeRh (001) with ∼100 nm thickness were grown by magnetron sputtering from a FeRh alloy target onto (001) MgO substrates. The base pressure in the chamber was 8×10^{-8} Torr. The growth was performed at a substrate temperature of 873 K, using a DC power of 40 W and an argon pressure of 2 mTorr. The growth rate measured by a quartz crystal microbalance was 0.04 nm/s. The films were subsequently given one of the following treatments: (1) left uncapped to allow the formation of a native oxide with a thickness estimated by hard x-ray photoemission spectroscopy measurements to be less than 2 nm, (2) capped *in-situ* (without breaking high vacuum) with 1.8 nm or 2.5 nm of alumina by reactive sputtering from an Al target, or with 1.8 nm of sputtered Pt, (3) capped *ex-situ* (after exposure to atmosphere) with 2.5 nm of sputtered Al or with 2.5 nm of sputtered Ag. Note that all capping depositions were done at RT to minimize inter-diffusion between the FeRh film and the capping layer and to eliminate differences in strain induced by differential thermal contraction of cap and FeRh. The films capped without breaking high vacuum were allowed to cool to RT (2 hours minimum) before subsequent deposition, therefore resulting in a similar potential exposure to water and other oxidants as the films capped after exposure to atmosphere (a monolayer of adsorbed gas molecules is formed on the surface of the FeRh film in less than 30 sec at 8×10^{-8} Torr). Hence in this work we do not distinguish between capped *ex-situ* and *in-situ*. The thickness of the deposited caps was controlled based on the calibrated rate of deposition of each material (thickness of calibration films measured by profilometry).

The magnetic phase transition of all samples was measured by SQUID magnetometry. Figure 6.1 shows the temperature dependence of the magnetization of the 5 different samples in an applied field of 5 T. By correcting for the effect of the applied magnetic field on T_0 (-8 K/T), we find that all 5 samples are fully AF below 340 K and fully FM above 410 K in zero applied magnetic field. The spread in transition temperature observed between the 5 different samples is attributed to the extreme sensitivity of T_0 on external factors such as small changes in Fe composition. A measured composition shift of 2 at. % between different samples is due to the drift in sputter target composition over time because of non-equal sputtering yields between Fe and Rh species. T_0 follows the expected trend of decreasing with increasing Rh concentration. Note that SQUID magnetometry measurements of $M(H)$ at 300 K

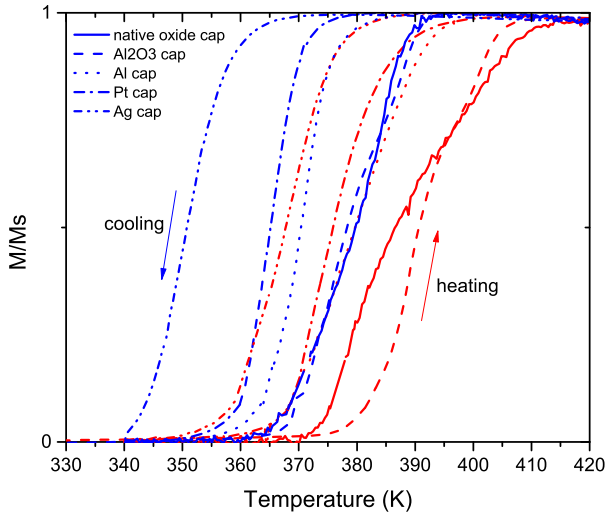

Figure 6.1: Temperature dependent magnetization of FeRh films with different caps showing the hysteretic transition from AF (near zero magnetization) to FM phase. The transition was measured in an external field of 5 T and the temperature axis has been corrected to reflect the transition in no external field. Note that all films are fully FM above 410 K and fully AF below 340 K. M is normalized by its high T, fully FM value to account for small differences in composition.

show a small residual FM component in all films. A saturation magnetization of 80 to 100 emu/cc is measured at 300 K, 7 to 10 % of the fully FM state at 400 K. Since SQUID magnetometry is not a local technique we cannot determine whether this contribution is distributed through the film, originates from either the top or bottom interface, or if it is a combination of both. A surface sensitive or depth sensitive technique is necessary to detect the presence of any interfacial FM layer.

Table 6.1 summarizes the structural and chemical information of the different FeRh/cap systems. The structural and chemical ordering quality of each film was checked by x-ray diffractometry and showed small deviation in the mosaicity and coherence length between the different films with respective average values of 0.34±0.02 and 35±1 nm, as well as similar lattice parameters indicating a cubic structure with negligible tetragonal strain within our measurement accuracy (±0.3%). The chemical order parameter S determined on separate uncapped FeRh films grown under the same condition is $S = 0.88\pm.03$. The film and cap thicknesses and the roughness of the interface were determined by x-ray reflectivity. The Al and alumina caps are thicker than nominal thickness based on deposition rate due to the oxidation of the Al. The interface roughness of the films is similar for all samples (1 to 4 nm), in good

Sample cap	No cap	Al	Pt	Alumina	Ag
Nominal cap thickness (nm)	N/A	2.5	1.8	2.5	2.5
Rh composition (at. %)	50.4	50.4	51.2	51.5	52.5
c (nm)	0.2988	0.2988	0.2982	0.2983	–
a (nm)	0.2990	0.2990	0.2992	0.2990	–
c/a (%)	99.9	99.9	99.7	99.8	–
Coherence length (nm)	34	34	36	34	–
Mosaicity (deg)	0.33	0.33	0.32	0.38	–
Film thickness (nm)	95	95	110	97	103
Cap thickness (nm)	N/A	5.6	–	7.5	7.4
Cap-film interface (nm)	N/A	1.5	–	3.8	4.3

Table 6.1: Summary of films and caps structural and chemical parameters.

agreement with the topography of uncapped FeRh films measured by atomic force microscopy which shows rms roughness of ∼5 nm. Note that the reflectivity model does not distinguish between a topographically rough interface and a chemically diffuse interface, and therefore both could contribute to the measured roughness. An accurate value of the roughness of the interface could not be determined from the x-ray reflectivity model fit for the FeRh film capped with Pt (non-detectable oscillations possibly due to a non-uniform Pt film or Pt islands) so the cap thickness value reported in Table 1 is the nominal deposition thickness. The composition of the films was measured by Rutherford backscattering spectrometry.

X-ray magnetic circular dichroism (XMCD) in photoemission electron microscopy (PEEM) is a surface sensitive magnetic microscopy technique suitable for the study of interfacial magnetic phenomena in buried layers due to its element selectivity and the penetration of the x-ray photons. The probing depth is the distance at which the recorded intensity decreases by a factor of e and is typically around 5 nm in metallic samples. The intensity of buried signal decreases exponentially with thickness but can be measured by increasing the integration time. In the samples studied here, all sample-cap interface regions were within the probing depth.

XMCD-PEEM imaging was performed at beamline UE49-PGM-a-SPEEM at the BESSY II synchrotron, at the Fe L_3 edge (705.6 eV), using low-energy secondary electrons with a spatial resolution of ∼30 nm. Magnetic contrast images were computed as described in ref. [24] by plotting the XMCD asymmetry at the Fe L_3 edge. XMCD asymmetry measures the strength of the projection of the magnetization along the propagation direction of the incoming x-ray beam. Saturated blue (red) in the selected color scale highlights magnetic domains with a projection of the magnetization aligned parallel (antiparallel) to the propagation direction of the photons. The color gradient indicates a lower magnetization or a departure of the local magnetization direction from the x-ray beam direction. No external magnetic field was applied during

the measurement. Images were recorded in the initial RT state (nominally AF), then in the fully FM phase between 400 K and 420 K and finally at RT again to check the stability of the initial interfacial phase.

PNR was performed on the MAGIK reflectometer at the NIST Center for Neutron Research as a function of temperature in order to fully characterize the depth-dependence of the magnetization [91]. Spin-polarized neutrons were specularly reflected from the sample in an applied field of 0.68 T at 450 K in the nominally FM phase and 300 K in the nominally AF phase. At each temperature, all four cross sections (non-spin flip and spin flip) were measured as a function of wave vector Q. Beam footprint and polarization efficiency corrections were applied to the raw data. No features were observed in the spin flip cross sections, confirming that all the magnetizations are in the plane of the film, parallel to the applied field. The resultant non-spin flip cross sections (– and ++) at both temperatures were fit to a model for the chemical and magnetic scattering length density (SLD) depth profiles for the stack MgO/FeRh/cap in order to isolate the magnetization near the bottom and top interfaces of the FeRh films at RT. The FeRh layer was divided into 3 layers with different magnetic SLDs and the model was then fitted to the experimental data using refl1D PNR software [92]. The data at different temperatures were fitted simultaneously, with the chemical SLDs, layer thicknesses and interface roughnesses the same between the two temperatures and only the magnetic SLDs allowed to vary.

6.3 Results

Figure 6.2 shows the XMCD asymmetry corresponding to the interfacial FeRh phase at different temperatures for the FeRh thin film capped with Al. Similar to other studies with a Au capping layer [20, 22] we find that the Al cap induces a RT FM interfacial layer that is stable to thermal cycling. The interfacial FM has a reduced contrast compared to the fully FM phase, but is clearly visible. Changes in XMCD-PEEM magnetic contrast can generally be attributed to 3 separate factors: the magnitude of the Fe moments, the fraction of Fe atoms that carry a FM moment and the direction of the Fe moments. Metallic doping by a non-magnetic element has been shown to reduce the Fe magnetic moment in FeRh [22, 46, 87, 88] and it is the most likely factor. The observed reduced magnetic signal can also be the result of a thin FM layer compared to the probing depth of ca. 5 nm, or a combination of these two factors.

We used PNR to separate these two factors and determine the thickness of the interfacial FM layer giving rise to this signal and the magnitude of the magnetic moment carried in this layer. Figure 6.3 shows the resultant non-spin flip cross sections (– and ++) at both temperatures (Fig. 6.3 (a) and (b)) and the corresponding structural and magnetic layers model which was fit to the data (Fig. 6.3 (c) and (d)).

Our structural and magnetic layers model is in excellent agreement with the high

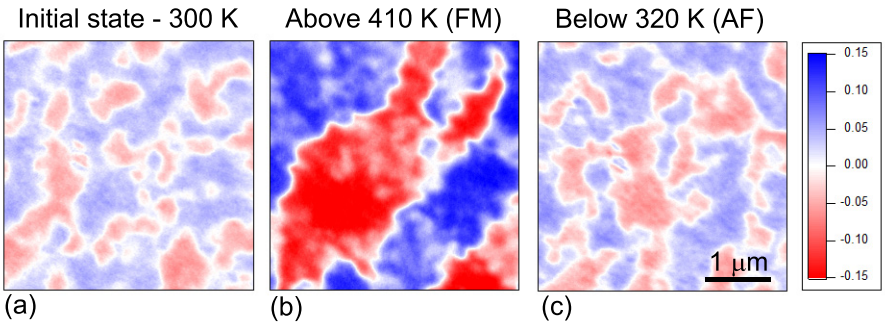

Figure 6.2: XMCD-PEEM asymmetry images of FeRh thin film capped with Al at (a) the initial RT state, (b) above 410 K in the fully FM phase, (c) cooled back below 320 K in the nominally AF phase. The interfacial FM layer is stable to temperature cycling. The labels (FM) and (AF) indicate the nominal phase according to bulk magnetization measurements.

temperature PNR experimental data. The magnetic moment per FeRh atom of the fully FM layer is 1.61 μ_B in good agreement with the saturation magnetization measured by magnetometry of 1.77 μ_B. The model is also in good agreement with the RT data. It requires the presence of a non-negligible magnetic layer at the interface between the FeRh layer and the Al cap at RT. The interfacial magnetic layer is modeled to have a thickness of 7 nm with a magnetic SLD of $0.50\times10^{-6}\mathring{A}^{-2}$ which corresponds to a magnetic moment of 0.23 μ_B.

In addition, the PNR reveals that there is a magnetic layer at the MgO/FeRh substrate interface as shown by the magnetic SLD in Fig. 6.3 (d) and in good agreement with previous observations in Ref. [21]. This magnetic layer can be attributed to a Rh-rich layer near the bottom interface as observed in Ref. [22]. Indeed both the x-ray reflectivity and PNR fits are improved by inclusion of this Rh-rich layer. We speculate that this variation in the FeRh composition with depth is due to Fe deficiency because of Fe diffusion into the MgO substrate. Interfacial diffusion between Fe and MgO has been reported in studies related to magnetic tunnel junctions with formation of an inter-diffused (Mg,Fe)O layer at the interface after annealing to temperatures above 450°C [93, 94]. Our films are deposited at 600°C and a similar effect would result in Fe depletion in the bottom layer, therefore increasing the Rh concentration locally. As discussed in the introduction an increase in Rh concentration lowers T_0 and can lead to the stabilization of the FM phase at RT.

Note that the magnetic moment of 0.23 μ_B, found at the interface with the Al cap, is an order of magnitude larger than the interfacial FM reported by Fan *et al.* of 0.02 μ_B for a FeRh film capped with MgO [21], indicating that the effect of a metallic cap on the interfacial FM is stronger than that of an oxide cap.

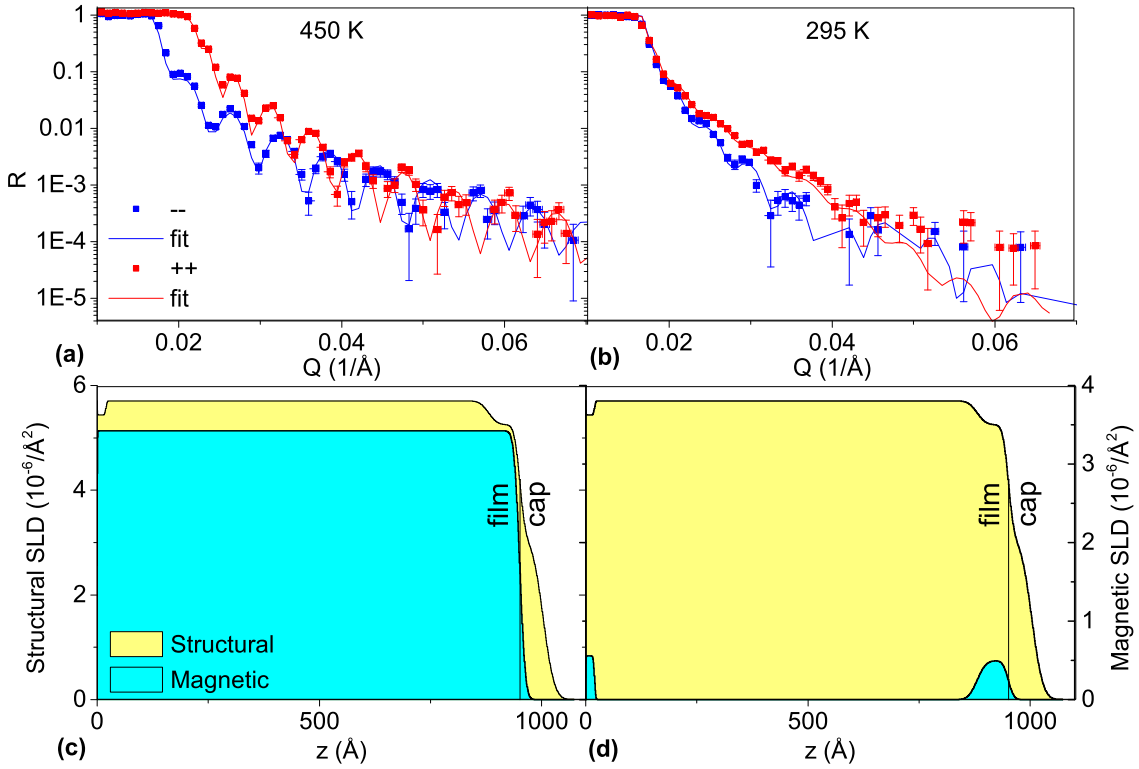

Figure 6.3: PNR reflectivity curves for FeRh capped with Al at (a) 450 K (fully FM) and (b) 295 K (interfacial FM only) and corresponding structural and magnetic profile models (c) and (d).

In order to further compare the effect of an oxide to that of Al, a FeRh film capped with alumina was then studied. Figure 6.4 shows the magnetic contrast images of the FeRh film capped with alumina. A surprising behavior is observed: interfacial FM is seen initially at RT and disappears after the first heating-cooling cycle and subsequent temperature cycles. The FeRh film capped with a thinner alumina layer (nominal 1.8 nm compared to 2.5 nm) shows the same behavior. X-ray photoemission spectroscopy (XPS) of the sample reveals that the alumina cap is initially not chemically homogeneous: it contains oxidized and metallic aluminum atoms. The initial FM interface is attributed to the presence of some metallic Al at the interface, which upon small heating reacts with and is incorporated into the alumina cap.

To confirm our explanation we turn to the detailed analysis of the XPS Al, Fe and Rh peaks, before and after heating. Figure 6.5 (a) shows the Al 2p XPS peaks

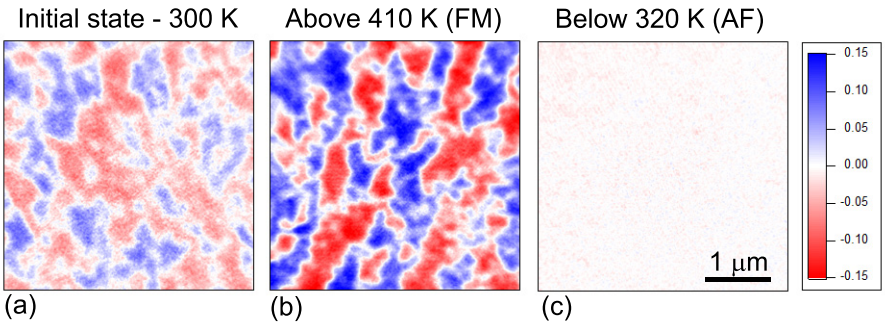

Figure 6.4: XMCD-PEEM asymmetry images of FeRh thin film capped with alumina at (a) the initial RT state, (b) above 410 K in the fully FM phase, (c) cooled back below 320 K in the fully AF phase. While initial FM domains are seen in the RT image (a), after heating to the fully FM phase and cooling back below the transition temperature no interfacial FM persists and instead a fully AF interface is seen. This AF phase is stable to further heating and cooling cycles.

measured before and after heating. A strong presence of metallic Al is seen before heating as indicated by the double peak fit. A rough estimate gives that only 50 % of the layer is initially oxidized. After heating, only one chemical state is observed in Al 2p XPS peak within our resolution limit. The small energy shift between the two spectra is due to a different band alignment, as confirmed by the binding energy of O 1s peak (not shown). Further comparison of the XPS spectra before and after heating shows that the Fe and Rh elemental peaks have a reduced amplitude after heating (Fig. 6.5 (b) and (c)), indicating that the thickness of the capping layer is increasing, in good agreement with the formation of more oxide ($\sim$1 nm of extra alumina cap as estimated from the magnitude of the reduction). Note that a change in morphology of the cap could cause additional damping of the Fe and Rh peaks.

To support our claim that a stable and fully oxidized cap does not generate any interfacial FM, we turn to an uncapped film that was previously studied for the nucleation and growth of the FM phase presented in Chapter 4. This film is effectively capped with a native oxide. Hard x-ray photoemission spectroscopy of the Fe 2p and Rh 3d core levels reveals that Rh is present in the metallic state only and that the native oxide is composed of Fe oxide. Note that although Fe 2p and Rh 3d levels are accessible by soft x-rays, hard x-rays were used to probe deeper into the film. The most probable candidate according to the structure of the Fe 2p peak is Fe_2O_3, with a thickness estimated at 2 nm.

Figure 6.6 shows the magnetic contrast images recorded during the full heating and cooling cycle (AF, FM, AF again). No detectable FM phase is observed at the interface with the native oxide. A structure of large FM domains with strong

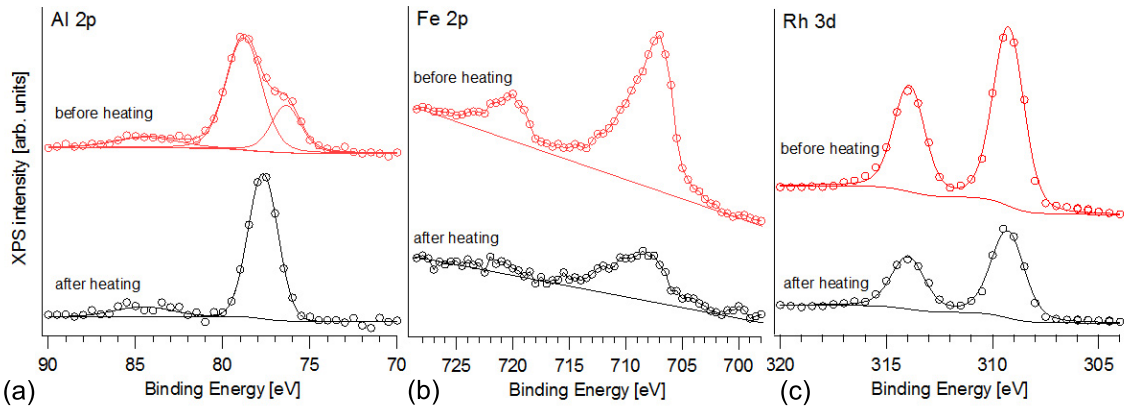

Figure 6.5: XPS spectra of FeRh thin film capped with alumina recorded at RT in the initial state (before heating) and after a full cycle of heating above 410 K and cooling back to RT (after heating), showing the details of (a) the Al 2p peak, (b) the Fe 2p peak and (c) the Rh 3d peak.

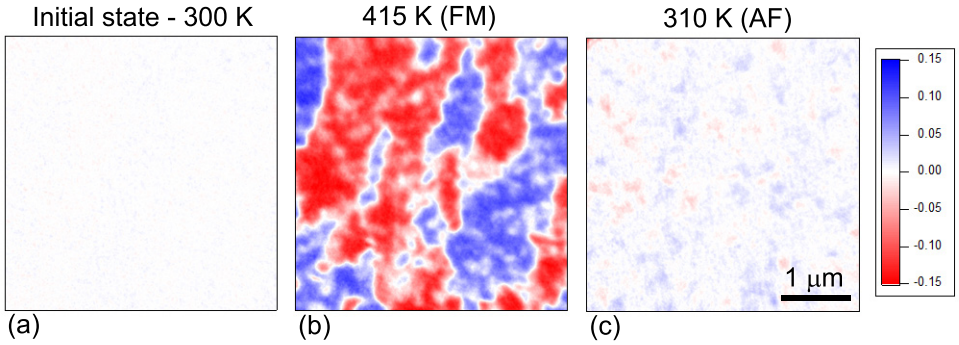

Figure 6.6: XMCD-PEEM asymmetry images of uncapped FeRh thin film, effectively capped with a native oxide of 2 nm or less at (a) the initial RT state, (b) 415 K in the fully FM phase, (c) cooled back to 310 K in the fully AF phase. The white color in the low temperature images (a) and (c) indicates the absence of FM domains, while the 415 K image (b) shows a strong FM contrast.

contrast is observed in the fully FM phase at 415 K similar to the structures seen in the film capped with Al and alumina. After cooling, a weak residual magnetic contrast is detected locally where the FM islands last disappeared but the majority of the background has no asymmetry, indicating its AF nature.

To further investigate the effect of a metallic cap, Fig. 6.7 shows the asymmetry images of a FeRh film capped with Pt. Unlike the film capped with the other metallic layer of Al, no interfacial FM is observed at RT, both in the initial state and after

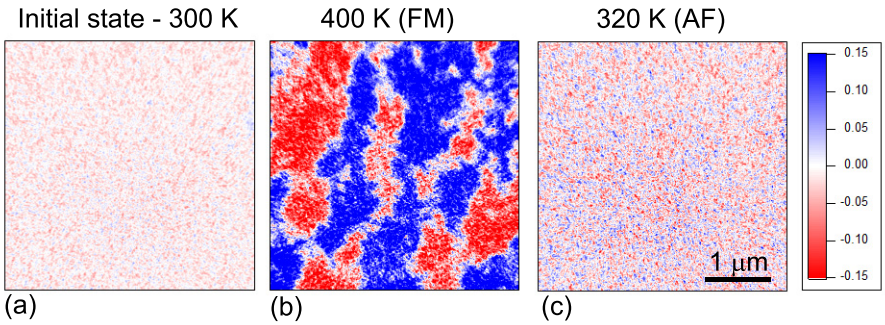

Figure 6.7: XMCD-PEEM asymmetry images of FeRh thin film capped with 1.8 nm of Pt at (a) the initial RT state, (b) 400 K in the fully FM phase, (c) cooled back to 320 K in the fully AF phase. Note that the initial and final images show only noise, so there is no interfacial FM at RT.

a full heating and cooling cycle. In the fully FM phase, the typical pattern of FM domains with strong FM contrast is seen again (the quality of these images is slightly reduced due to a lower acquisition time). Even in the case of a non-uniform film due to the formation of Pt islands, this shows that in the regions covered with Pt, the Pt results in the same absence of interfacial FM as the native oxide cap.

Finally, PNR measurement of a FeRh film capped with Ag was performed. The same methodology as for the Al capped film was used to perform the measurement and analyze the data. Figure 6.8 (a) shows the non-spin flip cross sections PNR at RT. The reflectivity data recorded at 450 K (not shown) is very similar to the film capped with Al and modeled with a fully FM layer of magnetic moment 1.60 μ_B (lower than film capped with Al due to a lower Fe concentration of the film overall). When comparing the RT reflectivity profile of the film with Ag cap to the Al capped film, it is clear that while the Al capped films showed a strong splitting between the ++ and – cross sections indicating the presence of FM at RT, splitting in the Ag capped film is minimal (close to the resolution limit), indicating that the magnetic signal at RT is negligible. Indeed a reasonable fit is obtained by assuming a model with no interfacial FM layer at the interface with the Ag cap at RT, shown in Fig. 6.8 (b).

Our data indicates that the magnetic component at the origin of the small splitting between ++ and – is located at the bottom interface with the MgO substrate, consistent with the observation of the Al capped film. In both samples, the bottom FM layer is ∼2 nm thick with a moment of 0.26 μ_B.

XMCD-PEEM of the FeRh/Ag interface near RT is in good agreement with the PNR results as shown in Fig. 6.8 (c), confirming the absence of interfacial FM. Note that the combination of the large roughness of the cap from the x-ray reflectivity

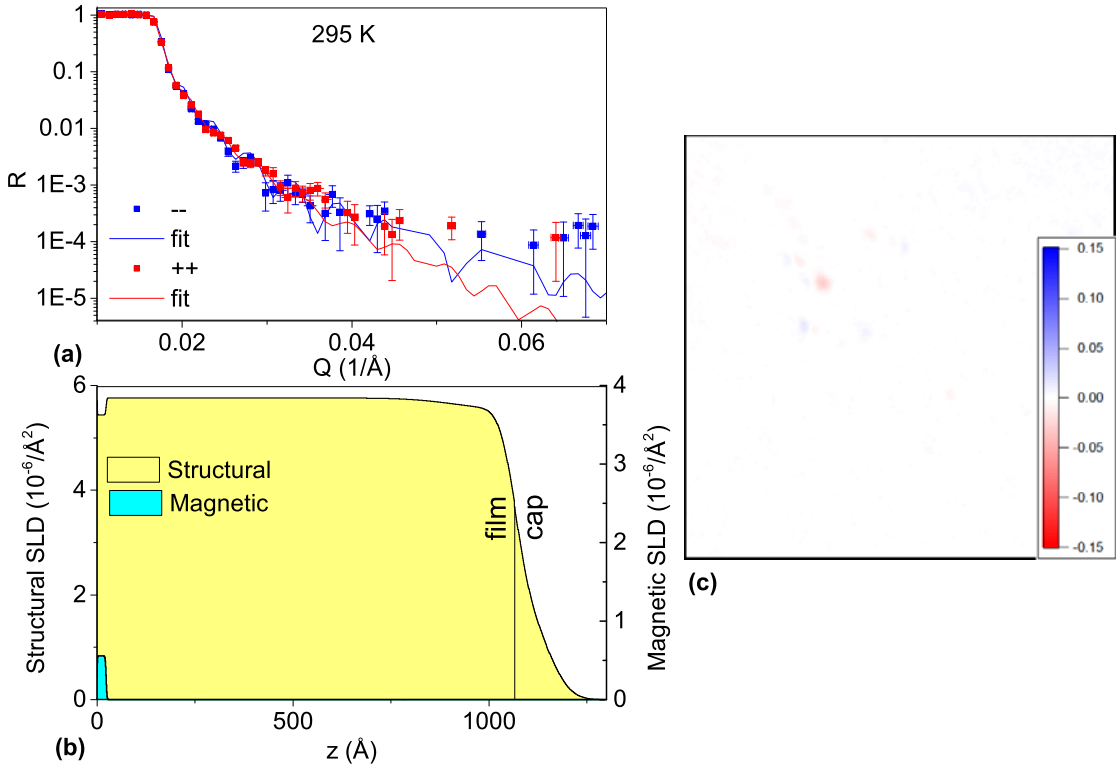

Figure 6.8: (a) Room temperature PNR reflectivity curves for FeRh capped with Ag and (b) corresponding structural and magnetic profile models. (c) XMCD-PEEM asymmetry image of FeRh capped with Ag near RT showing the mostly AF interface (except for a few weak residual local FM domains).

model and the detection of some oxidation in XPS of this film capped with Ag indicates the possibility of a non-uniform island forming cap, similar to the Pt cap. But since PNR information is averaged over the entire sample surface area and the field of view of the XMCD-PEEM image is 4 μm, assumed to be large compared to the size of islands, the FeRh/Ag interface was clearly probed in our measurements.

6.4 Discussion

To test the hypothesis that the interfacial FM is due to diffusion of the capping element which modifies T_0 of FeRh near the interface, the effect of three metallic caps was compared: Al, Pt (known to raise T_0) and Ag (non-miscible).

While no previous experimental observation exists on the effect of Al on FeRh, we suggest that it is comparable to the effect of Ni or Pd which are known to lower T_0. Diffusion of Al from the Al cap into the FeRh film during the growth results in a lightly Al doped FeRh layer near the interface with the cap, thereby lowering T_0 of this interfacial layer and making the FM phase stable at RT at the interface, as observed by XMCD-PEEM and PNR. Diffusion from the Pt cap results in a lightly Pt doped FeRh layer with the opposite effect of raising its T_0. The increase of T_0 induced by Pt doping is well-documented and ranges from 7 K to 20 K per at.% of Pt. [46, 87, 88, 89]. In this case the interfacial layer is not FM at RT because its T_{AF-FM} is raised even higher than that of the bulk of the film. For technological use of FeRh in which maintaining the magnetic properties of FeRh at the interface is desired, the selection of an immiscible element such as Ag or Re [88] as the cap material would prevent interfacial FM in FeRh. Ag is not miscible therefore has no effect on the magnetic properties of FeRh. Both oxide caps (fully-oxidized alumina and native oxide) do not induce any RT interfacial FM due to the absence of metallic element diffusion. A shown by the XPS analysis, the initial FM seen at the interface with the non-fully oxidized alumina cap is due to some residual metallic Al in the cap.

Another possible source of interfacial FM could be the stabilization of a layer with different FeRh composition from the bulk, either due to a single-species termination of the surface/interface or because of surface/interface segregation. The films studied in this work have [001] direction out of the plane, therefore we are interested in the properties of {001} surfaces. In a perfect equiatomic alloy, this surface consists of alternating Fe and Rh layers and is terminated by a layer of only one species.

Rh termination of the {001} surfaces in FeRh was experimentally observed by quantitative low energy electron diffraction (LEED) by Kim *et al.* [95]. Based on this observation, Lounis *et al.* [96] performed theoretical density functional theory calculations and showed that, for films below a certain thickness, 100 % Rh-terminated (001) surface results in a magnetic reconstruction which stabilizes the FM phase near the surface. Their calculation shows that 100 % Fe-terminated surface does not cause any magnetic surface reconstruction. However the stability of the Rh termination versus the Fe termination was not studied. Several groups have relied on this theory to explain the experimental observation of a residual FM component at RT [28, 44, 97], including the interfacial studies already mentioned [20, 21].

While there is some experimental evidence for preferential Rh termination of the FeRh (001) surface, no direct experimental reports of surface segregation leading to a local increase of Fe or Rh concentration could be found. Theoretical calculations of surface segregation energies in transition-metal alloys by Ruban*et al.* [98] predict a strong surface segregation of Rh in Fe for a bcc (001) surface but this calculation assumes that Rh is a dilute impurity and care must be taken when comparing this result to a concentrated equiatomic alloy of Fe and Rh as segregation reversal is seen in other concentrated systems. Indeed, Heinz *et al.* [99] report experimental results

on the ordered B2 FeAl alloy and show that the segregation question is quite rich and complicated. In summary, three general cases are possible: (1) the ordered bulk-like termination is favored, (2) chemical disorder is induced in the first few surface layers or (3) a new kind of chemical order can develop. This latter case is often the result of surface preparation (sputtering and annealing) inducing a metastable state. In particular the Rh termination observed by LEED in ref. [95] could be the result of the cleaning procedure that the sample experienced. In contrast, a recent surface-sensitive photoemission study of ultrathin FeRh films deposited in-situ by Lee *et al.* reported no significant change in Rh to Fe core level photoemission intensity ratio after annealing the film, indicating no strong tendency of surface segregation of either Fe or Rh [100].

Heat treatment of the film can also modify the surface. We have observed in XMCD-PEEM of uncapped films with an initial AF surface that after heating above the Curie temperature of 573 K, the surface of the film is modified (most likely by chemical diffusion) and remains FM to subsequent cooling. The same effect was observed on a film with higher Rh concentration heated only to 395 K for period of several hours.

Finally, the adsorption of atoms of a third species can modify the segregation or reconstruction expected in equilibrium with the vacuum. This means that capping with different materials could lead to different segregation configurations. A possible illustration was recently reported by McLaren *et al.* [101]. The composition profile along the cross-section of a 50 nm FeRh film capped with Al shows the presence of a Fe rich region extending to about 2 nm below the FeRh/Al interface. This result indicates that the Al cap favors Fe segregation at the interface, contrasting with the Rh termination of an Ar-ion-bombarded surface and the absence of segregation of the surface of an in-situ deposited film.

Since both Fe segregation and Rh termination could result in the stabilization of a FM layer at the interface one would expect a FM interface to always be observed. However our results show that this is not the case. In particular, the uncapped film was found to have a native oxide layer at the surface constituted of Fe oxide. The formation of Fe oxide causes Rh-enrichment of the top FeRh layer near the interface with the native oxide, but no interfacial FM was found, indicating that Rh-enrichment by itself is not enough to generate interfacial FM. Therefore we suggest that segregation effects are secondary and that the main driving force for the stabilization of FM is the alloying with the third metallic element from the cap.

Comparison of metallic Al and oxide alumina of similar thickness (5.6 and 7.5 nm determined from x-ray reflectivity) further eliminates strain as the cause since similar local strains are expected from these two caps, yet the interfacial FM is only observed with the Al cap. Additionally, a FeRh film capped with a thinner alumina layer (nominal 1.8 nm compared to 2.5 nm) shows the same behavior as seen in Fig. 6.4 (some initial interfacial FM that disappears after the first heating/cooling cycle). This confirms that strain resulting from capping layers of different thicknesses

is not alone enough to generate interfacial FM.

These results show that chemical effects alone can explain the stabilization of an interfacial FM layer at RT in FeRh capped with Al. The opposite effect of capping with a different metallic element (Pt) is clear evidence of the chemical origin of the FM layer and confirms our hypothesis.

6.5 Conclusion

In conclusion, the effect of capping material on interfacial FM layer between FeRh films and caps was systematically studied for 5 different capping materials (native oxide, alumina, Al, Pt, and Ag). While no measurable interfacial FM is seen at the interface with stable oxide caps, XMCD-PEEM and PNR confirm that Al stabilizes a FM layer of $\sim$7 nm with magnetization reduced by a factor of 7 with respect to the nominal FM film. No such layer is seen for Pt or Ag. The FM interface layer is the result of alloying between FeRh and the cap element. Al doping acts to lower T_0 while Pt raises it. Ag is not miscible therefore has no effect on the magnetic properties of FeRh. Understanding of the chemical inter-diffusion origin of interfacial FM in FeRh enables improvements in the technological implementation of FeRh. In particular the use of non-miscible layers is recommended to limit inter-diffusion between metallic layers and maintain the nominal magnetic properties of the FeRh film or, when not possible, the change in magnetic properties must be taken into account.

Chapter 7

Conclusion

The goal of this work was to perform a microscopic study of the unusual AF-FM transition in FeRh thin films, by doing temperature dependent in-situ microscopy of the evolution of the FM and AF phase across the transition.

Thin-film growth was implemented and optimized with extensive structural and magnetic characterization. Epitaxial, strain-free, near-equiatomic films were fabricated on MgO substrates and the hysteresis and broadening of the transition was determined at the macroscopic level. The effect of film composition was studied and an updated phase diagram was proposed with a maximum in T_0 at 48.5 at.% Rh and a progressive decrease in T_0 at higher Rh concentration.

We designed a membrane-based microfabricated device to be used as an x-ray transparent heater stage and tested this device in a transmission synchrotron x-ray microscope. Successful growth of single crystal FeRh onto this device was limited so we turned instead to a photoemission electron microscopy (PEEM) of FeRh on MgO substrates.

FM domains were imaged near the surface of FeRh thin films by XMCD-PEEM. Nucleation, growth and coalescence stages were identified in the phase transformation mechanism from AF to FM. The coexistence of FM and AF phases inherent to a first-order phase transition was observed in the early stages of the transition. The transition at the local nuclei level was found to be sharp, with the spread of these nucleation events contributing to the macroscopic broadening. Upon cooling, a different behavior was seen with the disappearance of the FM phase more progressive, corresponding to the growth of the AF phase.

XMLD-PEEM was used to spatially resolve the AF phase near the surface of FeRh thin films and its evolution upon cooling. The feature size and the magnetic contrast of the AF phase were close to the limit of the instrument, nevertheless a characteristic length of 300 nm was identified, smaller than the average size of FM domains and small changes in the AF morphology were detected between 5 K cooling steps, indicating that the growth of the AF phase is limited, most likely by crystalline defects. Moreover the AF structure was found to be reproducible to repeated cycling

through the transition, confirming its sensitivity to defects.

This study of the transition at the microscopic level has thus led to a better understanding of the domain structure of each phase and the broadening and asymmetry between heating and cooling of the macroscopically observed transition.

Finally, an alloying effect was found to be at the origin of the interfacial FM observed in capped FeRh thin films. Alloying with a metallic element can either lower or raise T_0. A lowered T_0 lead to a stable FM layer at the interface while a raised T_0 did not. The sensitivity of FeRh to chemical inter-diffusion was therefore demonstrated and non-miscible metallic layers or stable oxide layers are recommended in the integration of FeRh into technological devices.

FeRh is a unique system which offers many opportunities for exciting research. In the course of the research presented in this dissertation, other interesting questions have come up, some of which have sparked projects currently in progress in our lab. While we identified chemical diffusion as the primary cause of interfacial FM, strain is also known to affect the magnetic properties of these films, with tetragonal strain predicted to give rise to perpendicular anisotropy. More work is currently in progress to induce perpendicular anisotropy in the FM phase of FeRh by substrate induced strain. Successful growth of single crystalline FeRh films on the x-ray transparent heater stage we designed will allow transmission x-ray microscopy study which could reveal additional information about the nucleation and growth of domains not located at the surface of the film, but through the entire thickness of the film. The understanding we gained about what contributes to the broadening of the transition is relevant to the magnetocaloric effect in which the breadth of the transition affects the cooling power. The magnetocaloric effect will be investigated by thin-film calorimetry, using the membrane-based calorimeters. Finally, femtosecond dynamics studies (synchrotron x-ray transmission or reflectivity experiments) will shed light on the structural or magnetic origin of the transition and will benefit from the knowledge gained on the steady state of the transition, both from the initial film characterization and the PEEM microscopy.

Bibliography

[1] M. Fallot and R. Hocart. Sur l'apparition du ferromagnétisme par élévation de température dans des alliages de fer et de rhodium. *Rev. Sci.*, 77:498–500, 1939.

[2] F. De Bergevin and L. Muldawer. Etude cristallographique de certains alliages fer-rhodium. *Compt. Rend.*, 252:1347–1349, 1961.

[3] J. S. Kouvel and C. C. Hartelius. Anomalous magnetic moments and transformations in the ordered alloy FeRh. *Journal of Applied Physics*, 33(3):1343–1344, 1962.

[4] S. B. Roy, G. K. Perkins, M. K. Chattopadhyay, A. K. Nigam, K. J. S. Sokhey, P. Chaddah, A. D. Caplin, and L. F. Cohen. First order magnetic transition in doped $CeFe_2$ alloys: Phase coexistence and metastability. *Phys. Rev. Lett.*, 92:147203, Apr 2004.

[5] J. D. Moore, G. K. Perkins, Y. Bugoslavsky, L. F. Cohen, M. K. Chattopadhyay, S. B. Roy, P. Chaddah, K. A. Gschneidner, and V. K. Pecharsky. Correlating the local magnetic properties of the magnetic phase transition in Gd_5Ge_4 using scanning hall probe imaging. *Phys. Rev. B*, 73:144426, Apr 2006.

[6] L.J. Swartzendruber. The FeRh (iron-rhodium) system. *Bulletin of Alloy Phase Diagrams*, 5(5):456–462, 1984.

[7] S. Maat, J.-U. Thiele, and E. E. Fullerton. Temperature and field hysteresis of the antiferromagnetic-to-ferromagnetic phase transition in epitaxial FeRh films. *Phys. Rev. B*, 72:214432, Dec 2005.

[8] J. Cao, N. T. Nam, S. Inoue, H. Y. Y. Ko, N. N. Phuoc, and T. Suzuki. Magnetization behaviors for FeRh single crystal thin films. *Journal of Applied Physics*, 103(7):07F501, 2008.

[9] M. Sharma, H. M. Aarbogh, J.-U. Thiele, S. Maat, E. E. Fullerton, and C. Leighton. Magnetotransport properties of epitaxial MgO(001)/FeRh films across the antiferromagnet to ferromagnet transition. *Journal of Applied Physics*, 109(8):083913, 2011.

[10] L. M. Sandratskii and P. Mavropoulos. Magnetic excitations and femtomagnetism of FeRh: A first-principles study. *Phys. Rev. B*, 83:174408, May 2011.

[11] M. Manekar and S. B. Roy. Reproducible room temperature giant magnetocaloric effect in Fe-Rh. *Journal of Physics D: Applied Physics*, 41(19):192004, 2008.

[12] M. R. Ibarra and P. A. Algarabel. Giant volume magnetostriction in the FeRh alloy. *Phys. Rev. B*, 50:4196–4199, Aug 1994.

[13] N. T. Nam, W. Lu, and T. Suzuki. Exchange bias of ferromagnetic/antiferromagnetic in FePt/FeRh bilayers. *Journal of Applied Physics*, 105(7):07D708, 2009.

[14] J.-U. Thiele, S. Maat, and E. E. Fullerton. FeRh/FePt exchange spring films for thermally assisted magnetic recording media. *Applied Physics Letters*, 82(17):2859–2861, 2003.

[15] E.F. Kneller and R. Hawig. The exchange-spring magnet: a new material principle for permanent magnets. *Magnetics, IEEE Transactions on*, 27(4):3588–3560, 1991.

[16] M. Takahashi and R. Oshima. Annealing effect on phase transition of equiatomic FeRh alloy. *Materials Transactions, JIM*, 36(6):735–742, 1995.

[17] W. Lu, B. Yan, and T. Suzuki. Magnetic phase transition and magneto-optical properties in epitaxial $FeRh_{0.95}Pt_{0.05}$ single-crystal thin film. *Scripta Materialia*, 61(9):851 – 854, 2009.

[18] Y. Yokoyama, M. Usukura, S. Yuasa, Y. Suzuki, H. Miyajima, and T. Katayama. MFM observation of magnetic phase transitions in ordered FeRh systems. *Journal of Magnetism and Magnetic Materials*, 177181, Part 1(0):181 – 182, 1998. International Conference on Magnetism.

[19] M. Manekar, C. Mukherjee, and S. B. Roy. Imaging of time evolution of the first-order magneto-structural transition in $Fe - Rh$ alloy using magnetic force microscopy. *EPL*, 80(1):17004, 2007.

[20] Y. Ding, D. A. Arena, J. Dvorak, M. Ali, C. J. Kinane, C. H. Marrows, B. J. Hickey, and L. H. Lewis. Bulk and near-surface magnetic properties of FeRh thin films. *Journal of Applied Physics*, 103(7):07B515, 2008.

[21] R. Fan, C. J. Kinane, T. R. Charlton, R. Dorner, M. Ali, M. A. de Vries, R. M. D. Brydson, C. H. Marrows, B. J. Hickey, D. A. Arena, B. K. Tanner, G. Nisbet, and S. Langridge. Ferromagnetism at the interfaces of antiferromagnetic FeRh epilayers. *Phys. Rev. B*, 82:184418, Nov 2010.

[22] M. Loving, M. A. de Vries, F. Jimenez-Villacorta, C. Le Graet, X. Liu, R. Fan, S. Langridge, D. Heiman, C. H. Marrows, and L. H. Lewis. Tailoring the FeRh magnetostructural response with Au diffusion. *Journal of Applied Physics*, 112(4):043512, 2012.

[23] C. Baldasseroni, D. R. Queen, D. W. Cooke, K. Maize, A. Shakouri, and F. Hellman. Heat transfer simulation and thermal measurements of microfabricated x-ray transparent heater stages. *Review of Scientific Instruments*, 82(9):093904, 2011.

[24] C. Baldasseroni, C. Bordel, A. X. Gray, A. M. Kaiser, F. Kronast, J. Herrero-Albillos, C. M. Schneider, C. S. Fadley, and F. Hellman. Temperature-driven nucleation of ferromagnetic domains in FeRh thin films. *Applied Physics Letters*, 100(26):262401, 2012.

[25] K.M. Cher, T.J. Zhou, and J.S. Chen. Compositional effects on the structure and phase transition of epitaxial FeRh thin films. *Magnetics, IEEE Transactions on*, 47(10):4033–4036, 2011.

[26] D. Kande, S. Pisana, D. Weller, D.E. Laughlin, and Z. Jian-Gang. Enhanced B2 ordering of FeRh thin films using B2 NiAl underlayers. *Magnetics, IEEE Transactions on*, 47(10):3296–3299, 2011.

[27] S. Inoue, N. T. Nam, N. N. Phuoc, J. Cao, H. Y. Y. Ko, and T. Suzuki. Magnetic and magneto-optical properties of FeRh thin films. *Journal of Magnetism and Magnetic Materials*, 320(22):3113 – 3116, 2008. Eighth Perpendicular Magnetic Recording Conference.

[28] I. Suzuki, T. Koike, M. Itoh, T. Taniyama, and T. Sato. Stability of ferromagnetic state of epitaxially grown ordered FeRh thin films. *Journal of Applied Physics*, 105(7):07E501, 2009.

[29] W. Lu, Y. Wang, B. Yan, and T. Suzuki. Magnetic properties and first-order magnetic phase transition in single crystal FeRh thin film. *Journal of Materials Science*, 45(18):4919–4923, 2010.

[30] W. Lu, P. Huang, K. Li, and B. Yan. Effect of substrate temperature on the crystallographic structure and first-order magnetic phase transition of FeRh thin films. *Journal of Materials Research*, 28:1042–1046, 3 2013.

[31] B.D. Cullity and S.R. Stock. *Elements of x-ray diffraction*. Pearson education. Prentice Hall, 3rd edition, 2001.

[32] Professor Andrew Zangwill. Epitaxial phenomena. Lecture notes, Summer 1991. Troisième cycle de la physique en Suisse Normande.

[33] M A de Vries, M Loving, A P Mihai, L H Lewis, D Heiman, and C H Marrows. Hall-effect characterization of the metamagnetic transition in FeRh. *New Journal of Physics*, 15(1):013008, 2013.

[34] E. Yang, D.E. Laughlin, and Jian-Gang Z. Correction of order parameter calculations for FePt perpendicular thin films. *Magnetics, IEEE Transactions on*, 48(1):7–12, 2012.

[35] D. W. Cooke, F. Hellman, C. Baldasseroni, C. Bordel, S. Moyerman, and E. E. Fullerton. Thermodynamic measurements of Fe-Rh alloys. *Phys. Rev. Lett.*, 109:255901, Dec 2012.

[36] D. L. Smith. *Thin-film deposition: principles and practice*. McGraw-Hill, 1995.

[37] C. Bordel, J. Juraszek, D. W. Cooke, C. Baldasseroni, S. Mankovsky, J. Minár, H. Ebert, S. Moyerman, E. E. Fullerton, and F. Hellman. Fe spin reorientation across the metamagnetic transition in strained FeRh thin films. *Phys. Rev. Lett.*, 109:117201, Sep 2012.

[38] N. Anderson. Towards perpendicular anisotropy in ferromagnetic FeRh thin films. Summer research report, University of California Berkeley, July 2012.

[39] X.H. Wei, J. Zhu, and Y.R. Li. Anisotropic lattice strain relaxation of $MgO/SrTiO_3(001)$ in a textured island growth mode. *Vacuum*, 85(11):999 – 1003, 2011.

[40] F. Niu, A. L. Meier, and B. W. Wessels. Epitaxial growth and strain relaxation of MgO thin films on Si grown by molecular beam epitaxy. *Journal of Vacuum Science & Technology B: Microelectronics and Nanometer Structures*, 24(6):2586–2591, 2006.

[41] J. Perrière. Rutherford backscattering spectrometry. *Vacuum*, 37(56):429 – 432, 1987.

[42] G. Shirane, C. W. Chen, P. A. Flinn, and R. Nathans. Mössbauer study of hyperfine fields and isomer shifts in the Fe-Rh alloys. *Phys. Rev.*, 131:183–190, Jul 1963.

[43] G. Shirane, R. Nathans, and C. W. Chen. Magnetic moments and unpaired spin densities in the Fe-Rh alloys. *Phys. Rev.*, 134:A1547–A1553, Jun 1964.

[44] G. C. Han, J. J. Qiu, Q. J. Yap, P. Luo, T. Kanbe, T. Shige, D. E. Laughlin, and J.-G. Zhu. Suppression of low-temperature ferromagnetic phase in ultrathin FeRh films. *Journal of Applied Physics*, 113(12):123909, 2013.

[45] A. I. Zakharov, A. M. Kadomtseva, R. Z. Levitin, and E. G. Ponyatovskii. Magnetic and magnetoelastic properties of a metamagnetic iron-rhodium. *Soviet Physics - Journal of Experimental and Theoretical Physics*, 19:1348–1353, December 1964.

[46] J. S. Kouvel. Unusual nature of the abrupt magnetic transition in FeRh and its pseudobinary variants. *Journal of Applied Physics*, 37(3):1257–1258, 1966.

[47] L.J. Swartzendruber. Fe-Rh phase diagram. ASM Alloy Phase Diagrams Center - Online, 1990. P. Villars, editor-in-chief; H. Okamoto and K. Cenzual, section editors;.

[48] R. C. Wayne. Pressure dependence of the magnetic transitions in Fe-Rh alloys. *Phys. Rev.*, 170:523–527, Jun 1968.

[49] M. Zhang, E. A. Olson, R. D. Twesten, J. G. Wen, L. H. Allen, I. M. Robertson, and I. Petrov. In situ transmission electron microscopy studies enabled by microelectromechanical system technology. *J. Mater. Res.*, 20(7):1802–1807, 2005.

[50] E. De Smit, I. Swart, J. F. Creemer, G. H. Hoveling, M. K. Gilles, T. Tyliszczak, P. J. Kooyman, H. W. Zandbergen, C. Morin, B. M. Weckhuysen, and F. M. F. De Groot. Nanoscale chemical imaging of a working catalyst by scanning transmission x-ray microscopy. *Nature*, 456(7219):222–225, 2008.

[51] D. W. Denlinger, E. N. Abarra, K. Allen, P. W. Rooney, S. K. Watson, and F. Hellman. Thin film microcalorimeter for heat capacity measurements from 1. 5 to 800 k. *Rev. Sci. Instrum.*, 65(4):946, 1994.

[52] D. R. Queen and F. Hellman. Thin film nanocalorimeter for heat capacity measurements of 30 nm films. *Rev. Sci. Instrum.*, 80(6):063901, 2009.

[53] B. Revaz, B. L. Zink, and F. Hellman. $Si - N$ membrane-based microcalorimetry: Heat capacity and thermal conductivity of thin films. *Thermochim. Acta*, 432(2):158–168, 2005.

[54] B. Revaz, B. L. Zink, D. O'Neil, L. Hull, and F. Hellman. Numerical simulation of the heat transfer in amorphous silicon nitride membrane-based microcalorimeters. *Rev. Sci. Instrum.*, 74(10):4389–4403, 2003.

[55] D. W. Cooke, K. J. Michel, and F. Hellman. Thermodynamic measurements of submilligram bulk samples using a membrane-based "calorimeter on a chip". *Rev. Sci. Instrum.*, 79(5):053902–10, 2008.

[56] J. Christofferson, K. Maize, Y. Ezzahri, J. Shabani, X. Wang, and A. Shakouri. Microscale and nanoscale thermal characterization techniques. *Journal of Electronic Packaging*, 130(4):041101, 2008.

[57] G. C. Albright, J. A. Stump, J. D. McDonald, and H. Kaplan. True temperature measurements on microscopic semiconductor targets. *Proceedings of SPIE*, 3700:245–250, 1999.

[58] J. Christofferson and A. Shakouri. Thermoreflectance based thermal microscope. *Rev. Sci. Instrum.*, 76(2):024903, 2005.

[59] M. Farzaneh, K. Maize, D. Lüeren, J. A. Summers, P. M. Mayer, P. E. Raad, K. P. Pipe, A. Shakouri, R. J. Ram, and J. A. Hudgings. Ccd-based thermoreflectance microscopy: principles and applications. *Journal of Physics D: Applied Physics*, 42(14):143001, 2009.

[60] G. Tessier, S. Holé, and D. Fournier. Quantitative thermal imaging by synchronous thermoreflectance with optimized illumination wavelengths. *Appl. Phys. Lett.*, 78(16):2267–2269, 2001.

[61] F. P. Incropera and D. P. Dewitt. *Introduction to heat transfer*. John Wiley and Sons, 4 edition, 2001.

[62] B. L. Zink, B. Revaz, J. J. Cherry, and F. Hellman. Measurement of thermal conductivity of thin films with a $Si-N$ membrane-based microcalorimeter. *Rev. Sci. Instrum.*, 76(2):024901, 2005.

[63] C. Y. Ho, R. W. Powell, and P.E. Liley. Thermal conductivity of the elements. *J. Phys. Chem. Ref. Data*, 1(2):279–422, 1972.

[64] L. N. Aksyutov. Normal spectral emissivity of gold, platinum, and tungsten. *Journal of Engineering Physics and Thermophysics*, 27(2), 1974.

[65] B. H. Frazer, B. Gilbert, B. R. Sonderegger, and G. De Stasio. The probing depth of total electron yield in the sub-kev range: $TEY-XAS$ and $X-PEEM$. *Surface Science*, 537(13):161 – 167, 2003.

[66] G. Schütz, W. Wagner, W. Wilhelm, P. Kienle, R. Zeller, R. Frahm, and G. Materlik. Absorption of circularly polarized x rays in iron. *Phys. Rev. Lett.*, 58:737–740, Feb 1987.

[67] C. M. Schneider and G. Schönhense. Investigating surface magnetism by means of photoexcitation electron emission microscopy. *Reports on Progress in Physics*, 65(12):1785, 2002.

[68] J. Nogués and I. K. Schuller. Exchange bias. *Journal of Magnetism and Magnetic Materials*, 192(2):203 – 232, 1999.

[69] F. Bertaut, F. de Bergevin, and G. Roult. Etude par diffraction neutronique de $Fe_{0,47}Rh_{0,53}$. *Compt. Rend.*, 256:1688–1691, 1963.

[70] E. O. Wollan and W. C. Koehler. Neutron diffraction study of the magnetic properties of the series of perovskite-type compounds $[(1-x)\mathrm{La},\ x\mathrm{Ca}]\mathrm{Mno}_3$. *Phys. Rev.*, 100:545–563, Oct 1955.

[71] W. L. Roth. Neutron and optical studies of domains in NiO. *Journal of Applied Physics*, 31(11):2000–2011, 1960.

[72] A. Scholl, J. Stöhr, J. Lüning, J. W. Seo, J. Fompeyrine, H. Siegwart, J.-P. Locquet, F. Nolting, S. Anders, E. E. Fullerton, M. R. Scheinfein, and H. A. Padmore. Observation of antiferromagnetic domains in epitaxial thin films. *Science*, 287(5455):1014–1016, 2000.

[73] F. Nolting, A. Scholl, J. Stöhr, J. W. Seo, J. Fompeyrine, H. Siegwart, J.-P. Locquet, S. Anders, J. Lüning, E. E. Fullerton, M. F. Toney, M. R. Scheinfein, and H. A. Padmore. Direct observation of the alignment of ferromagnetic spins by antiferromagnetic spins. *Nature*, 405:767–769, 2000.

[74] P. Kuiper, B. G. Searle, P. Rudolf, L. H. Tjeng, and C. T. Chen. X-ray magnetic dichroism of antiferromagnet fe_2o_3: The orientation of magnetic moments observed by Fe $2p$ x-ray absorption spectroscopy. *Phys. Rev. Lett.*, 70:1549–1552, Mar 1993.

[75] J. Stöhr and H. C. Siegmann. *Magnetism, From Fundamentals to Nanoscale Dynamics*. Springer Series in Solid-State Sciences, 2006.

[76] M. M. Schwickert, G. Y. Guo, M. A. Tomaz, W. L. O'Brien, and G. R. Harp. X-ray magnetic linear dichroism in absorption at the l edge of metallic Co, Fe, Cr, and V. *Phys. Rev. B*, 58:R4289–R4292, Aug 1998.

[77] S. S. Dhesi, G. van der Laan, and E. Dudzik. Determining element-specific magnetocrystalline anisotropies using x-ray magnetic linear dichroism. *Applied Physics Letters*, 80(9):1613–1615, 2002.

[78] J. Kuneš, P.M. Oppeneer, S. Valencia, D. Abramsohn, H.-Ch. Mertins, W. Gudat, M. Hecker, and C.M. Schneider. Understanding the XMLD and its magnetocrystalline anisotropy at the $l_{2,3}$-edges of 3d transition metals. *Journal of Magnetism and Magnetic Materials*, 272276, Part 3(0):2146 – 2147, 2004. Proceedings of the International Conference on Magnetism (ICM 2003).

[79] M. Finazzi, A. Brambilla, P. Biagioni, J. Graf, G.-H. Gweon, A. Scholl, A Lanzara, and L. Duò. Interface coupling transition in a thin epitaxial antiferromagnetic film interacting with a ferromagnetic substrate. *Phys. Rev. Lett.*, 97:097202, Aug 2006.

[80] W. Kuch, F. Offi, L. I. Chelaru, J. Wang, K. Fukumoto, M. Kotsugi, J. Kirschner, and J. Kuneš. Huge magnetocrystalline anisotropy of x-ray linear dichroism observed on CoFeMn bilayers. *Phys. Rev. B*, 75:224406, Jun 2007.

[81] J. B. Kortright and S.-K. Kim. Resonant magneto-optical properties of Fe near its $2p$ levels: measurement and applications. *Phys. Rev. B*, 62:12216–12228, Nov 2000.

[82] H. A. McKay, H. Chen, R. M. Feenstra, and P. J. Poole. Scanning tunneling microscopy images of $\mathrm{III}-\mathrm{V}$ semiconductor alloys: Strain effects. *Journal of Vacuum Science & Technology B: Microelectronics and Nanometer Structures*, 21(1):18–22, 2003.

[83] D. M. Rubin. A simple autocorrelation algorithm for determining grain size from digital images of sediment. *Journal of Sedimentary Research*, 74(1):160–165, 2004.

[84] C. Robertson and S. C. George. Theory and practical recommendations for autocorrelation-based image correlation spectroscopy. *Journal of Biomedical Optics*, 17(8):080801–1–080801–7, 2012.

[85] F. Hellman, A. L. Shapiro, E. N. Abarra, R. A. Robinson, R. P. Hjelm, P. A. Seeger, J. J. Rhyne, and J. I. Suzuki. Long ferromagnetic correlation length in amorphous $TbFe_2$. *Phys. Rev. B*, 59:11408–11415, May 1999.

[86] S. Hashi, S. Yanase, Y. Okazaki, and M. Inoue. A large thermal elasticity of the ordered FeRh alloy film with sharp magnetic transition. *Magnetics, IEEE Transactions on*, 40(4):2784–2786, 2004.

[87] S. Yuasa, Y. Otani, H. Miyajima, and A. Sakuma. Magnetic properties of bcc $FeRh_{1-x}M_x$ systems. *Magnetics in Japan, IEEE Translation Journal on*, 9(6):202–209, 1994.

[88] P. H. L. Walter. Exchange inversion in ternary modifications of iron rhodium. *Journal of Applied Physics*, 35(3):938–939, 1964.

[89] W. Lu, N. T. Nam, and T. Suzuki. Effect of Pt doping on the structure, magnetic, and magneto-optical properties of ordered FeRh-Pt thin films. *Magnetics, IEEE Transactions on*, 45(6):2716–2719, 2009.

[90] W. Lu, N. T. Nam, and T. Suzuki. First-order magnetic phase transition in FeRh-Pt thin films. *Journal of Applied Physics*, 105(7):07A904, 2009.

[91] C.F. Majkrzak. Neutron scattering studies of magnetic thin films and multilayers. *Physica B: Condensed Matter*, 221(14):342 – 356, 1996. Proceedings of the Fourth International Conference on Surface X-ray and Neutron Scattering.

[92] P. A. Kienzle, J. Krycka, N. Patel, and I. Sahin. Refl1d (version 0.6.19). [Computer Software], 2011. College Park, MD.

[93] S. R. Spurgeon, J. D. Sloppy, R. Tao, R. F. Klie, S. E. Lofland, J. K. Baldwin, A. Misra, and M. L. Taheri. A study of the effect of iron island morphology and interface oxidation on the magnetic hysteresis of Fe-MgO (001) thin film composites. *Journal of Applied Physics*, 112(1):013905, 2012.

[94] C. Martinez-Boubeta, L. Balcells, and B. Martinez. On the changes at the Fe/MgO interface upon annealing. *Journal of Applied Physics*, 113(12):123908, 2013.

[95] S. Kim, F. Jona, and P. M. Marcus. Atomic structure of a 001 surface of the alloy FeRh. *Surface Review and Letters*, 06(01):133–136, 1999.

[96] S. Lounis, M. Benakki, and C. Demangeat. Ferromagnetic stabilization of ordered B2 FeRh thin films. *Phys. Rev. B*, 67:094432, Mar 2003.

[97] G. C. Han, J. J. Qiu, Q. J. Yap, P. Luo, D. E. Laughlin, J. G. Zhu, T. Kanbe, and T. Shige. Magnetic stability of ultrathin FeRh films. *Journal of Applied Physics*, 113(17):17C107, 2013.

[98] A. V. Ruban, H. L. Skriver, and J. K. Nørskov. Surface segregation energies in transition-metal alloys. *Phys. Rev. B*, 59:15990–16000, Jun 1999.

[99] K. Heinz and L. Hammer. Surface structure and segregation of bimetallic bcc-type alloys. *Journal of Physics: Condensed Matter*, 11(43):8377, 1999.

[100] J.-S. Lee, E. Vescovo, L. Plucinski, C. M. Schneider, and C.-C. Kao. Electronic structure and magnetic properties of epitaxial FeRh(001) ultrathin films on W(100). *Phys. Rev. B*, 82:224410, Dec 2010.

[101] M. J. McLaren, M. A. de Vries, R. M. D. Brydson, and C. Marrows. Characterisation of magnetic FeRh epilayers. *Journal of Physics: Conference Series*, 371(1):012031, 2012.

[102] W. M. Rohsenow, J. P. Hartnett, and Y. I. Cho. *Handbook of Heat Transfer (3rd Edition)*. McGraw-Hill, 1998.

Appendix A

Heat transfer dimensionless numbers analysis

The following are the heat transfer dimensionless numbers used in convection problems. [61, 102]

The Grashof number is the ratio of buoyancy to viscous forces. Its expression is given by

$$Gr = \frac{g\beta\Delta T L^3}{\nu^2} \tag{A.1}$$

with g the acceleration due to Earth's gravity, β the coefficient of thermal expansion, ΔT the temperature difference between the system and the gas, L the characteristic length of the system and ν the kinematic viscosity of the gas which is equal to the ratio of the dynamic viscosity η and the density ρ.

The Prandtl number is the ratio of molecular momentum and thermal diffusivity. Its expression is given by

$$Pr = \frac{\nu}{\alpha} \tag{A.2}$$

where the diffusivity α is defined as

$$\alpha = \frac{\lambda}{\rho C_p} \tag{A.3}$$

with λ the thermal conductivity and C_p the specific heat capacity.

The Rayleigh number is the product of the Grashof number and the Prandtl number:

$$Ra = GrPr \tag{A.4}$$

The transition from laminar to turbulent regime occurs at $Ra > 10^9$. At 760 Torr of nitrogen, based on the microscale dimension of our system $Ra = 0.85 << 10^9$ so we are far from the turbulent transition.

The Knudsen number is the ratio of gas molecule mean free path to the system's characteristic length:

$$Kn = \frac{\ell}{L} \tag{A.5}$$

with the mean free path given by

$$\ell = \frac{RT}{\sqrt{2}\pi d^2 \mathcal{N}_A p} \tag{A.6}$$

where d is the diameter of the gas molecules, p the pressure of the gas, R the universal gas constant and $\mathcal{N}_A$ is the Avogadro number.

In the molecular regime, the molecular impingement flux is defined by

$$J = \frac{N_A P}{\sqrt{2\pi MRT}} \tag{A.7}$$

with M the molecular weight of the gas.